PLASMA DYNAMICS

X. PLASMA DYNAMICS

Academic and Research Staff

Prof. George Bekefi
Prof. Abraham Bers
Prof. Flora Y. F. Chu
Prof. Bruno Coppi
Prof. Thomas H. Dupree
Prof. Elias P. Gyftopoulos
Prof. Lawrence M. Lidsky
Prof. James E. McCune
Prof. Peter A. Politzer
Prof. Louis S. Scaturro
Prof. Dieter J. Sigmar
Prof. Louis D. Smullin
Dr. Bamandas Basu
Dr. Giuseppe Bertin
Dr. Frank W. Chambers
Dr. Luciano DeMenna
Dr. Ronald C. Englade
Dr. Stephen P. Hirshman
Dr. George L. Johnston
Dr. Kim Molvig
Dr. Thaddeus Orzechowski
Dr. Aniket Pant
Dr. Francesco Pegoraro
Dr. Theo Schep
Dr. Adolfo Taroni
Kevin Hunter
John J. McCarthy
William J. Mulligan
James L. Terry

Graduate Students

Charles T. Breuer
Warren K. Brewer
Leslie Bromberg
Constantine J. Callias
Natale M. Ceglio
Hark C. Chan
Franklin R. Chang
John A. Combs
Donald L. Cook
David A. Ehst
Antonio Ferreira
Nathaniel J. Fisch
Alan S. Fisher
Jay L. Fisher
Alan R. Forbes
Ricardo M. O. Galvao
Keith C. Garel
Mark Gottlieb
James S. Herring
Ady Hershcovitch
James C. Hsia
Alan C. Janos
Mark D. Johnston
David L. Kaplan
Masayuki Karakawa
Charles F. F. Karney
Peter T. Kenyon
Robert E. Klinkowstein
David S. Komm
Craig M. Kullberg
John L. Kulp, Jr.
David B. Laning
George P. Lasche
Kenneth J. Laskey
Edward M. Maby
Francois Martin
Mark L. McKinstry
Thomas J. McManamy
David O. Overskei
Alan Palevsky
Louis R. Pasquarelli
Robert E. Potok
Robert H. Price
Allan H. Reiman
John E. Rice
Burton Richards
Kenneth Rubenstein
Richard E. Sclove
Earl L. Simmons
Michael D. Stiefel
David S. Stone
Kenneth P. Swartz
Miloslav S. Tekula
David J. Tetrault
Kim S. Theilhaber
Clarence E. Thomas
Alan L. Throop
Ben M. Tucker
Ernesto C. Vanterpol
David M. Wildman
Stephen M. Wolfe
Michael A. Zuniga

X. PLASMA DYNAMICS

A. Basic Plasma Research

1. CHARGE-EXCHANGE ENHANCEMENT

National Science Foundation (Grant ENG75-06242-A01)

Edward W. Maby, Louis D. Smullin

Introduction

In order to produce negative hydrogen or deuterium ion beams, the output of a positive ion source must undergo charge exchange with neutral atoms such as cesium. The maximum efficiency of this process is 21% for 800-eV H^+ interacting with cesium.[1] It has been suggested that by optically exciting the cesium, the efficiency can be improved.[2] The purpose of this report is to explore the feasibility of this suggestion. We shall review the mathematics that describes the H-Cs charge-exchange process, and then estimate the degree of efficiency enhancement at 2 keV in order to imply a new maximum efficiency at a lower energy. We shall also examine the technological issues that arise as a consequence of the enhancement effort and discuss the direction of future work.

Charge-Exchange Mathematics

Let F^+, F^O, and F^- represent the fractional portion of a hydrogen beam that is positive, neutral, and negative ($F^+ + F^O + F^- = 1$). Let each possible charge-exchange reaction be described by a cross section σ_{ij}, where $i, j \in \{+, 0, -\}$. Furthermore, let this variable π represent an effective target "thickness" equal to the actual thickness in cm multiplied by the target density in cm^{-3}. The charge-exchange process may be modeled by the following differential equations:

$$\frac{dF^+}{d\pi} = -(\sigma_{+o}+\sigma_{+-})F^+ + \sigma_{o+}F^O + \sigma_{-+}F^- \tag{1a}$$

$$\frac{dF^O}{d\pi} = \sigma_{+o}F^+ - (\sigma_{o-}+\sigma_{o+})F^O + \sigma_{-o}F^- \tag{1b}$$

$$\frac{dF^-}{d\pi} = \sigma_{+-}F^+ + \sigma_{o-}F^O - (\sigma_{-+}+\sigma_{-o})F^-. \tag{1c}$$

Given a set of initial values, i.e., $F^O_o = F^-_o = 0$, the Laplace transform of each component can easily be determined.

$$L^+(s) = D^{-1}(s^2+s(\sigma_{-+}+\sigma_{-o}+\sigma_{o-}+\sigma_{o+}) + \sigma_{o-}\sigma_{-+} + \sigma_{o+}\sigma_{-o} + \sigma_{o+}\sigma_{-+}) \tag{2a}$$

$$L^{O}(s) = D^{-1}(s\sigma_{+O}+\sigma_{+-}\sigma_{-O}+\sigma_{-+}\sigma_{+O}+\sigma_{+O}\sigma_{-O}) \tag{2b}$$

$$L^{-}(s) = D^{-1}(s\sigma_{+-}+\sigma_{+O}\sigma_{O-}+\sigma_{O+}\sigma_{+-}+\sigma_{+-}\sigma_{O-}), \tag{2c}$$

where

$$D = s^3 + s^2(\sigma_{+-}+\sigma_{+O}+\sigma_{O+}+\sigma_{O-}+\sigma_{-+}+\sigma_{-O})$$

$$+ s(\sigma_{O-}\sigma_{+O}+\sigma_{O+}\sigma_{+-}+\sigma_{O-}\sigma_{-+}+\sigma_{-O}\sigma_{+-}+\sigma_{O+}\sigma_{-O}+\sigma_{-+}\sigma_{+O}+\sigma_{-O}\sigma_{+O}+\sigma_{O+}\sigma_{-+}+\sigma_{O-}\sigma_{-+}). \tag{3}$$

The inverse transform of each component takes the form

$$F = A + B(1 - \exp(-s_1\pi)) + C(1 - \exp(-s_2\pi)). \tag{4}$$

Here s_1 and s_2, in addition to $s = 0$, are the roots of D. They determine the target "thickness" at which each component is in equilibrium. We consider principally those cases for which this condition is true, since F^- approaches a limiting maximum value as $\pi \to \infty$. Each equilibrium value may be determined by evaluating the limit of sL(s) as $s \to 0$.

$$F^{-}\big|_{\infty} = \frac{\sigma_{+O}\sigma_{O-}+\sigma_{O+}\sigma_{+-}+\sigma_{+-}\sigma_{O-}}{\sigma_{O-}\sigma_{+O}+\sigma_{O+}\sigma_{+-}+\sigma_{O-}\sigma_{-+}+\sigma_{O+}\sigma_{-O}+\sigma_{-O}\sigma_{+-}+\sigma_{-O}\sigma_{+O}+\sigma_{O+}\sigma_{-+}+\sigma_{O-}\sigma_{+-}+\sigma_{-+}\sigma_{+O}} \tag{5a}$$

$$F^{O}\big|_{\infty} = \frac{\sigma_{+-}\sigma_{-O}+\sigma_{-+}\sigma_{+O}+\sigma_{+O}\sigma_{-O}}{\sigma_{O-}\sigma_{+O}+\sigma_{O+}\sigma_{+-}+\sigma_{O-}\sigma_{-+}+\sigma_{O+}\sigma_{-O}+\sigma_{-O}\sigma_{+-}+\sigma_{-O}\sigma_{+O}+\sigma_{O+}\sigma_{-+}+\sigma_{O-}\sigma_{+-}+\sigma_{-+}\sigma_{+O}} \tag{5b}$$

$$F^{+}\big|_{\infty} = \frac{\sigma_{O-}\sigma_{-+}+\sigma_{O+}\sigma_{-O}+\sigma_{O+}\sigma_{-+}}{\sigma_{O-}\sigma_{+O}+\sigma_{O+}\sigma_{+-}+\sigma_{O-}\sigma_{-+}+\sigma_{O+}\sigma_{-O}+\sigma_{-O}\sigma_{+-}+\sigma_{-O}\sigma_{+O}+\sigma_{O+}\sigma_{-+}+\sigma_{O-}\sigma_{+-}+\sigma_{-+}\sigma_{+O}}. \tag{5c}$$

As a numerical example, we calculate each equilibrium value using the known cross sections for 2-keV hydrogen interacting with cesium.[3,4]

σ	2 keV H → Cs	σ	2 keV H → Cs
σ_{+O}	6.8×10^{-15} cm^2	σ_{O-}	1.5×10^{-16} cm^2
σ_{+-}	3.7×10^{-17} cm^2	σ_{-+}	6.3×10^{-18} cm^2
σ_{O+}	1.2×10^{-17} cm^2	σ_{-O}	2.0×10^{-15} cm^2

Therefore

$$F^-|_\infty = .0695$$

$$F^O|_\infty = .9288$$

$$F^+|_\infty = .0017.$$

These values agree well with experiment.

Enhancement Estimation

We make the following observations concerning the expression for $F^-|_\infty$:

(i) σ_{-+} is sufficiently small to be neglected. The reaction to which it corresponds, $H^- + Cs^+ \rightarrow H^+ + Cs^O + e$, is not influenced when the cesium is excited.

(ii) σ_{+-} may be neglected, since $dF^-|_\infty/d\sigma_{+-}$ is very small.

(iii) $dF^-|_\infty/d\sigma_{+O} \ll dF^-|_\infty/d\sigma_{O-}$.

(iv) The reaction corresponding to σ_{O+}, $H^O + Cs^+ \rightarrow H^+ + Cs^O$, is not influenced when the cesium is excited.

Observations (i) and (ii) permit simplification of Eq. 5a:

$$F^-|_\infty \approx \frac{\frac{\sigma_{O-}}{\sigma_{-O}}}{\frac{\sigma_{O-}}{\sigma_{-O}} + \frac{\sigma_{O+}}{\sigma_{+O}} + 1}. \tag{6}$$

Observations (iii) and (iv) imply that enhancement of $F^-|_\infty$ is primarily due to enhancement of σ_{O-} and that other σ changes are unimportant. In fact, since $\sigma_{O+}/\sigma_{+O} \ll 1$ and $\sigma_{O-}/\sigma_{-O} \ll 1$, $F^-|_\infty$ is nearly proportional to σ_{O-}.

It has been observed by Oparin et al.[5] that the maximum values of σ_{+O} for hydrogen interacting with different elements ($H^+ + E^O \rightarrow H^O + E^+$) are proportional to $V_i^{-5/2}$, where V_i is the ionization potential of the element. Assuming that this proportionality also holds for σ_{O-} ($H^O + Cs^O \rightarrow H^- + Cs^+$), then

$$\frac{\sigma^*_{O-}}{\sigma_{O-}} \sim \left(\frac{V_i^*}{V_i}\right)^{-5/2}. \tag{7}$$

For cesium, $V_i = 3.89$ eV and $V_i^* = 2.44$ eV (first excited state). Therefore

$$\frac{\sigma^*_{O-}}{\sigma_{O-}} \sim 3.2. \tag{8}$$

Unfortunately, only half of the cesium atoms can be excited optically at one time. Hence

$$\frac{F^-|^*_\infty}{F^-|_\infty} \sim \frac{1}{2}\left(\frac{\sigma^*_{O-}}{\sigma_{O-}}\right) = 1.6, \tag{9}$$

or $F^-|^*_\infty = .111$ at 2 keV. Assuming roughly the same degree of enhancement at all energies, we conclude that the maximum efficiency previously stated as 21% can be enhanced to approximately 33%.

Technological Problems

The cesium target "thickness", π, required for equilibrium charge exchange is approximately 2×10^{16} cm^{-2} for the example that has been presented. This value can be made a characteristic of an atomic cesium beam through which the H^+ source output must pass at right-angle incidence. The optical excitation is produced by a dye laser, tuned to the first cesium spectral line. Its beam is perpendicular to both the hydrogen and cesium beams at their point of intersection. The linewidth of the excited transition is not Doppler-broadened as a consequence of this geometry, so that the excitation efficiency is not reduced. Unfortunately, the cesium is so strongly absorbent that much laser power will be lost through scattering. For practical applications, this factor must not ultimately outweigh the gain in H^- output power.

A compact radio-frequency H^+ source has been designed and built, as shown in Fig. X-1. It can produce up to 10 μA output current. The first experiments will

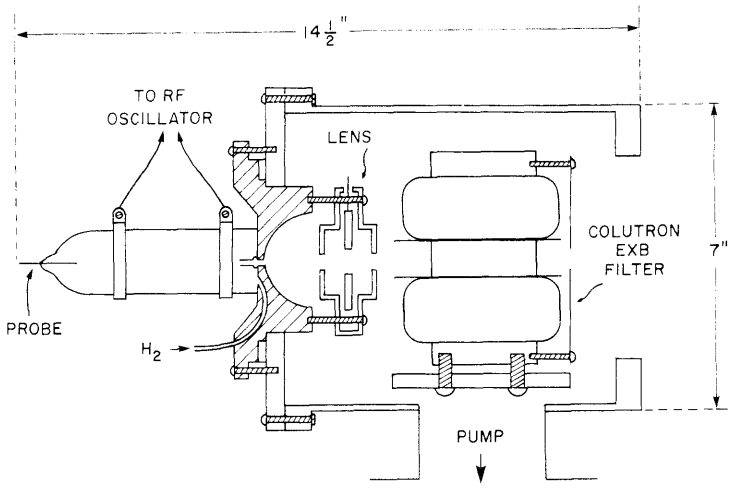

Fig. X-1. Radio-frequency H^+ source.

involve sodium rather than cesium because a dye laser tuned to the first sodium transition is available and will be performed in collaboration with Professors D. Kleppner and W. Phillips in the Atomic Resonance and Scattering laboratory, where an Na vapor system and a dye laser of suitable characteristics to excite the Na are available.

References

1. H. Tawara and A. Russek, Rev. Mod. Phys. 45, 178 (1973).
2. Daniel Kleppner, Private communication, 1976.
3. A. S. Schlachter, P. J. Bjorkholm, D. H. Loyd, L. W. Anderson, and W. Haeberli, Phys. Rev. 177, 184 (1969).
4. T. E. Leslie, K. P. Sarver, and L. W. Anderson, Phys. Rev. A 4, 408 (1971).
5. V. A. Oparin, R. N. Il'in, and E. S. Solov'ev, Sov. Phys. – JETP 24, 240 (1967).

2. SPACE-TIME SOLUTION OF THREE-WAVE RESONANT EQUATIONS WITH ONE WAVE HEAVILY DAMPED

National Science Foundation (Grant ENG75-06242-A01)

Flora Y. F. Chu, Charles F. F. Karney

The resonant interaction between three waves of action amplitudes a_j, $j = 1, 2, 3$, whose frequencies and wave vectors obey the resonant conditions $\omega_1 = \omega_2 + \omega_3$, $k_1 = k_2 + k_3$, can be described by

$$v_1 a_{1x} + a_{1t} + \gamma_1 a_1 = -K a_2 a_3 \tag{1a}$$

$$v_2 a_{2x} + a_{2t} + \gamma_2 a_2 = K^* a_1 a_3^* \tag{1b}$$

$$v_3 a_{3x} + a_{3t} + \gamma_3 a_3 = K^* a_1 a_2^*. \tag{1c}$$

In (1), v's are the group velocities of the waves, γ's are damping constants, and K is the coupling coefficient. Equations 1 occur in a variety of physical examples such as nonlinear decay of lower hybrid waves in plasmas[1] and laser-plasma interactions.[2] Various approximations of (1) have been studied both numerically and analytically.[3, 4] Recently, Kaup et al.[5] solved Eqs. 1 by the inverse-scattering method when $\gamma_j = 0$, $j = 1, 2, 3$. Here, we solve the equations exactly when $\gamma_1 = \gamma_2 = 0$ and the third mode is so heavily damped that (1c) becomes

$$\gamma_3 a_3 = K^* a_1 a_2^*. \tag{2}$$

If (2) holds, (1a, b) can be rewritten as

$$v_1 I_{1x} + I_{1t} = -I_1 I_2, \qquad v_2 I_{2x} + I_{2t} = I_1 I_2, \tag{3}$$

where $I_1 = (2/\gamma_3)|Ka_1|^2$, $I_2 = (2/\gamma_3)|Ka_2|^2$. Note that (3) can also be derived if mismatch terms arising from inhomogeneities are included in (1). Equations 3 have been solved exactly by Chu[6] and Chen.[7] Solutions I_1 and I_2 are given as

$$I_1 = -\ln\left[Z(\xi)-T(\tau)\right]_\tau, \qquad I_2 = \ln\left[Z(\xi)-T(\tau)\right]_\xi, \tag{4}$$

where $Z(\xi)$ and $T(\tau)$ are arbitrary functions of the independent variables:

$$\xi = (x-v_2 t)/(v_1-v_2), \qquad \tau = (x-v_1 t)/(v_2-v_1).$$

We consider (3) to be the model equations for nonlinear decay of lower hybrid waves into heavily damped electrostatic ion cyclotron waves in a Tokamak plasma.[1] These equations also describe Brillouin backscatter in a laser plasma system.[2]

Using (4), we show that initial- and boundary-value problems can be reduced to the solution of ordinary differential equations. We present general forms for the solution of these equations and plots of the solution in specific cases.

We present, first, the initial-value problem. If the initial values of I_1 and I_2 are $I_1(x,0) = I_{10}(x)$ and $I_2(x,0) = I_{20}(x)$, then we can solve for $Z(\xi(x,0)) = Z(x/V)$ and $T(\tau(x,0)) = T(-x/V)(V \equiv v_1 - v_2)$. Equations 4 yield

$$I_{10} Z_x(x/V) + I_{20} T_x(-x/V) = 0$$

$$Z_x(x/V) - T_x(-x/V) = \left[(I_{10}+I_{20})/V\right] \exp \int_0^x dz\, (I_{10}(z)+I_{20}(z))/V.$$

Then

$$Z(\xi) = \frac{1}{2} + \frac{1}{V}\int_0^{V\xi} dy\, I_{20}(y) \exp \int_0^y dz\, [I_{10}(z)+I_{20}(z)]/V$$

$$T(\tau) = -\frac{1}{2} - \frac{1}{V}\int_0^{-V\tau} dy\, I_{10}(y) \exp \int_0^y dz\, [I_{10}(z)+I_{20}(z)]/V. \tag{5}$$

The analytic solutions for I_1 and I_2 are

$$I_1 = -\left[v_2 \frac{\partial}{\partial x} + \frac{\partial}{\partial t}\right] \ln \left[Z\left(\frac{x - v_2 t}{V}\right) - T\left(\frac{x - v_1 t}{-V}\right)\right]$$

$$I_2 = \left[v_1 \frac{\partial}{\partial x} + \frac{\partial}{\partial t}\right] \ln \left[Z\left(\frac{x - v_2 t}{V}\right) - T\left(\frac{x - v_1 t}{-V}\right)\right]. \tag{6}$$

As an example, consider the collision of two Gaussian wave packets:

$$I_{10}(x) = \frac{2}{\sqrt{\pi}} h_1 \exp - \left[\frac{x + x_1}{w_1}\right]^2$$

$$I_{20}(x) = \frac{2}{\sqrt{\pi}} h_2 \exp - \left[\frac{x - x_2}{w_2}\right]^2$$

We take $V > 0$. If $x_1 + x_2$ is sufficiently large, I_{10} and I_{20} can be considered nonoverlapping and Eqs. 5 may be evaluated to give

$$Z(\xi) = -\frac{1}{2} + \exp\left\{\frac{h_2 w_2}{V}\left[\operatorname{erf}\left(\frac{V\xi - x_2}{w_2}\right) + 1\right]\right\}$$

$$T(\tau) = \frac{1}{2} - \exp\left\{\frac{h_1 w_1}{V}\left[\operatorname{erf}\left(\frac{-V\tau + x_1}{w_1}\right) - 1\right]\right\}.$$

An example of this interaction is plotted in Fig. X-2. Note that for wave 2, the leading edge is amplified more than its trailing edge, since it sees an undepleted wave 1. This effect is generally true for all initial pulses.

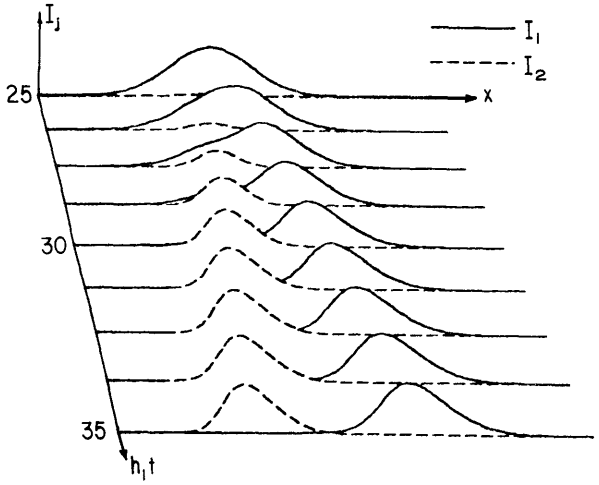

Fig. X-2.
Plot of $I_1(x, t)$ and $I_2(x, t)$ for initial-value problem when $v_2 = -1.2\, v_1$, $h_2 = 10^{-3}\, h_1$, $w_1 = 10\, v_1/h_1$, $w_2 = w_1/2$, $x_1 + x_2 = 60\, v_1/h_1$.

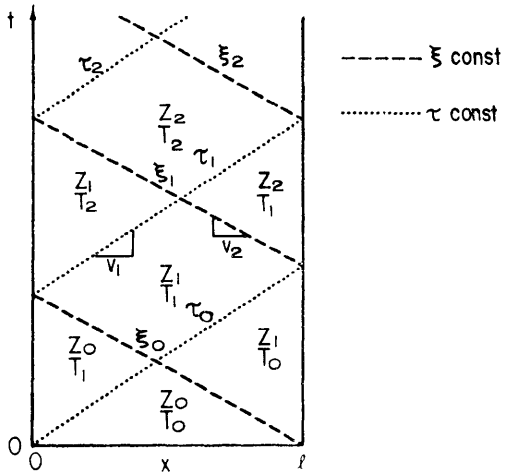

Fig. X-3.
Plot of ξ_n and τ_n in the x-t plane.

From the general expressions (5) for Z and T, we can also calculate the final areas of I_1 and I_2 if initially the pulses are nonoverlapping.

$$A_{1f} + A_{2f} = A_{1i} + A_{2i} \tag{7a}$$

$$A_{2f} = V \log \left[\exp(A_{2i}/V) + \exp(-A_{1i}/V) - 1\right] + A_{1i}. \tag{7b}$$

Here A_{2f} and A_{2i} are the final and initial areas of I_2. Equation 7a is the equation for conservation of action. Equation 7b gives the transfer of action from wave 1 to wave 2 and enables us to calculate the energy dissipated in mode 3. Note that the energy dissipated is independent of the initial shapes of the waves.

In the decay of lower hybrid waves in Tokamaks, the boundary-value problem is more relevant. There are two boundary-value problems that can be solved. If $v_1 > 0$ and $v_2 > 0$, then (3) with the conditions $I_1(0, t) = \mathcal{I}_{10}(t)$, $I_2(0, t) = \mathcal{I}_{20}(t)$, $I_1(x, 0) = I_{10}(x)$, $I_2(x, 0) = I_{20}(x)$, $0 < x < \ell$ can be solved in the same manner as the initial-value problem because I_1 and I_2 are specified on the same lines in x, t space. Moreover, if $v_1 > 0$ but $v_2 < 0$, then the boundary values for (3) become

$$I_1(0, t) = \mathcal{I}_{10}(t), \qquad I_2(\ell, t) = \mathcal{I}_{20}(t) \tag{8a}$$

$$I_1(x, 0) = I_{10}(x), \qquad I_2(x, 0) = I_{20}(x). \tag{8b}$$

By using the method described in solving the initial-value problem, (8b) will give the solution of

$$Z(\xi) = Z_o\left(\frac{x}{V}\right), \qquad 0 < x < \ell, \ 0 < V\xi < \ell$$

$$T(\tau) = T_o\left(\frac{-x}{V}\right), \qquad 0 < x < \ell, \ -\ell < V\tau < 0.$$

At the boundary at x = 0, for $0 < t < -\ell/v_2$, $Z = Z_o(\xi)$ is known. We can solve for $T(\tau) = T_1(\tau)$, for $0 < \tau < -v_1\ell/v_2V$, since from (4a)

$$T_{1\tau} = \mathcal{I}_{10}(V\tau/v_1)[Z_o(-v_2\tau/v_1) - T_1(\tau)].$$

This procedure can be repeated successively at x = 0 and $x = \ell$ to find $Z = Z_n(\xi)$, $\xi_{n-1} < \xi < \xi_n$, and $T = T_n(\tau)$, $\tau_{n-1} < \tau < \tau_n$, where $\xi_o = \ell/V$, $\tau_o = 0$, $\xi_n = (\ell - v_2\tau_{n-1})/v_1$, $\tau_n = -v_1\xi_{n-1}/v_2$. The relationships of τ_n and ξ_n are illustrated in Fig. X-3. The functions Z_n and T_n obey the recursive equations.

$$Z_n(\xi) = \mathcal{I}_n Z_H(\xi) - Z_H(\xi) \int^{\xi} \left\{[\mathcal{I}_{20}[(\ell - V\xi)/v_2]\, T_{n-1}((\ell - v_1\xi)/v_2)]/Z_H(\xi)\right\} d\xi$$

$$T_n(\tau) = \mathcal{T}_n T_H(\tau) + T_H(\tau) \int^{\tau} \{[\mathcal{I}_{10}(V\tau/v_1)\, Z_{n-1}(-v_2\tau/v_1)]/T_H(\tau)\}\, d\tau,$$

where $Z_H(\tau) = \exp\{\int^{\xi} \mathcal{I}_{20}[(\ell - V\xi)/v_2]\, d\xi\}$ and $T_H(\tau) = \exp\{\int^{\tau} - \mathcal{I}_{10}(V\tau/v_1)\, d\tau\}$. The constants of integration $\mathcal{I}_n$ and $\mathcal{T}_n$ are determined by requiring the continuity of $T(\tau)$ and

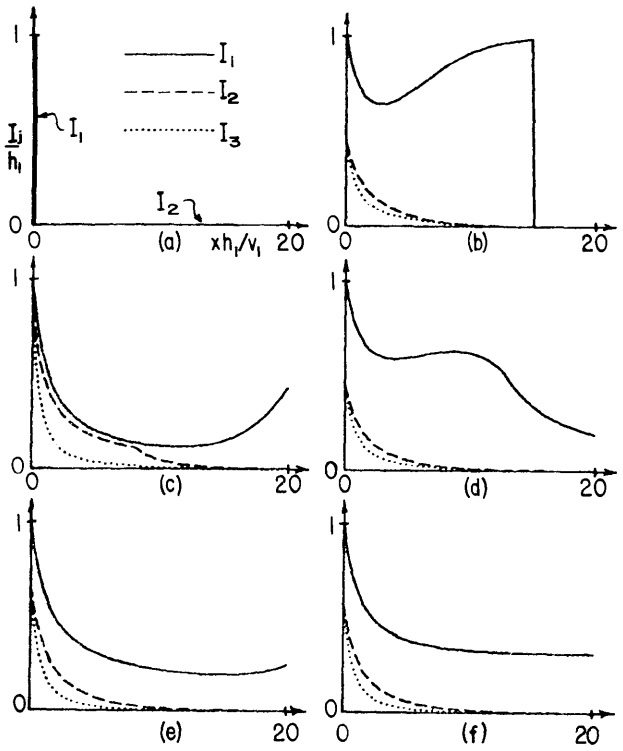

Fig. X-4. Plots of $I_1(x, t)$, $I_2(x, t)$, and $I_3(x, t) \equiv 4|Ka_3|^2/h_1$ for boundary-value problem when $v_2 = -1.2\, v_1$, $\ell = 20\, v_1/h_1$, $h_2 = 10^{-3}\, h_1$, and for various times t. (a) $0/h_1$, (b) $15/h_1$, (c) $30/h_1$, (d) $50/h_1$, (e) $70/h_1$, (f) steady state.

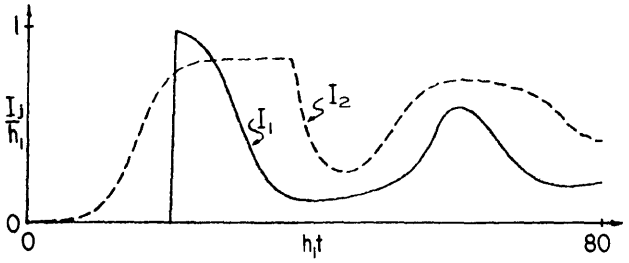

Fig. X-5. Plot of $I_1(\ell, t)$ and $I_2(0, t)$ for boundary-value problem.

$Z(\xi)$. For simple values of the initial and boundary conditions, Z_n and T_n and hence $I_1(x, t)$ and $I_2(x, t)$ can be solved analytically. For example, if $\mathcal{I}_{10}(t) = h_1$, $\mathcal{I}_{20}(t) = h_2$, $I_{10}(x) = 0$, $I_{20}(x) = h_2$ (h_1, h_2 const.), this boundary-value problem describes the growth of wave 2 from noise when wave 1 is turned on at $t = 0$. Figure X-4 illustrates this example. Note that the amplitude of wave 2 oscillates considerably. In Fig. X-5, $I_1(\ell, t)$ and $I_2(0, t)$ are plotted. Both waves oscillate but decay with time until they reach the steady state shown in Fig. X-4f.

We have completely solved both the initial- and the boundary-value problems for (3). In any physical problem, however, it is important to check that the neglect of $v_3 a_{3x} + a_{3t}$ in Eq. 1c is justified. The problem in two dimensions and time can be solved in a similar manner. This will be presented in a later report.

References

1. R. L. Berger and F. W. Perkins, Phys. Fluids 19, 406 (1976).
2. C. S. Liu, M. N. Rosenbluth, and R. B. White, Phys. Rev. Letters 31, 697 (1973).
3. R. W. Harvey and G. Schmidt, Phys. Fluids 18, 1395 (1975).
4. V. Fuchs, Bull. Am. Phys. Soc. 20, 1253 (1975).
5. D. J. Kaup, A. H. Reiman, and A. Bers, RLE Progress Report No. 117, Research
6. Laboratory of Electronics, M. I. T., January 1976, pp. 168-173.
6. F. Y. F. Chu, Phys. Letters 51A, 129 (1975).
7. H. H. Chen, Private communication, 1976.

3. LOWER HYBRID OSCILLATING TWO-STREAM AND MODULATIONAL INSTABILITIES WITH FINITE WAVELENGTH PUMP

National Science Foundation (Grant ENG75-06242-A01)

George L. Johnston, Abraham Bers

Introduction

In order to extend our understanding of the nonlinear effects of propagation of lower hybrid waves in plasma, we present an analysis of the lower hybrid oscillating two-stream and modulational instabilities with finite wavelength pump.

In RLE Progress Report No. 117 (pp. 197-204) we reported a differential equation for the low-frequency particle density modulation induced by the ponderomotive force density in a warm-fluid model under the assumptions of quasi neutrality and extremely low frequency. Only the z-component (the component in the direction of the applied magnetic field) of the sum of the species ponderomotive force density appears in this equation.

We shall give a compact expression for the z-component of the ponderomotive force density resulting from the interaction of cold-fluid normal mode pump and upper

and lower sideband waves through the convective nonlinearity in the species equations of motion under the assumption that the frequency of the externally excited wave satisfies the conditions $\Omega_i \ll \omega_o \ll \Omega_e$. Combining these results yields a compact expression for the low-frequency particle density modulation in terms of high-frequency fields and susceptibility. We also present an equation describing the high-frequency cold-fluid propagation in the frequency range $\Omega_i \ll \omega_o \ll \Omega_e$, including the nonlinear effect of low-frequency particle density modulation. Combining the high- and low-frequency dynamics and introducing appropriate approximations yields a pair of linear homogeneous equations for upper and lower sideband amplitudes coupled by the pump amplitude. Setting the determinant of coefficients of the sideband amplitudes to zero gives the dispersion relation for the oscillating two-stream and modulational instabilities. Introducing the resonant approximation for the linear high-frequency response of the sidebands, we get an approximate form for the dispersion relation. We examine extreme oscillating two-stream and modulational instability limits.

Low-Frequency Particle Density Modulation

The particle density modulation in the plasma induced by the ponderomotive force density is determined from the low-frequency component of the warm-fluid equations. We make the assumptions of quasi neutrality and that the time-harmonic spectral composition of the low-frequency response is very small compared with Ω_i, $k_z C_s$, and $k_z V_{ti}$. Under these assumptions, and combining the species continuity and warm-fluid equations of motion, we previously obtained an equation for the low-frequency particle density modulation n_L as a balance of z-components of ponderomotive force density and pressure gradient

$$(\gamma_e T_e + \gamma_i T_i) \frac{\partial n_L}{\partial z} = F_{eLz} + F_{iLz}. \tag{1}$$

When the functional forms of F_{eLz} and F_{iLz} are introduced, this equation can be integrated to give an expression for n_L.

Ponderomotive Force Density and Resulting Low-Frequency Particle Density Modulation

We want to extract the low-frequency component of the bilinear combination of linear fluid velocity perturbations of a normal mode pump wave and upper and lower sidebands interacting through the convective nonlinearity in the cold-fluid equations of motion, $(\underline{u}_a \cdot \nabla)\underline{u}_a$. We approximate linear susceptibilities at high frequency by making the assumption $\Omega_i \ll \omega_H \ll \Omega_e$, and treat the ions as unmagnetized. Making use of (1), we obtain the component of n_L at frequency ω and wave vector $\underline{k}$.

To implement this program, we consider the interaction of two waves at frequencies

ω_1 and ω_2, where $\omega_1 > \omega_2$. The low frequency is $\omega_3 = \omega_1 - \omega_2$. Results of this formulation are applied to the interaction of the pump and the upper sideband, i.e., $\omega_1 = \omega_o + \omega$, $\omega_2 = \omega_o$, and of the pump and the lower sideband, i.e., $\omega_1 = \omega_o$, $\omega_2 = \omega_o - \omega$.

The z-component of the ponderomotive force density of species α is

$$F_{\alpha Lz} = -n_o m_\alpha [(\underline{u}_\alpha \cdot \nabla) u_{\alpha z}]_L. \tag{2}$$

Here $\underline{u}_\alpha$ is the linear fluid velocity perturbation of species α driven by the high-frequency electric field. The unperturbed species number density is n_o, the mass of species α is m_α, and subscript L denotes the low-frequency component of the bilinear combination. We consider the sum of species fluid velocity perturbations arising from the waves of frequency ω_1 and ω_2,

$$\underline{u}_\alpha = \underline{u}_{\alpha 1} + \underline{u}_{\alpha 2}. \tag{3}$$

We introduce the complex representation

$$\underline{u}_{\alpha 1,2} = \tilde{\underline{u}}_{\alpha 1,2} + \text{c.c.} \tag{4}$$

for the species fluid velocity perturbations and other quantities. The complex amplitudes $\tilde{\underline{u}}_{\alpha 1,2}(\underline{r}, t)$ are expressed in terms of the cold-fluid susceptibility by

$$\tilde{\underline{u}}_{\alpha 1,2}(\underline{r}, t) = \frac{\omega_{1,2}}{4\pi n_o q_\alpha i} \underline{\underline{\chi}}^\alpha_{1,2} \cdot \tilde{\underline{E}}_{1,2}(\underline{r}, t). \tag{5}$$

The complex amplitude of the component of $(\underline{u}_\alpha \cdot \nabla) u_{\alpha z}$ at frequency $\omega_3 = \omega_1 - \omega_2$ is given by

$$[(\tilde{\underline{u}}_\alpha \cdot \nabla) u_{\alpha z}]_3 = (\tilde{\underline{u}}_{\alpha 1} \cdot \nabla) \hat{z} \cdot \tilde{\underline{u}}^*_{\alpha 2} + \left(\tilde{\underline{u}}^*_{\alpha 2} \cdot \nabla\right) \hat{z} \cdot \tilde{\underline{u}}_{\alpha 1}. \tag{6}$$

We seek an expression for $\tilde{F}_{\alpha 3z}$ in terms of the susceptibility and the complex amplitudes $\tilde{\underline{E}}_1$ and $\tilde{\underline{E}}_2$. To achieve this, in combining the various relationships in (2)-(6) we assume $\omega_1 = \omega_2 = \omega_o$. Thus $\underline{\underline{\chi}}^\alpha_1 = \underline{\underline{\chi}}^\alpha_2 + \underline{\underline{\tilde{\chi}}}^\alpha$, where the high frequency that appears in $\underline{\underline{\chi}}^\alpha$ is ω_o. We make use of the fact that $\hat{z} \cdot \underline{\underline{\chi}}^\alpha = -(\omega_{p\alpha}/\omega_o)^2 \hat{z}$ with $\underline{\underline{\chi}}^\alpha$ Hermitian; that is,

$$\chi^\alpha_{ij} = \chi^{\alpha *}_{ji}. \tag{7}$$

From these considerations we arrive at

$$\tilde{F}_{\alpha 3z} = \frac{\partial}{\partial z}\left[\frac{1}{4\pi} (\tilde{\underline{E}}^*_2 \cdot \underline{\underline{\chi}}^\alpha \cdot \tilde{\underline{E}}_1)\right]. \tag{8}$$

We substitute (8) in (1) and perform an integration with respect to z, to obtain the

compact result for the complex amplitude of the particle density modulation at frequency ω_3 induced by the ponderomotive force density resulting from the interaction of waves at frequencies ω_1 and ω_2:

$$\frac{\tilde{n}_3}{n_o} = \frac{1}{4\pi n_o T} \tilde{\underline{E}}_2^* \cdot \underset{\sim}{\chi} \cdot \tilde{\underline{E}}_1, \tag{9}$$

where $T = (\gamma_e T_e + \gamma_i T_i)$ and $\underset{\sim}{\chi} = \underset{\sim}{\chi}^e + \underset{\sim}{\chi}^i$.

Applying (9) to the interaction of the pump and the upper and lower sidebands finally yields

$$\frac{\tilde{n}_L}{n_o} = \frac{1}{4\pi n_o T} \left(\tilde{\underline{E}}_o^* \cdot \underset{\sim}{\chi} \cdot \tilde{\underline{E}}_+ + \tilde{\underline{E}}_-^* \cdot \underset{\sim}{\chi} \cdot \tilde{\underline{E}}_o \right) \tag{10}$$

for the low-frequency particle density modulation. Here subscripts zero, plus, and minus refer to the pump and to upper and lower sideband fields, respectively.

Nonlinear High-Frequency Dynamics

The dominant nonlinearity in the high-frequency dynamics appears in the species continuity equations

$$\frac{\partial n_a}{\partial t} + \nabla \cdot (n_a \underline{u}_a) = 0. \tag{11}$$

Our approximate treatment of the nonlinear high-frequency dynamics is based on approximate replacement in the nonlinear term of n_a with $(n_o + n_L)$ and of $\underline{u}_a$ with the sum of linear species fluid velocity perturbations induced by the pump wave and upper and lower sidebands. We separate the components of this equation at upper and lower sideband frequencies, combine them with Poisson's equation, and express the species fluid velocity perturbations in terms of the susceptibilities evaluated at ω_o and the corresponding complex amplitudes of the pump and sideband fields, to obtain the following pair of equations:

$$\nabla \cdot \left[\underset{\sim}{K} \cdot \tilde{\underline{E}}_+ + \left(\tilde{n}_L / n_o \right) \underset{\sim}{\chi} \cdot \tilde{\underline{E}}_o \right] = 0 \tag{12}$$

$$\nabla \cdot \left[\underset{\sim}{K} \cdot \tilde{\underline{E}}_- + \left(\tilde{n}_L^* / n_o \right) \underset{\sim}{\chi} \cdot \tilde{\underline{E}}_o \right] = 0. \tag{13}$$

Dispersion Relation

It is convenient to express the electric fields in terms of electrostatic potentials. Thus, from (10), (12), and the complex conjugate of (13), we obtain the following set of coupled homogeneous equations for $\tilde{\phi}_+$ and $\tilde{\phi}_-^*$:

$$A\tilde{\phi}_+ + B\tilde{\phi}_-^* = 0 \tag{14}$$

$$C\tilde{\phi}_+ + D\tilde{\phi}_-^* = 0. \tag{15}$$

The quantities A, B, C, and D in (14) and (15) are given by the relations

$$A = \Lambda_+ + \frac{1}{4\pi n_o T}\left[\underline{k}_o \cdot \underline{\underline{\chi}} \cdot (\underline{k}_o+\underline{k})\right]\left[(\underline{k}_o+\underline{k}) \cdot \underline{\underline{\chi}} \cdot \underline{k}_o\right] |\tilde{\phi}_o|^2 \tag{16}$$

$$B = \frac{1}{4\pi n_o T}\left[(\underline{k}_o-\underline{k}) \cdot \underline{\underline{\chi}} \cdot \underline{k}_o\right]\left[(\underline{k}_o+\underline{k}) \cdot \underline{\underline{\chi}} \cdot \underline{k}_o\right] \tilde{\phi}_o^2 \tag{17}$$

$$C = \frac{1}{4\pi n_o T}\left[\underline{k}_o \cdot \underline{\underline{\chi}} \cdot (\underline{k}_o+\underline{k})\right]\left[(\underline{k}_o-\underline{k}) \cdot \underline{\underline{\chi}}^* \cdot \underline{k}_o\right] \tilde{\phi}_o^{*2} \tag{18}$$

$$D = \Lambda_- + \frac{1}{4\pi n_o T}\left[(\underline{k}_o-\underline{k}) \cdot \underline{\underline{\chi}} \cdot \underline{k}_o\right]\left[(\underline{k}_o-\underline{k}) \cdot \underline{\underline{\chi}}^* \cdot \underline{k}_o\right] |\tilde{\phi}_o|^2, \tag{19}$$

in which $\Lambda_\pm = (\underline{k}_o \pm \underline{k}) \cdot \underline{\underline{K}}(\omega_o \pm \omega) \cdot (\underline{k}_o \pm \underline{k})$.

Setting the determinant of the coefficients equal to zero gives the dispersion relation

$$1 + \frac{N_+ |\tilde{\phi}_o|^2}{\Lambda_+} + \frac{N_- |\tilde{\phi}_o|^2}{\Lambda_-} = 0, \tag{20}$$

where $N_\pm = (4\pi n_o T)^{-1} \left|(\underline{k}_o \pm \underline{k}) \cdot \underline{\underline{\chi}} \cdot \underline{k}_o\right|^2$. This dispersion relation may be expressed in a more convenient form by introducing in (20) the quantities $\hat{\Lambda}_\pm = \hat{k}_\pm \cdot \underline{\underline{K}}(\omega_o \pm \omega) \cdot \hat{k}_\pm$ and $\hat{N}_\pm = \left|\hat{k}_\pm \cdot \underline{\underline{\chi}} \cdot \hat{k}_o\right|^2$, where $\hat{k}_\pm = (\underline{k}_o \pm \underline{k})/|\underline{k}_o \pm \underline{k}|$ and $\hat{k}_o = \underline{k}_o/|\underline{k}_o|$. Then we obtain the dispersion relation

$$1 + \frac{E_o^2}{16\pi n_o T}\left(\frac{\hat{N}_\pm}{\hat{\Lambda}_+} + \frac{\hat{N}_-}{\hat{\Lambda}_-}\right) = 0, \tag{21}$$

where E_o is the amplitude of the pump field.

Resonant Approximation for Linear High-Frequency Sideband Response

We introduce the familiar resonant approximation for the linear high-frequency sideband response functions

$$\hat{\Lambda}_\pm \approx \pm 2\omega_o^{-1} S_\pm(\omega - \alpha \pm \delta). \tag{22}$$

The quantities α and δ are defined in terms of the lower hybrid frequencies

corresponding to the wave vectors $(\underline{k}_o \pm \underline{k})$

$$\left(\omega_H^{\pm}\right)^2 = S_{\pm}^{-1}\left(\omega_{pi}^2 + \omega_{pe}^2 \cos^2\theta_{\pm}\right) \tag{23}$$

where

$$S_{\pm} = 1 + (\omega_{pe}/\Omega_e)^2 \sin^2\theta_{\pm} \tag{24}$$

and $\theta_{\pm}$ are the polar angles of $(\underline{k}_o \pm \underline{k})$, by

$$\alpha = \frac{1}{2}\left(\omega_H^+ - \omega_H^-\right) \qquad \delta = \omega_o - \frac{1}{2}\left(\omega_H^+ + \omega_H^-\right). \tag{25}$$

With the resonant approximation, the dispersion relation (21) assumes the approximate form

$$\left[(\omega-\alpha)^2 - \delta^2\right] + P_-(\omega-\alpha) - P_+\delta = 0, \tag{26}$$

where

$$P_{\pm} = \frac{E_o^2}{32\pi n_o T}\,\omega_o\left(\frac{\hat{N}_+}{S_+} \pm \frac{\hat{N}_-}{S_-}\right). \tag{27}$$

The solution of the dispersion relation is

$$\omega - \alpha = -\frac{1}{2}P_- \pm \frac{1}{2}\left[4(\delta^2 + P_+\delta) + P_-^2\right]^{1/2}. \tag{28}$$

We observe that δ must be negative in order to obtain positive values of Im ω.

Approximate Solutions of the Dispersion Relation

In order to find approximate analytic solutions of the dispersion relation (26), we examine the limits $|\underline{k}| \gg |\underline{k}_o|$ (extreme oscillating two-stream instability) and $|\underline{k}| \ll |\underline{k}_o|$ (extreme modulational instability). In these limits, $\hat{N}_+$ and $\hat{N}_-$ differ very slightly from each other, as do S_+ and S_-. Accordingly, we neglect P_- in (28). Assuming that P_+ varies slowly relative to δ, we find that the maximum growth rate is given by $\delta_m = \frac{1}{2}P_+$. This occurs when $\delta = -\frac{1}{2}P_+$.

Limiting Values of Coupling Coefficients

We now examine the values of the coupling coefficients $\hat{N}_{\pm} = \left|\hat{k}_{\pm} \cdot \underset{\sim}{\chi} \cdot \hat{k}_o\right|^2$ in the limiting cases $|\underline{k}| \gg |\underline{k}_o|$ (oscillating two-stream instability) and $|\underline{k}| \ll |\underline{k}_o|$ (modulational

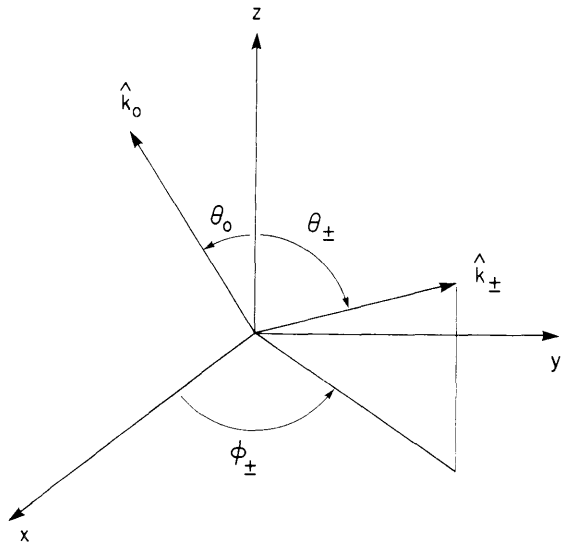

Fig. X-6. Unit wave vectors for pump and sideband waves.

instability). We denote the polar coordinates of $\hat{\underline{k}}_o$ and of $\hat{\underline{k}}_\pm$ by θ_o, $\phi_o = 0$, and $\theta_\pm$, $\phi_\pm$, respectively (see Fig. X-6). In terms of these parameters we have

$$\hat{N}_\pm = (\sin\theta_\pm \cos\phi_\pm \sin\theta_o \chi_\perp + \cos\theta_\pm \cos\theta_o \chi_{||})^2 + \sin^2\theta_\pm \sin^2\phi_\pm \sin^2\theta_o |\chi_x|^2. \quad (29)$$

We recall that $\chi_\perp = 1 + (\omega_{pe}/\Omega_e)^2 - (\omega_{pi}/\omega_o)^2$, $\chi_{||} = 1 - (\omega_{pe}/\omega_o)^2 - (\omega_{pi}/\omega_o)^2$, and $\chi_x = -i\omega_{pe}^2/\omega_o\Omega_e$.

For $|\underline{k}| \gg |\underline{k}_o|$ (oscillating two-steam instability), $\sin\theta_\pm \approx \sin\theta_o$ and $|\cos\theta_\pm| \approx \cos\theta_o$. Thus the coupling coefficients assume the approximate form

$$\hat{N}_\pm \approx (\cos\phi_\pm \sin^2\theta_o \chi_\perp + \cos^2\theta_o \chi_{||})^2 + \sin^2\phi_\pm \sin^4\theta_o |\chi_x|^2. \quad (30)$$

In this limit, $\delta < 0$ is achieved when the polar angle of $\underline{k}$ is somewhat smaller than that of $\underline{k}_o$.

In the case of the lower hybrid wave, $\cos^2\theta_o \lesssim m_e/m_i$, the coupling coefficients are maximized when $\phi_\pm \approx \pi/2, 3\pi/2$ and $\hat{N}_\pm \approx (\omega_{pe}^2/\omega_o\Omega_e)^2$. The maximum value of the growth rate is given by

$$\gamma_m = \frac{E_o^2}{32\pi n_o T}\left(\frac{\omega_{pe}^2}{\omega_o\Omega_e}\right)^2 \frac{\omega_p}{\left(1 + \dfrac{\omega_{pe}^2}{\Omega_e^2}\right)}. \quad (31)$$

This can be written in the more familiar form[1]

$$\frac{\gamma_m}{\omega_o} = \frac{1}{8}\left(\frac{U}{c_s}\right)^2 \left(\frac{\omega_{pi}}{\omega_o}\right)^2 \frac{1}{\left(1 + \dfrac{\omega_{pe}^2}{\Omega_e^2}\right)}, \tag{32}$$

where $U = cE_o/B_o$ and $c_s = (T/m_i)^{1/2}$.

In the case of the electron wave, i.e., $m_e/m_i \lesssim \cos^2\theta_o \leq 1$, if $\cos^2\theta_o \approx 0(1)$, the χ_x term is negligible, and hence $\hat{N}_\pm$ is maximized when $\phi_\pm = 0,\pi$. Then, using the linear dispersion relation, we have $\hat{N}_\pm \approx 1$, and the maximum growth rate is given by

$$\gamma_m = \frac{E_o^2}{32\pi n_o T} \frac{\omega_o}{\left(1 + \dfrac{\omega_{pe}^2}{\omega_e^2}\sin^2\theta_o\right)}. \tag{33}$$

For $|\underline{k}| \ll |\underline{k}_o|$ (modulational instability), $\sin\theta_\pm \approx \sin\theta_o$, $\cos\theta_\pm \approx \cos\theta_o$, and $\cos\phi_\pm \approx 1$, $\sin\phi_\pm \approx 0$.

Using the linear dispersion relation, we have $\hat{N}_\pm \approx 1$ and the maximum growth rate is given by (33). The value of δ is negative when $\underline{k}$ is in the x direction; it is positive when $\underline{k}$ is in the y or z direction. There is a range of directions in which δ may be negative.

References

1. M. Porkolab, MATT-1069, Plasma Physics Laboratory, Princeton University, Princeton, New Jersey, October 1974.

4. NUMERICAL SOLUTION OF MULTIWAVE INTERACTIONS IN THE BEAM-PLASMA INSTABILITY

National Science Foundation (Grant ENG75-06242-A01)

Alan L. Throop, Ronald R. Parker

Introduction

In RLE Progress Report No. 115 (pp. 141-159) we discussed a formalism for studying the nonlinear evolution of the beam-plasma (BP) instability under the influence of the parametric coupling shown in Fig. X-7. The formalism was developed to describe an experiment[1-4] in which a linearly unstable BP wave was observed to grow until its amplitude became sufficiently large that it was able to decay resonantly into a backward-traveling Trivelpiece-Gould (TG) mode and a forward-traveling ion acoustic mode (IA) of the plasma column. The results indicated that when the mode energy of the unstable BP mode is properly treated, the nonlinear interaction must be viewed as a four-wave, rather than a three-wave, interaction. This occurred because the BP mode has two waves, a growing (G) and a decaying (D) wave, which must be carefully distinguished from the fast and slow space-charge waves of the uncoupled electron beam.

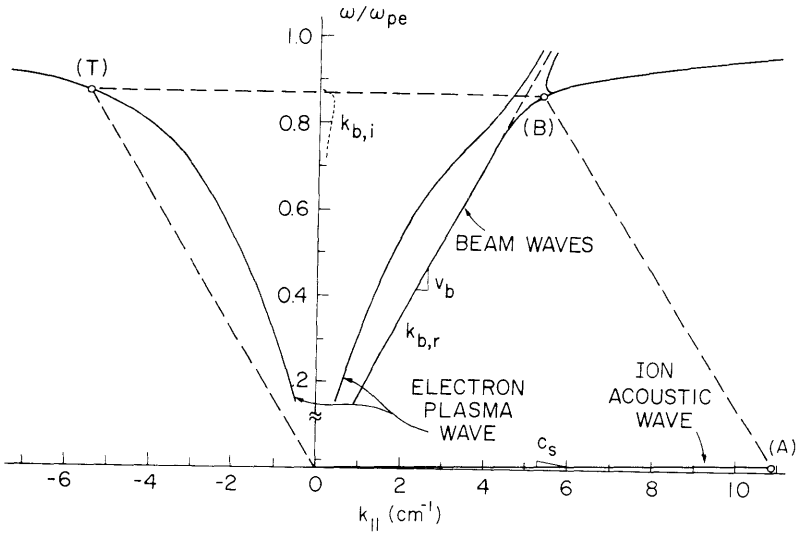

Fig. X-7. Waves involved in the parametric decay instability. (B) = linearly unstable BP wave. (T) = backward-traveling TG mode. (A) = forward-traveling ion acoustic mode.

The interaction is described by the following set of coupled-mode (CM) equations for a system of guided waves under confined flow ($B_o \to \infty$):

$$\left(\frac{d}{dt} + \gamma\right) \tilde{A}_D = j\tilde{K}\tilde{A}_A\tilde{A}_T$$

$$\left(\frac{d}{dt} - \gamma\right) \tilde{A}_G = j\tilde{K}^*\tilde{A}_A\tilde{A}_T$$

$$\frac{d}{dt} \tilde{A}_A = j\tilde{A}_T^*\left(\tilde{K}\tilde{A}_D + \tilde{K}^*\tilde{A}_G\right)$$

$$\frac{d}{dt} \tilde{A}_T = j\tilde{A}_A^*\left(\tilde{K}\tilde{A}_D + \tilde{K}^*\tilde{A}_G\right), \tag{1}$$

where $\frac{d}{dt} \equiv \frac{\partial}{\partial t} + v_{gM} \frac{\partial}{\partial z}$ is the convective derivative with v_{gM} the group velocity of mode M (M = D, G, A or T), $\tilde{A}_M(z, t)$ is the (complex) square root of the action density (w_M/ω_M) of mode M, w_M is the small-signal time-averaged energy density of mode M, γ is the linear growth rate of the BP instability, and $\tilde{K}$ is the (complex) coupling coefficient for the interaction. The complex nature of the coupling coefficient is determined primarily by the expression for the time-averaged small-signal energy of the unstable BP mode, which is given by

$$\tilde{w}_B = \epsilon_o E_D E_G^* \omega \frac{\partial}{\partial \omega} D\Big|_{\tilde{\omega}_B, \tilde{k}_{zB}} \tag{2}$$

where $D(\omega, \bar{k})$ is the dispersion relation and E_D is the normal mode amplitude of the electric field. The stability of the system is determined by the sign Re $(\tilde{w}_B)$, or equivalently by the phase angle of the coupling coefficient. For the particular waves of interest in this experiment the coupling coefficient[4] is given by

$$\tilde{K} \approx \frac{\omega_{pe}}{2v_A} \frac{k_A}{k_{zA}} \left(\frac{\omega_A}{2\omega_T} \frac{\omega_B}{m_i n_o}\right)^{1/2} \frac{\omega_{pe}}{k_B \tilde{v}_B} \frac{1}{\tilde{F}_{w_B}^{1/2}} \tag{3}$$

where capitalized subscripts denote relevant modes, $v_M \equiv \omega_M/k_{ZM}$ is the phase velocity of mode M, and $\tilde{F}_{w_B}$ is a factor arising from $\tilde{w}_B$ given by

$$\tilde{F}_{w_B} = \left(1 - \frac{v_{te}^2}{\tilde{v}_B^2}\right)^{-2} + \frac{m_e}{m_i} - \eta\left(\frac{v_b}{\tilde{v}_B} - 1\right)^{-3}, \tag{4}$$

where v_b is the dc beam velocity, v_{te} is the electron thermal velocity, and $\eta = n_b/n_o$ is the ratio of beam density to plasma density.

In this report we consider the nonlinear solution to the time-independent and

space-independent sets of CM equations that can be obtained from Eqs. 1. At first, we might conclude that an analysis of the time-independent set of CM equations would be directly relevant to the experiment, which is operated in steady state in time. But on the basis of previous work concerning the analogous three-wave backscatter problem,[5,6] it seems likely that, in order to determine the exact final state of the system predicted by this model, a study of the complete set of partial differential equations describing the evolution of the modes in both time and space should be made. Nevertheless, considerable insight concerning the stability of the nonlinear interaction and the scaling of mode saturation levels with system parameters can be obtained from the simpler set of ordinary differential equations where either space or time derivatives are set to zero in Eqs. 1. We shall consider these questions, and then deal with the relevance of the results to our experiment and to other experiments in which beam trapping has been observed to be the dominant saturation mechanism. We only summarize the results of numerical integration of the CM equations; a more complete treatment has been given elsewhere.[4]

Space-Independent Equations

To simplify the set of Eqs. 1 for numerical integration, we choose to undimensionalize the equations and assume that $A_A(t=0) = A_T(t=0)$. This assumption is physically reasonable and implies that the A and T modes are equal for all time, so that the number of CM equations is reduced from four to three. Normalizing the mode amplitudes to the initial amplitudes of the A mode, we obtain the following set of space-independent CM equations from Eqs. 1:

$$\left(\frac{\partial}{\partial\tau} + \Gamma\right)\tilde{D} = j\, e^{j\theta_K}\tilde{A}^2$$

$$\left(\frac{\partial}{\partial\tau} - \Gamma\right)\tilde{G} = j\, e^{-j\theta_K}\tilde{A}^2$$

$$\frac{\partial}{\partial\tau}\tilde{A} = j\tilde{A}^*\left(\tilde{D}\, e^{j\theta_K} + \tilde{G}\, e^{-j\theta_K}\right), \tag{5}$$

where

$$\tau \equiv |K|\,|A_A(0)|\,t \qquad \Gamma = \gamma/|K|\,|A_A(0)|$$

$$K = |K|\, e^{j\theta_K} \qquad \tilde{D}(\tau) \equiv \tilde{A}_D(\tau)/|A_A(\tau=0)|, \text{ etc. for } \tilde{G}, \tilde{A}.$$

This form of the CM equations suggests that the nonlinear stability of the equations depends strongly on the phase angle of the coupling coefficient θ_K, since it determines

the sign of the nonlinear term.

These equations have been numerically integrated in terms of the amplitudes and phases of the modes, by using a linear multistep predictor-corrector package.[7] This package has been modified to operate interactively on the M. I. T. MULTICS system, with the output displayed graphically. Conservation equations derived from the CM equations are evaluated at each time step to insure that the integration proceeds accurately. Reasonable initial conditions relevant to the experiment are calculated by using a fluctuation-dissipation theorem.[4] We shall show, however, that the more important results, such as the nonlinear stability of the interaction and the maximum field strength of the BP mode, are relatively insensitive to the initial values of the mode amplitudes.

Figure X-8 shows typical plots of the evolution of the mode amplitudes obtained by numerical integration of the equations for cases in which θ_K lies in stable and unstable regions. For $\theta_K < 45°$, which corresponds to Re $(\tilde{w}_B) > 0$, the system exhibits stable nonlinear oscillations; for $0° < \theta_K < 45°$, the evolution is such that the amplitude of the G mode always remains larger than its initial value, thereby resulting in a waveform similar to that predicted by beam-trapping theory. For $\theta_K \geq 45°$, which corresponds to Re $(\tilde{w}_B) < 0$, the nonlinear coupling of modes results in an explosive growth of all modes. Note that in both cases the decaying BP mode reaches amplitudes fully as large as that of the initially growing BP mode, so that the interaction must be viewed in general as a four-wave, rather than a three-wave, coupling [the results shown here are for the special case $A(\tau) = T(\tau)$]. The behavior of these numerical results is supported by an analytical study of a simplified subset of Eqs. 5.

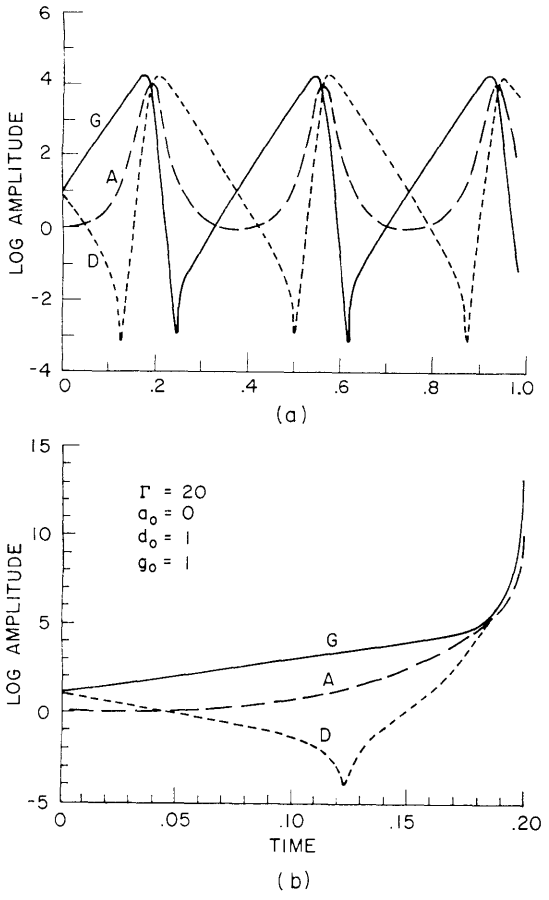

Fig. X-8.
Time evolution of D, G, and A (=T) modes for (a) stable case ($\theta_K = 0°$) and (b) explosive case ($\theta_K = 45°$).

An extensive study of the dependence of the maximum field strength of the BP mode on the initial mode amplitudes reveals a weak scaling, while the

dependence on the normalized growth rate of the BP mode indicates a linear scaling. The dependence on the phase angle of the coupling coefficient, however, revealed the strong scaling shown in Fig. X-9. While the linear growth of the BP mode is stabilized by its parametric decay for all values of $\theta_K < 45°$, it is clear that the saturated field strength

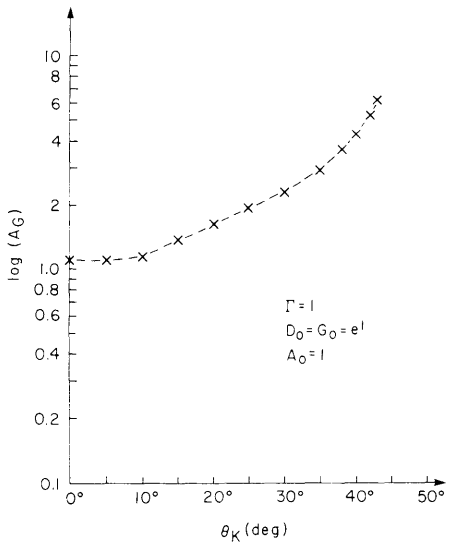

Fig. X-9.

Maximum amplitude of the BP wave vs the phase angle of the coupling coefficient determined by numerical integration of the space-independent equations.

becomes greatly enhanced for values of θ_K greater than approximately 10°. This suggests that a situation might exist wherein wave-wave effects could limit the growth of the BP mode for conditions of $\theta_K \approx 0°$, although other mechanisms could dominate for conditions of larger values of θ_K where the maximum BP wave amplitude caused by wave-wave effects is large.

Time-Independent Equations

The time-independent set of CM equations where we let $\partial/\partial t = 0$ is considerably more complicated than the space-independent case because of the negative group velocity of the TG mode. A conservation relation that allows the T equation to be eliminated cannot be derived; instead, the direct spatial analog to the time equations predicts

$$C_1 |T|^2 + C_2 |A|^2 = \text{constant} \tag{6}$$

where C_1 and C_2 are positive constants. This means not only that the nonlinear wave coupling cannot destabilize the linear growth of the BP mode but also that it cannot be used to conclude whether the coupling will stabilize the linear growth and we must resort to numerical methods to study the stability of the interaction. A solution to the CM equations that is relevant to the experiment, as well as exhibiting stable behavior, must

satisfy the required boundary conditions on the TG mode amplitude; that is, that the TG mode be small at some point downstream from the region of linear growth of the BP mode:

$$T(\ell) \approx 0 \tag{7}$$

where $x = \ell$ is some downstream position in the system.

The set of four time-independent CM equations, when normalized in the form of Eqs. 5, can be shown to resemble the usual three-wave backscatter problem. For the four-wave case, we can combine the equations for the D and G modes into an equation for a single BP mode (denoted B), which initially acts as a pump for the wave coupling.[4] For the simple case $\theta_K = 0$, we can compare the equations for the mode amplitudes (where $A = a\, e^{j\theta_a}$, etc.) for the two cases:

$$\begin{aligned} &\text{three-wave:} \quad \dot{b} - \Gamma b = -at \\ &\text{four-wave:} \quad \dot{b} - \Gamma^2 \int b\, dx = -at \end{aligned} \tag{8a}$$

or

$$\begin{aligned} &\text{three-wave:} \quad \ddot{b} + (t^2 - a^2)b - \Gamma \dot{b} = 0 \\ &\text{four-wave:} \quad \ddot{b} + (t^2 - a^2)b - \Gamma^2 b = 0, \end{aligned} \tag{8b}$$

where $\dot{b}$ denotes the spatial derivative. Note that, although we have added a linear growth to the pump for the three-wave case, it does not affect the time-asymptotic behavior of the interaction.[5] The similarity of Eqs. 8 for the two cases suggests that if the Γ^2 term in the four-wave equation in Eq. 8a could be shown to integrate to zero or otherwise become negligible, then a stable, unperiodic, time-asymptotic state would be expected for both cases. Equations 8b illustrate, however, that the three-wave case can be expected to reach a turning point in the BP mode amplitude before the four-wave case. The similarity between the three- and four-wave cases can also be seen in a numerical integration of the four-wave CM equations for $\Gamma \equiv 0$.[4]

In order to introduce a turning point in the four-wave CM equations, we found it necessary to include linear damping of the T mode.[4] At the same time the results gave well-defined regions of linear and nonlinear behavior for the modes and yielded solutions that satisfied the required boundary conditions on the T mode. Figure X-9a shows the result of integrating the four CM equations, where $T(x = 0)$ has been chosen to give a solution where $T(\ell) = 0$. It can be seen that the linear growth of the total BP mode has been significantly reduced by the effects of the wave coupling. Clearly defined regions of linear and nonlinear behavior also exist. This behavior represents a typical stable solution which can be found for the time-independent CM equations for any given set of

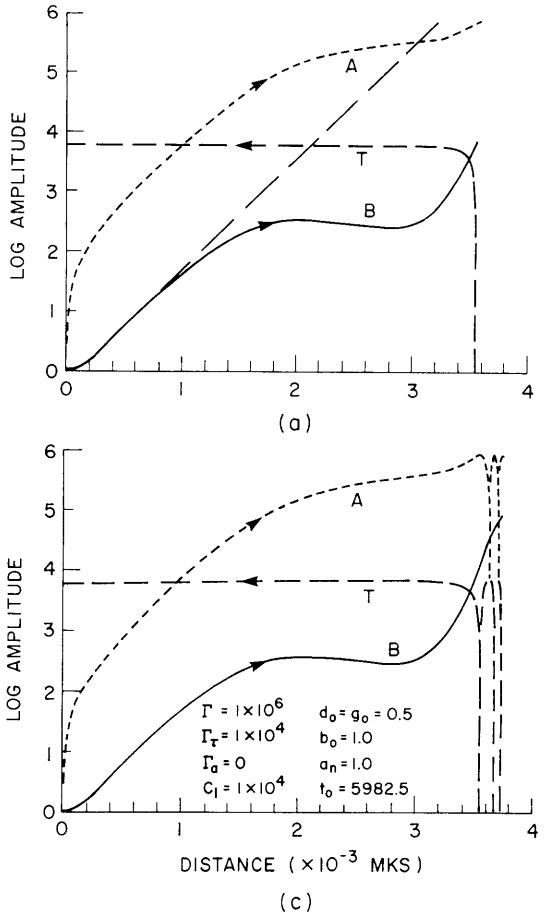

Fig. X-10. Numerical solution of the time-independent equations, evaluated for experimental parameters, showing (a) reduced growth rate of the BP mode and (b) behavior for longer distances.

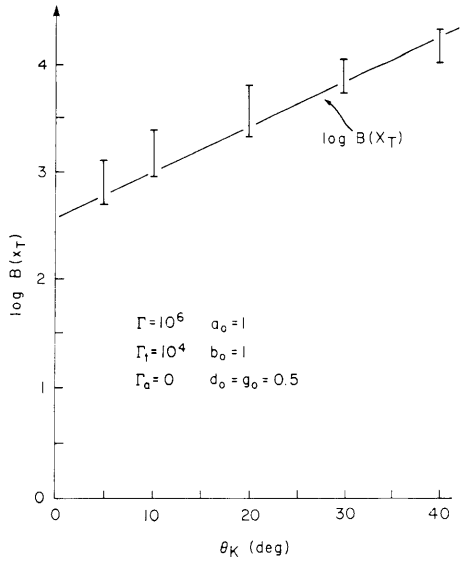

Fig. X-11.

Dependence of the maximum amplitude of the BP wave on the phase angle of the coupling coefficient for the time-dependent equations.

input conditions. Figure X-10b shows that for the region of space outside that of interest in this problem the BP mode resumes its linear growth while the A and T modes oscillate at a rate proportional to the amplitude of the B mode. It seems likely, in analogy with the three-wave results, that an evaluation of the time-asymptotic spatial state would show the region of rapid oscillations reduced to monotonic decay of the mode amplitudes.

As in the time case, a study of the scaling laws of the spatial equations can be made by taking as a measure of the maximum wave amplitude the value of the BP mode amplitude where $\dot{B} = 0$. The results for the time and space equations are similar, as illustrated in Fig. X-11 where the same strong dependence of the maximum field strength on θ_K is indicated for the spatial case. For $\theta_K \geq 45°$, no conditions were found where the linear growth of the BP mode was reduced by the wave coupling.

Application of Time- and Space-Independent Results to Experiments

Our results have suggested that wave-coupling effects can stabilize the linear growth of the unstable BP wave, provided the proper conditions on the coupling coefficient exist. We shall now discuss the manner in which the coupling coefficient varies with several experimental parameters for the experiment that we have discussed and for typical beam-trapping experiments.

Figure X-12 shows the dependence of the magnitude and phase of the coupling coefficient, as well as the linear growth rate of the BP mode, on operating frequency for several values of plasma density. For high-density cases, we find $\theta_K \approx 0$ near the maximum growth rate, while low-density cases never have a region where θ_K is small. Therefore, for the higher density case we expect that wave-coupling effects could dominate the evolution of the BP mode at frequencies near the maximum growth rate, while other mechanisms might dominate at other frequencies. This is similar to the observations of Jones, Carr and Seidl, who observed that the decay instability saturated the growth of the BP mode at frequencies near the maximum growth of the linear instability, while beam trapping appeared to dominate at off-resonance frequencies.[8]

Figure X-12 also suggests the sensitivity of the coupling coefficient to such experimental operating conditions as beam energy, beam current, plasma density, and plasma radius. For a fixed operating frequency, the value of θ_K is sensitive to variation of all of these parameters except beam current. The variation of θ_K with beam energy is shown specifically in Fig. X-13, for conditions relevant to the experiment in which the parametric decay instability was observed. θ_K remains small for the higher range of beam energy, but approaches $-45°$ for small beam energies. The small level of saturated field strength which is therefore indicated for higher beam energies relative to that at lower beam energies is consistent with the experimental observations.[5]

In the past, several experiments were performed which determined conclusively

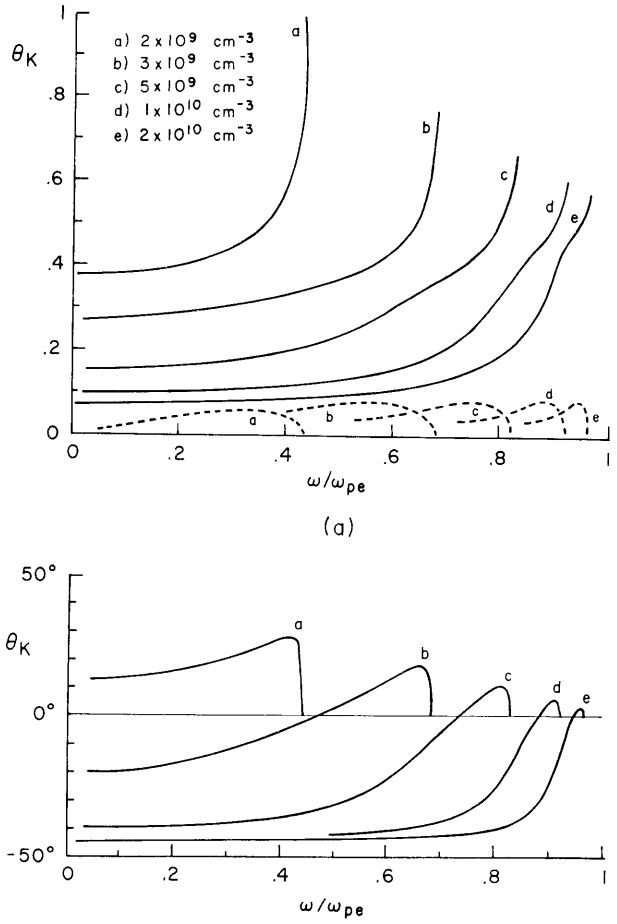

Fig. X-12. Magnitude and phase of the coupling coefficient vs frequency for several values of background plasma density.

(a) $|K|$ ($\times 10^{14}$ MKS) ——— I_b = 1 mA T_e = 5 eV

Im (k_z)/Re (k_{z0}) - - - - U_b = 500 V $k_\perp$ = 210 m^{-1}

(b) < K (deg)

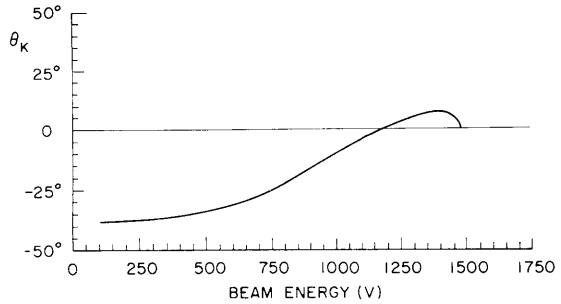

Fig. X-13.

Phase angle of coupling coefficient vs beam energy evaluated for experimental parameters.

I_b = 1 mA $n_o = 3 \times 10^{10}$ cm^{-3}

ω/ω_{pe} = .9 $k_\perp$ = 210 m^{-1}

Table X-1. Experimental parameters of several beam-trapping experiments.

Author	n_o (cm^{-3})	U_b (V)	f_o (MHz)	f_o/f_{pe}
Gentle[9]	1×10^9	300	140	0.50
Nyack[10]	3×10^8	100	96	0.62
DeNeef[11]	5×10^8	150	131	0.67
Malmberg[12]	5×10^8	100	145	0.73

that beam-trapping is the dominant mechanism in the stabilization of the growth of the BP mode. We must question how to reconcile the lack of observation of the decay instability in these experiments with the present case. Table X-1 summarizes the operating conditions of several experiments. It is interesting to note that conditions of low plasma density, slow electron beams, and a ratio of operating frequency (corresponding to the maximum growth rate) to plasma frequency that is significantly less than unity are common features that seem to be typical of most trapping experiments involving the BP instability of the lower plasma branch. A numerical evaluation of the linear dispersion characteristics for several of these experiments confirms that the low plasma density used in these experiments consistently results in the low-density behavior seen in Fig. X-11. This suggests that the lack of stabilizing wave-wave effects is due to the large nonzero value of θ_K.

Figure X-14 illustrates how a transition in saturation mechanisms with beam energy, which was suggested in the present experiment,[4] might be observed. We have used the numerically derived scaling laws for the spatial equations and the expression for the threshold for beam trapping,

$$E_{trap} \approx 2k_B m_e v_b^2 \left(1 - \frac{v_B}{v_b}\right)^2,$$

to plot the relative wave amplitudes that are expected for the two mechanisms. For higher beam energies, the numerical results suggest a saturation level of approximately 1 V/cm because of the decay instability, while the saturation level for beam trapping is approximately 50 V/cm. In this range, therefore, we expect that wave-wave effects will dominate over trapping; for lower beam energies, beam-trapping effects should begin to appear as the trapping threshold decreases simultaneously with the increase in the saturation level because of the decay instability.

These results suggest that early in the development of the BP instability

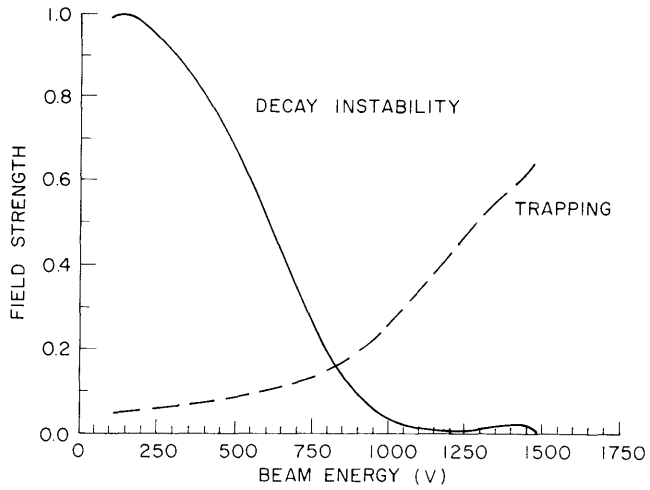

Fig. X-14. Saturated field levels of the BP wave caused by decay instability and beam trapping as a function of beam energy.

E_{trap} ($\times$ 100 V/cm) ---- I_B = 1 mA $n_o = 3 \times 10^{10}$ cm^{-3}

E_{PDI} (relative) —— $\omega/\omega_{pe} = .9$ $k_\perp = 210$ m^{-1}

wave-coupling effects may be important and dominate over beam trapping as a saturation mechanism for a broad range of interesting experimental conditions. The results predicted on the basis of the four-wave model for the parametric interaction seem consistent with experiments, and suggest that the mode energy of an unstable wave participating in such nonlinear interactions must be carefully defined. Further analysis of the space-time behavior of the solutions to Eqs. 1 is needed, however, before these results may be considered conclusive.

References

1. R. R. Parker and A. L. Throop, Quarterly Progress Report No. 108, Research Laboratory of Electronics, M.I.T., January 15, 1973, pp. 154-167.

2. R. R. Parker and A. L. Throop, Phys. Rev. Letters 31, 1549 (1973).

3. A. L. Throop, "Coupled-Mode and Parametric Interactions in a Beam-Plasma System," S.M. Thesis, Department of Electrical Engineering, M.I.T., February 1974.

4. A. L. Throop, "The Influence of Four-Wave Parametric Interactions on the Nonlinear Evolution of the Beam-Plasma Instability," Ph.D. Thesis, Department of Electrical Engineering and Computer Science, M.I.T., May 1976.

5. R. Harvey and G. Schmidt, "Three-Wave Backscatter in a Finite Region," Stevens Institute of Technology Report 000-3004-6 (1974).

6. V. Fuchs and G. Beaudry, "Nonlinear Parametric Decay Interactions in Finite Homogeneous Plasmas" (to appear in J. Math. Phys.).

7. A. Hindmarsh, "Gear: Ordinary Differential Equation System Solver," Lawrence Livermore Laboratory Report UCID-30001 (1972).

8. R. Jones, W. Carr, and M. Seidl, "Beam Trapping Subsequent to the Parametric Pump Depletion Saturation of a Beam-Plasma Instability," Phys. Fluids 19, 607 (1976).

9. K. Gentle and J. Lohr, Phys. Fluids 16, 1464 (1973).

10. C. Nyack and P. Christiansen, Phys. Fluids 17, 2025 (1974).

11. C. P. DeNeef, J. H. Malmberg, and T. M. O'Neil, Phys. Rev. Letters 30, 1032 (1973).

12. J. Malmberg and C. Wharton, Phys. Fluids 12, 2600 (1969).

5. GIANT MICROWAVE BURSTS EMITTED FROM A FIELD-EMISSION, RELATIVISTIC e-BEAM MAGNETRON

National Science Foundation (Grant ENG75-06242-A01)
U.S. Energy Research and Development Administration (Contract E(11-1)-2766)

George Bekefi, Thaddeus J. Orzechowski

Advances in high-voltage pulse technology permit the generation of intense relativistic beams of electrons ranging in power from gigawatts to terawatts. Efficient conversion of this energy into electromagnetic radiation is a challenging task that is being pursued at several laboratories. In these studies an attempt is made to excite one of several known collective modes of oscillation on the beam and promote wave growth at the expense of the beam kinetic or potential energy. The techniques that have been employed fall roughly into three categories. In the first, strong axial bunching[1-3] is induced on the relativistic beam. In the second, the beam electrons are made to bunch transversely[4-7] to a guiding axial magnetic field. In the third,[8,9] modes of oscillation are used that are typical of "crossed-beam" devices[10-12] of which the magnetron is the best known example. Here the electron beam moves under the simultaneous action of a dc electric field and an orthogonal dc magnetic field. The well-known efficiency[11] of crossed-beam devices operating with convectional thermionic cathodes of relatively low current densities has stimulated us to apply these ideas to the regime of high currents and high voltages that are characteristic of field-emission diodes. Indeed, the magnetron described in this report has surpassed all expectations, yielding an unprecedented[13] power of ~1.7 GW; the efficiency of converting beam to microwave energy was close to 35%.

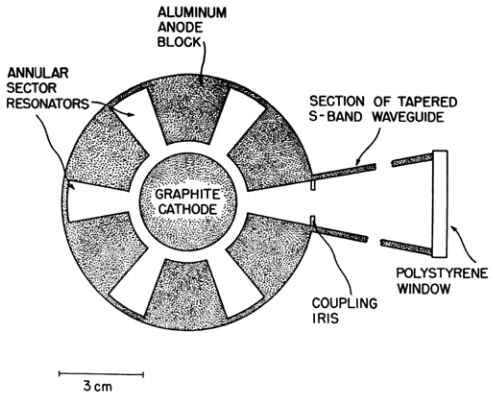

Fig. X-15. Schematic of the cylindrical diode. The scale gives only the correct diode dimensions. The size of the transmitting horn is given in the text.

The cylindrical vacuum diode is illustrated in Fig. X-15. The aluminum anode block has an inner radius of 2.1 cm; it is 9.4 cm long. Cut within the block are six vane-type (sectoral) resonators[10] designed to oscillate at a frequency of 3.0 GHz. Each resonator is 7.2 cm long; one of the resonators is provided with a long slot through which the radiant energy is coupled into a microwave horn, via a section of flared, S-band waveguide. The horn is 43 cm long and has a rectangular aperture that is 17 cm wide in the E-plane and 23 cm wide in the H-plane. The inner coaxial cathode cylinder, 4.8 cm long and 1.58 cm in radius, is machined from dense, fine-grained graphite. Cathodes with radii up to 1.76 cm have also been tried, but their use led to less microwave emission. The cathode is connected via a stainless-steel shank to the inner conductor of the water-filled coaxial capacitor that serves as the transmission line of the 4 Ω Nereus high-voltage facility (maximum voltage ≈ 600 kV). The anode is connected to the grounded wall of the capacitor. The entire system, including the transmitting horn, is continuously pumped to pressures better than 10^{-4} Torr.

The axial magnetic field B_z acting on the diode is generated by two solenoids, mounted in an approximate Helmholtz-pair configuration. The magnetic field is nearly uniform over the entire length of the cathode cylinder. Provision is made, however, for a slight rise in the magnetic field at the two ends of the cathode. The resulting "magnetic mirror" arrangement is probably beneficial in stabilizing the axially rotating electron space-charge cloud of the magnetron. The solenoids are energized by a capacitor bank whose rise time is ~6 ms. The discharging of this bank is timed in such a way that B_z reaches its peak value when Nereus fires. Thus the magnetic field is virtually constant in time over the duration of the ~35 ns voltage pulse applied across the diode. The aluminum anode block is not solid but, as well as the six resonators, is pierced with several large vacuum holes whose purpose is to reduce the amount of metal through which the magnetic field has to diffuse. The ensuing "thin-walled" construction of the anode block ensures good penetration of the pulsed magnetic field into the diode interior. A magnetic field as high as 12 kG can be generated; its strength is controlled by the charging voltage on the capacitor bank. The solenoid current is monitored by means of a precision current probe which, after calibration, yields values of B_z with an accuracy of ~5%.

The diode current is measured with a rapidly responding Ragowski coil wound around the steel shank that connects with the cathode and its output is displayed on a fast oscilloscope. The diode voltage is obtained from the signal delivered by a calibrated copper sulphate voltage divider network and is likewise displayed on an oscilloscope. There is an unwanted inductive contribution to this voltage that is subtracted out by a technique that has been described elsewhere.[8,9]

Typical time histories of the voltage and the current are shown in the top two oscilloscope traces of Fig. X-16 for the case of a 7.5 kG axial magnetic field. At this

magnetic field the diode is magnetically insulated, an azimuthally rotating space-charge field is established, and microwave emission is expected. The lower trace in Fig. X-16 shows the microwave signal output from the crystal detector. To bring the emitted

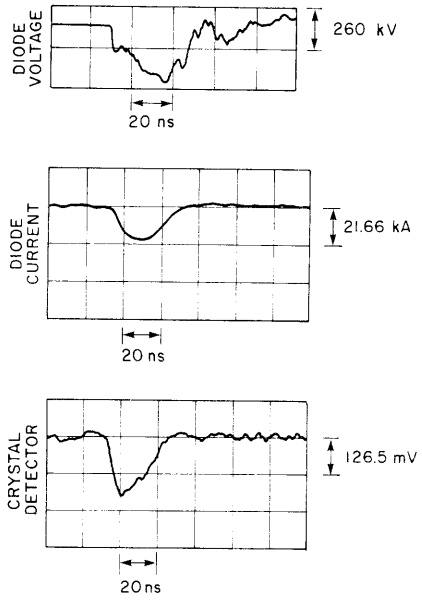

Fig. X-16.

Oscilloscope traces of the diode voltage (corrected for inductive effects), of the diode current, and of the voltage output from the microwave crystal detector. B_z = 7500 G.

power (~1.7 GW) to reasonably low levels to be measurable by the crystal detector, we employed the following microwave arrangement. A receiving antenna (a section of open S-band waveguide) was placed facing the transmitter and 4.0 m from it (a distance that places both antennas in each other's radiation field). A total of 80 dB of precision attenuators further reduced the radiation to levels typically in the milliwatt range. This power was allowed to impinge on a previously calibrated broadband crystal detector. Knowledge of the antenna gains and of their separation allows computation[14] of the desired P_t/P_x ratio where P_t is the power transmitted by the horn and P_x the power measured by the crystal. As a check on this procedure, we injected a known 10-cm wavelength signal into the horn transmitter from a conventional cw klystron and, using the same receiving antenna placed at the identical distance of 4 m, we measured P_x at the crystal detector. In this way an independent determination of the P_t/P_x ratio was obtained which did not require knowledge of the antenna gains (quantities that often are not easy to measure with precision). The agreement between the two methods was better than 10%. On the basis of this and other such tests we can assert that P_t is known with an accuracy of 20% or better. At the typical power levels of these measurements (~1.7 GW), air breakdown in front of the transmitting horn becomes a worrisome problem. On occasion, fairly erratic voltage signals from the crystal detector (not accompanied by similar erratic current traces) suggested to us that air breakdown may indeed have

taken place. We were not generally beset by this difficulty, however, primarily because of the rather short pulse length[15] (30-35 ns) of the microwave radiation.

In Fig. X-17 the peak currents and voltages, obtained from traces like those shown in Fig. X-16, are plotted as a function of the externally applied magnetic field B_z. When

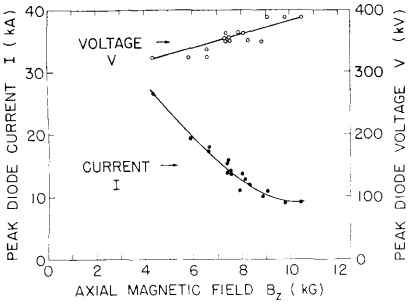

Fig. X-17.

Peak diode voltage and current as a function of magnetic field, as measured in the cutoff regime $B_z \geq B^*$.

B_z is zero, I is typically 35 kA and V ≈ 260 kV, thereby giving a diode impedance equal to 7.4 Ω. As B_z increases from zero, a critical magnetic field $B_z \equiv B^*$ is reached at which point the diode is said to be magnetically insulated,[8,9] and ideally no current should flow across the diode. For our voltages, geometry, and gap spacing (d = 5.2 mm), B^* = 4800 G. That substantial current does flow in the forbidden regime, $B_z \geq B^*$, is one of the classical properties of all magnetrons.[8,9,11] It signifies, in fact, that "non-conservative" oscillatory processes must occur. Thus strong onset of microwave emission is expected at this critical magnetic field. Figure X-17 also shows that as B_z is increased beyond B^* the diode current keeps falling, and the diode voltage increases slightly. These trends are manifestations of the fact that with increasing magnetic field, the diode impedance increases, and becomes more and more mismatched relative to the 4 Ω nominal impedance of the Nereus generator.

In the cutoff regime ($B_z > B^*$), an equilibrium, azimuthally rotating cloud characterized by a radially dependent drift $\vec{v}_d(r) = \vec{E}(r) \times \vec{B}/B^2$ is established. The six equally spaced microwave cavities cut in the anode block act as a slow-wave structure permitting the establishment of a wave whose phase velocity v_p approximately equals the drift velocity $v_d(r)$ of a "resonant" electron layer. Under these conditions, efficient transfer of energy from the beam to the wave can occur. It is clear that for a fixed diode geometry and for a fixed diode voltage V, the magnetron can only oscillate over a limited regime of magnetic fields. The minimum field is $B_{min} = B^* \approx 4800$ G. The maximum field B_{max} is determined by the drift velocity v_d of the fastest (outermost) electron layer. Using the theory developed by Ott and Lovelace,[16] we find that for our situation $B_{max} \approx 1.75\ B^* = 8400$ G. The lower trace in Fig. X-18 shows that significant microwave emission is indeed limited to a rather narrow range of magnetic fields, whose magnitudes are in good accord with theory.[16] The peak emission reaches a value of ~1.7 GW. The

upper curve in Fig. X-18 (broken line) represents the power in the electron beam as derived from the results of Fig. X-17. The peak conversion efficiency is nearly 35%.

The frequency spectrum of the short microwave burst has not yet been measured because a suitable S-band dispersive line is not available at this time. But we have made

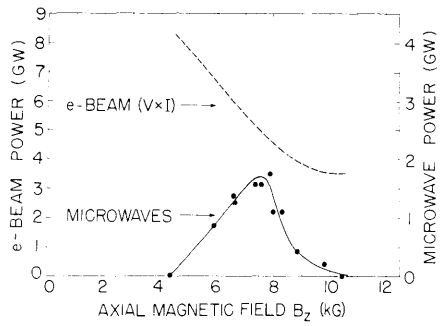

Fig. X-18.
Microwave power output and e-beam power as a function of magnetic field.

an indirect determination of the resonant frequency as follows: with the magnetron in place, we removed the transmitting horn and injected a low-power cw microwave signal of variable frequency into the diode structure. A strong absorption resonance at the design frequency of 3.0 GHz was observed. Since no other neighboring resonances were seen, we are impelled to conclude that the emission frequency likewise was close to 3 GHz. The width of the resonance at the half-power point was ~80 MHz, which suggests that under normal operating conditions the microwave bursts were emitted within a 3000 MHz ± 40 MHz frequency band.

The frequency response of the magnetron has been corroborated by using an instrument designed and built by Professor Louis D. Smullin. This instrument is a low-pressure discharge tube filled with argon to a pressure of approximately 1 Torr placed between 2 Alnico bar magnets positioned in such a way that it produces a magnetic field oriented perpendicular to the discharge tube axis. The spacing between the two bar magnets increases with axial distance along the discharge tube. Thus the discharge tube is acted upon by a nonuniform transversed magnetic field varying from 900 gauss at one end of the tube to 1400 gauss at the other end. This instrument was placed in the microwave beam with the RF field oriented along the discharge tube axis. The gas broke down at the axial position where the electron cyclotron frequency was equal to the frequency of the electromagnetic wave incident on the instrument. By taking an open-shutter photograph of the discharge tube, a bright spot was observed corresponding to electron cyclotron breakdown. Since the magnetic field was known at every point along the discharge tube, the wave frequency was determined by setting $\omega = \omega_c = eB/m$.

In conclusion, we have reported the successful operation of an efficient, relativistic e-beam magnetron employing a field emission cathode capable of supplying currents with densities (prior to cutoff) as high as ~1 kA/cm^2. We plan to investigate the scaling laws

and operating parameters of this and similar crossed-beam devices at even higher currents and voltages, where relativistic effects are expected to be more prominent. It is conceivable that powers in the terawatt range could be generated by such devices. We wish to point out that crossed-beam, field-emission systems may well be amenable to long pulse operation, typically of the order of 1 μs. This is a result of the built-in magnetic field oriented parallel to the cathode and anode surfaces. The strong field inhibits[7,8] motion of cathode and anode plasmas that, if left to themselves, eventually lead to diode closure, that is, to the electrical shorting of the system. Devices like those previously described[1-7] do not have this built-in feature and long pulse operation may be impossible.

References

1. N. F. Kovalev, M. I. Petelin, M. D. Raizer, A. V. Smorgonskii, and L. E. Tsopp, Zh. Eksp. Teor. Fiz. Pis'ma Red. 18, 232 (1973); JETP Letters 18, 138 (1973).
2. Y. Carmel, J. Ivers, R. E. Kreibel, and J. Nation, Phys. Rev. Letters 33, 1278 (1974).
3. M. Friedman, Appl. Phys. Letters 26, 366 (1975).
4. M. Friedman and M. Herndon, Phys. Fluids 16, 1982 (1973).
5. V. L. Granatstein, M. Herndon, P. Sprangle, Y. Carmel, and J. Nation, Plasma Phys. 17, 23 (1975).
6. V. L. Granatstein, M. Herndon, R. K. Parker, and S. P. Schlesinger, IEEE Trans. on Microwave Theory and Techniques, Vol. MTT-22, No. 12, Pt. 1, pp. 1000-1005, December 1974.
7. A. N. Didenko, A. G. Gerlitsin, V. I. Zelentsov, G. P. Fomenko, Yu. G. Shtein, and Yu. G. Yushkov, in Proceedings of the International Topical Conference on Electron Beam Research and Technology, U.S. Department of Commerce UC-21, Vol. II, p. 424, 1976.
8. T. J. Orzechowski and G. Bekefi, Phys. Fluids 19, 43 (1976).
9. G. Bekefi, T. J. Orzechowski, and K. D. Bergeron, in Proceedings of the International Conference on Electron Beam Research and Technology, U.S. Department of Commerce UC-21, Vol. I, p. 303, 1976; also Bull. Am. Phys. Soc. 21, 571 (1976), Paper DM4.
10. G. B. Collins (Ed.), Microwave Magnetrons, Radiation Laboratory Series, Vol. 6 (McGraw-Hill Book Company, Inc., New York, 1948).
11. E. Okress (Ed.), Crossed-Field Microwave Devices (Academic Press, Inc., New York, 1961).
12. P. L. Kapitsa, High-Power Microwave Electronics (Pergamon Press, New York, 1964).
13. An excellent review of power levels, efficiencies, etc. of various crossed-beam devices is given by V. L. Granatstein, R. K. Parker, and P. Sprangle, in Proceedings of the International Topical Conference on Electron Beam Research and Technology, U.S. Department of Commerce UC-21, Vol. II, p. 401, 1976.
14. S. Silver (Ed.), Microwave Antenna Theory and Design, Radiation Laboratory Series, Vol. 12 (McGraw-Hill Book Company, Inc., New York, 1949).
15. L. Gould, Handbook on Breakdown of Air in Waveguide Systems, Microwave Associates, Burlington, Massachusetts, April 1956.
16. E. Ott and R. V. Lovelace, Appl. Phys. Letters 27, 378 (1975). Note that these calculations are for a planar magnetron and therefore are only approximately applicable to our cylindrical device.

X. PLASMA DYNAMICS

B. Plasma Research Related to Fusion

Research – Theoretical

1. RF HEATING BY ELECTRON LANDAU DAMPING OF LOWER HYBRID WAVES

U. S. Energy Research and Development Administration (Contract E(11-1)-3070)

Abraham Bers, Frank W. Chambers, Nathaniel J. Fisch

Introduction

In this report we consider in detail supplementary heating of a Tokamak plasma by electron Landau damping (ELD) of lower hybrid (LH) waves.[1] In this heating scheme the RF power is deposited on the electrons and then the ions are heated by collisions in an electron-ion energy exchange time. Electron heating is also important in providing a means for controlling the current profile in a Tokamak.

In our analysis we shall consider the spatial damping of lower hybrid modes as they propagate into the plasma. The coordinate system is illustrated in Fig. X-19. For

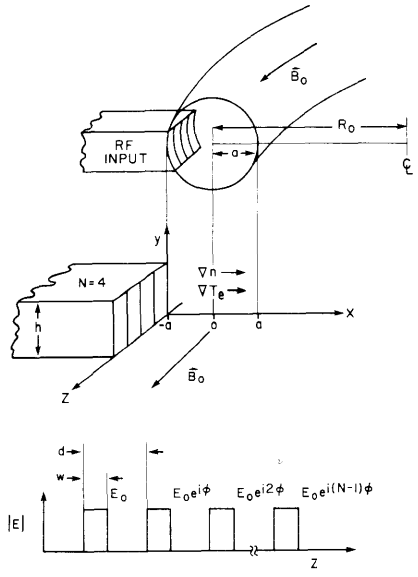

Fig. X-19.

Schematic representation of the three-dimensional Tokamak and of the two-dimensional slab model for studying the RF heating. The plasma is assumed uniform in the $\hat{y}$ and $\hat{z}$ directions and the excitation uniform in $\hat{y}$. The array is composed of N waveguides, width w, separation d, and, for power calculations, height h.

purposes of calculation we model the plasma as a slab, uniform in the $\hat{y}$ and $\hat{z}$ directions with a uniform magnetic field $\bar{B}_o$ in the $\hat{z}$ direction. The plasma density $n_e(x)$ and electron temperature $T_e(x)$ vary in the $\hat{x}$ direction; the wave launching structure, a waveguide array of finite extent,[1, 2] lies in the y-z plane. We Fourier-transform the

electric field in the $\hat{z}$ direction and consider the propagation and dissipation of the individual Fourier components in $n_z = ck_z/\omega$. The power flow and power dissipated per n_z component in the $\hat{x}$ direction are calculated in the WKB approximation. We then sum over all n_z components of the spectrum launched by the array to obtain the total power flow and power dissipated as a function of x. Thus we obtain the fraction of the total incident RF power dissipated in the plasma, which we define as the heating efficiency ϵ, and we determine the location in the plasma profile where this power is deposited. At the high powers required for significant supplementary RF heating, nonlinear effects on Landau damping are important. We must also consider the effect of the large perpendicular electric fields on perpendicular spatial diffusion and parallel velocity diffusion.

Linear Propagation and Electron Landau Damping of a Lower Hybrid Wave for Fixed n_z

The local linear spatial Landau damping in the $\hat{x}$ direction of a lower hybrid wave of wave number k with component k_z parallel to $\overline{B}_o$ is given approximately[1] by

$$k_{xi}(x) = \sqrt{\pi}\ k(x)\ \zeta^3(x)\ e^{-\zeta^2(x)} \tag{1}$$

where

$$\zeta(x) = \frac{\omega}{[\sqrt{2}\ k_z v_{Te}(x)]} = \frac{\frac{c}{v_{Te}(x)}}{\sqrt{2}\ n_z}.$$

The electron temperature T_e and the electron density n_e are both functions of x, and k(x) is the local wave number in a WKB approximation. We assume an excitation frequency ω, and a fixed wave number k_z in the direction parallel to $\overline{B}_o$, and profiles for the x-dependence of T_e and n_e. From these $k_{xi}(x)$ and subsequently the power flow and power dissipation in the $\hat{x}$ direction can be calculated. The temperature of $\zeta(x)$ is given in Eq. 1; the density dependence of k(x) is determined from the cold electrostatic dispersion relation for lower hybrid waves.

$$D(\omega, \vec{k}) = K_{\parallel} k_z^2 + K_{\perp} k_x^2 = 0 \tag{2}$$

where

$$K_{\parallel}(x) = 1 - \frac{\omega_{pe}^2(x)}{\omega^2} - \frac{\omega_{pi}^2(x)}{\omega^2} \tag{3}$$

and

$$K_{\perp}(x) \cong 1 + \frac{\omega_{pe}^2(x)}{\Omega_e^2} - \frac{\omega_{pi}^2(x)}{\omega^2} \tag{4}$$

for $\Omega_i \ll \omega \ll \Omega_e$.

Table X-2 gives a typical parameter set that is used for the calculations in this report. For this plasma the maximum ω_{LH} is 3.4×10^9. We consider an excitation at $\omega \sim 1.5\ \omega_{LH} = 5.0 \times 10^9$. In Fig. X-20 the plasma profiles, Re (k_x), and Im (k_x) are plotted against x for the parameters given in Table X-2. In Fig. X-20b we plot Re $[ck_x(x)/\omega n_z]$ because this ratio is independent of n_z in the electrostatic approximation. Since $\omega > \omega_{LH}^{max}$, there is no resonance (Re $(k_x) \to \infty$) and the enhancement $k_x/k_z|_{x=0} \sim 55 \sim \omega_{pe}(x=0)/\omega \sim (m_i/m_e)^{1/2}$. This enhancement is determined solely by the density profile, since the dispersion relation (Eq. 2) is independent of temperature. A typical perpendicular wavelength for $n_z = 6.0$ at $x = 0$ is $\lambda_x = .11$ cm. In Fig. X-20c, Im $(k_x(x)) = k_{xi}(x, n_z)$ is plotted for several n_z. Here the main x-dependence is introduced through the ζ-dependent term within the exponential. For a given n_z the x-dependence because of the electron temperature profile is the dominant effect. It can also be seen in Fig. X-20c that $k_{xi}(x, n_z)$ is quite sensitive to n_z. Waves with $n_z \leq 4.0$ are virtually undamped. With our parameters a normalized damping rate of $ck_{xi}/\omega = 1.0$ corresponds to an e-folding distance of ~6 cm. The damping is weakly density-dependent through the k(x) in Eq. 1.

The effect of finite electron and ion temperatures on the real part of the dispersion relation has been studied. The dispersion relation, including leading order temperature effects, is

$$-a^2 k_x^4 + K_{\parallel} k_z^2 + K_{\perp} k_x^2 = 0, \tag{5}$$

where

$$a^2 = 3\left[\left(\frac{\omega_{pi}}{\omega}\right)^2 \left(\frac{v_{Ti}}{\omega}\right)^2 + \frac{1}{4}\left(\frac{\omega_{pe}}{\Omega_e}\right)^2 \left(\frac{v_{Te}}{\Omega_e}\right)^2\right]$$

with

$$v_{Te,\,Ti} = \left[\frac{K_B T_{e,i}}{m_{e,i}}\right]^{1/2} \tag{6}$$

The k_x^4 term in Eq. 5 introduces a second mode for a given k_z. For some density this mode will merge with the cold electrostatic mode and a reflection or wave conversion will occur. Energy propagating in on a cold-plasma mode can turn around and propagate

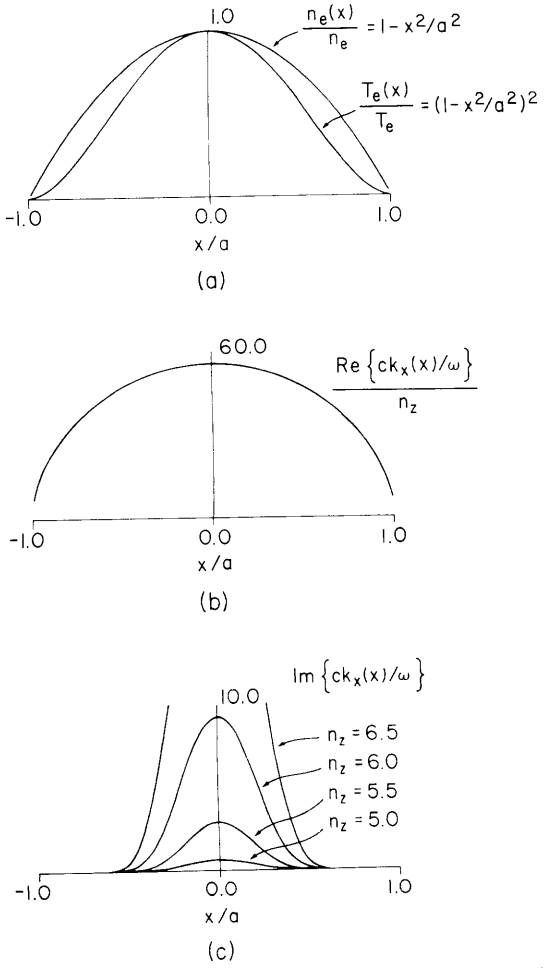

Fig. X-20.

Plasma profiles and variation of Re $(k_x(x))$ and Im $(k_x(x))$ vs x.

(a) Normalized temperature and density profiles.

(b) Re $\{ck_x(x)/\omega\}/n_z = k_x/k_z = n_x/n_z$. (Normalized to n_z.)

(c) Im $\{ck_x(x)/\omega\}$ for several values of n_z.

Table X-2. Current state-of-the-art Tokamak plasma example for computations.

Machine Parameters

$R_o = 100$ cm

$a = 20$ cm

$B = 20$ kG

Plasma Parameters and Profiles

D^+ Plasma

Density $n_e(x) = n_e(1-x^2/a^2)$

$n_e = 2 \times 10^{13}/\mathrm{cm}^3$

Temperature $T_e(x) = T_e(1-x^2/a^2)^2$

$T_e = 1000$ eV

$T_i = 200$ eV

back out on the warm-mode branch. The n_z for "turnaround" at a fixed density and temperature is determined from Eq. 5 by looking for a double root in k_x^2 to yield

$$n_z^2 = \frac{K_\perp^2}{4\left(\frac{\omega^2 a^2}{c^2}\right)(-K_\parallel)}. \tag{7}$$

The modes predicted by this dispersion relation for varying density for several n_z are illustrated in Fig. X-21. For this plot the electron temperature was fixed at 1000 eV, the ion temperature at 200 eV, and the density ranges from 0 through $1.12 \times 10^{14}/cm^3$, at which the lower hybrid resonance occurs for our chosen ω and B_o. The higher the

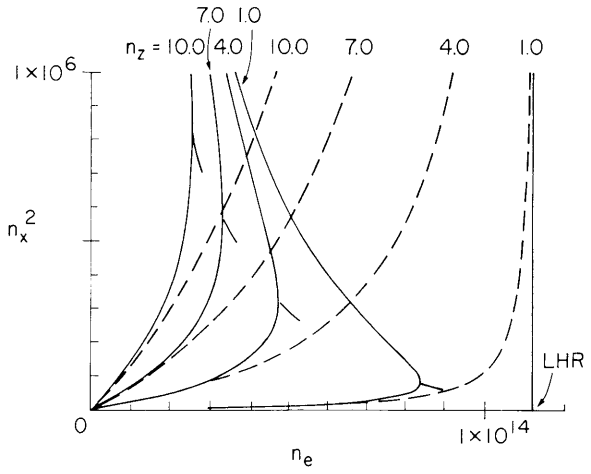

Fig. X-21. n_x^2 vs density for several n_z to illustrate the thermal effects introducing a second mode that merges with the lower hybrid mode at a turnaround density. Broken lines indicate the appearance of each mode in the absence of temperature effects. Lower hybrid resonance occurs at $n_e = 1.12 \times 10^{14}/cm^3$.

n_z, the more important the thermal effects will be. Since we consider a maximum density of $2 \times 10^{13}/cm^3$ and $n_z \lesssim 10.0$, thermal corrections are not important in our parameter range.

The power flow in the $\hat{x}$ direction per unit height in the $\hat{y}$ direction per unit Δk_z for a mode at some n_z, $S_x(x,n_z)$, is related to the power dissipated per unit distance Δx, $P_D(x, n_z)$, through $k_{xi}(x, n_z)$:

$$k_{xi}(x, n_z) = \frac{P_D(x, n_z)}{2S_x(x, n_z)}. \tag{8}$$

Since the power dissipated is just the negative spatial rate of change of the power flow,

$$P_D(x, n_z) = \frac{-dS_x(x, n_z)}{dx}. \tag{9}$$

We can integrate Eq. 9 to get an expression for the power flow for a given n_z mode,

$$S_x(x, n_z) = S_x(-a, n_z) \exp\left[-\int_{-a}^{x} 2k_{xi}(x, n_z)\, dx\right], \tag{10}$$

where $S_x(-a, n_z)$ is the incident power $x = -a$. Knowing $k_{xi}(x, n_z)$, for a given n_z we can determine the power flow, the total power dissipated, and the x location in the profile where the power is deposited. Figure X-22 gives calculations of the power flow and power dissipated either for varying n_z with $T_e = 1000$ eV held constant or for varying T_e with $n_z = 5.0$, as indicated in Table X-3, and calculations of the x locations for damping and reflection as a function of n_z. The dissipation is always greater on the left side ($x < 0$), since the power is assumed incident from the left at $x = -a$. Consider the n_z variation with T_e fixed at 1000 eV, then the more weakly damped modes, $n_z \sim 4.0$-5.0, deposit their energy near the center of the plasma where the damping is strongest because of the peaking of $T_e(x)$. As n_z is increased the modes damp out over smaller ranges in x and much nearer the left-hand edge. Ideally, we would like to have 100% of the mode energy deposited near the plasma center; however, these two requirements are satisfied at opposite ends of the n_z spectrum. Therefore we must seek a compromise design for the array to concentrate the wave energy near an n_z for which a sizable fraction of the power is deposited near the center of the plasma; for this example $n_z \cong 5.0$ appears best. Consider the temperature variation with n_z fixed at 5.0, then as the temperature increases the damping increases and the power is deposited nearer the plasma edge. To continue heating the core, it may also be necessary to launch low n_z modes that would be undamped initially but later would heat the core or, through the use of time-variant phased arrays, to vary the spectral composition of the launched spectrum as the plasma heats.

In Fig. X-22c we see for a given penetration x the n_z modes that will be turned around by the thermal effects (Eq. 7), and the n_z modes that are Landau damped. For Landau damping we require $v_{\phi z} = c/n_z \sim 5v_{Te}(x)$. The broken line indicates in x where a given n_z component will damp, the solid line indicates where it will reflect. Since the broken line, in our example, lies below the solid line, a mode propagating in from the edge will damp out before reaching the reflection region. Hence we are justified in using the cold-plasma dispersion relation.

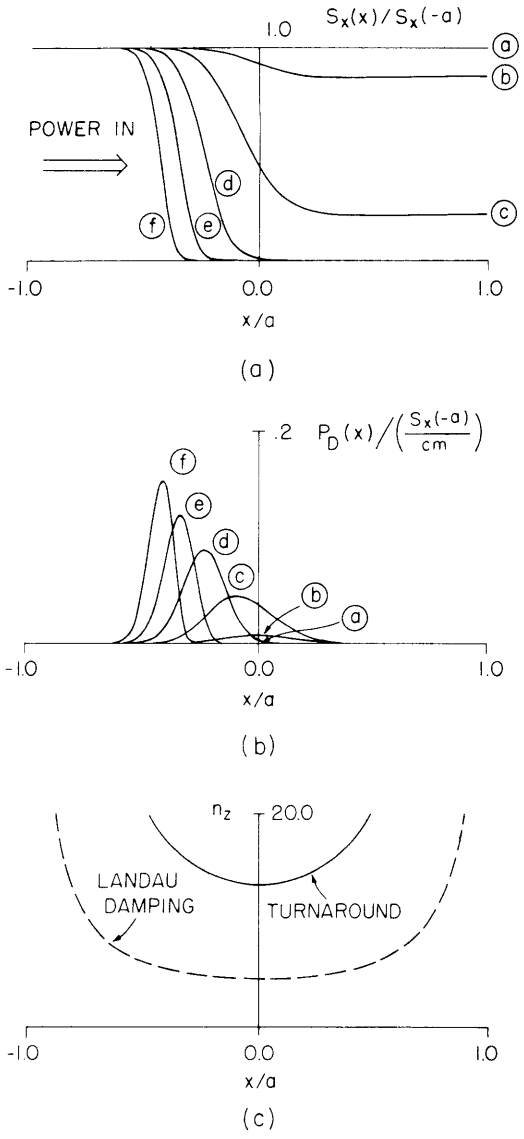

Fig. X-22.

(a) Power flux $S_x(x)$ vs x/a.

(b) Power dissipated $P_D(x)$ vs x/a. The curves show n_z varying with T_e fixed or T_e varying with n_z fixed. Heating efficiency ϵ and location of dissipated power are determined for each parameter set.

(c) Locations in x where a given n_z mode damps for T_e = 1000 eV (broken line) as calculated in (b) or turns around (solid line) as calculated in Fig. X-21.

Table X-3. Values for the calculations in Fig. X-22a, b.

Curve	T_e = 1000 eV	n_z = 5.0	Efficiency
	n_z =	T_e =	ϵ =
(a)	4.0	640 eV	.006
(b)	4.5	810	.144
(c)	5.0	1000	.794
(d)	5.5	1210	1.0
(e)	6.0	1440	1.0
(f)	6.5	1690	1.0

Power Flow and Power Dissipation vs x for a Spectrum of n_z

Any finite waveguide array will launch a spectrum of n_z components into the plasma. The exciting structure that we consider has N waveguide ports, each of width w, separated from the adjacent port by distance d. The waveguides are assumed to operate in the TE_{10} mode with the electric field in the $\hat{z}$ direction and with the relative phase, ϕ, between the waveguides fixed. The electric field spectrum Fourier-transformed in the $\hat{z}$ direction for such an array is given by

$$E_z(k_z) = E_o Nw \operatorname{sinc}\left(\frac{k_z w}{2}\right) \frac{\sin\left(\frac{Nd}{2} k_z - \frac{N\phi}{2}\right)}{N \sin\left(\frac{d}{2} k_z - \frac{\phi}{2}\right)} \left[\left(e^{-idk_z} e^{i\phi}\right)^{(N-1)/2}\right], \tag{11}$$

where E_o is the maximum electric field and is related to the total power in the waveguides (waveguide height h) by

$$P = N \frac{c\epsilon_o E_o^2 hw}{2} \frac{\left(1 - \frac{\pi^2}{k_o^2 h^2}\right)^{1/2}}{2} = 6.64 \times 10^{-4} \text{ Nw (cm) h (cm) } (E_o \text{ (V/cm)})^2 \frac{\lambda}{\lambda_g}, \tag{12}$$

where $k_o = \omega/c$. We can also view the power flow as being divided among the Fourier components. Thus

$$P = \int dz \int dy\, S_x(z, y) = \int \frac{dk_z}{2\pi} \underbrace{\int dy\, S_x(k_z, y)}_{S_x(k_z)} \tag{13}$$

where the equality of the integrals follows from Parseval's theorem, since $S_x(z, y)$ depends on $|E(z, y)|^2$. Hence, from Eqs. 12 and 13,

$$P = \int \frac{dk_z}{2\pi} \frac{c\epsilon_o h}{2} \frac{\left(1 - \frac{\pi^2}{k_o^2 h^2}\right)^{1/2}}{2} |E_z(k_z)|^2. \tag{14}$$

Here $E_z(k_z)$ is determined by Eq. 11, and thus we identify the power flux per unit spectral width as

$$S_x(k_z) = \frac{c\epsilon_o h}{2} \frac{\left(1 - \frac{\pi^2}{k_o^2 h^2}\right)^{1/2}}{2} |E_z(k_z)|^2. \qquad (15)$$

We can now relate this power flux in the waveguides to the input power flow $S_x(-a,n_z)$ at the boundary of the two-dimensional plasma model. We assume that $S_x(-a,n_z) = S_x(k_z)$ (Eq. 15) for all k_z that are above the accessibility condition. Thus we ignore any reflection in this part of the spectrum, and do not concern ourselves with the fate of the spectral energy below accessibility. It should be noted that a properly designed array will have most of the power flow above accessibility, since electron Landau damping occurs for $n_z \gg 1$.

For the plasma and Tokamak described in Table X-2 we want to concentrate the lower hybrid wave energy around $n_z = 5.5$. With $\omega = 5.0 \times 10^9$, $n_z = 5.5$ corresponds to a spatial wavelength $\lambda_z = 2\pi/k_z = 2\pi c/\omega n_z \cong 6.5$ cm. To produce a spectrum concentrating the energy at this wavelength, we set d = w = 3.0 cm with $\phi = 180°$. We consider an array of four waveguides, N = 4. Fewer waveguides lead to a broader spectrum exciting n_z components which will not heat efficiently. An upper limit on the number of waveguides is set by the available space at the wall port and concern for not having a spectrum that is too narrow.

The electron Landau-damping calculation for this array with the plasma and machine parameters listed in Table X-2 is presented in Fig. X-23. Figure X-23a gives the array spectrum $|E_z(k_z)|$ from Eq. 11. The spectrum is peaked at $n_z \sim 6.0$ to maximize the damping and there is little energy at low n_z where the spectrum is not accessible. In Fig. X-23b, through Eq. 15, the spectrum has been converted to a power flux and the inaccessible portions of the spectrum have been eliminated. The outermost trace then represents the power flux $S_x(k_z)$ at the edge of the plasma at x = -a. Then, using Eq. 10 for each n_z component, we follow this spectrum into the plasma. We give the spectrum in n_z for several x positions in the plasma. Between x/a = -1.0 and x/a = -0.6 only the very highest ($n_z \sim 8.0$-10.0) modes damp, because of the low electron temperature in this region. Between x/a = -0.6 and x/a = -0.2 the modes with $6 \lesssim n_z \lesssim 9$ damp out and deposit most of the energy. Between $-0.2 < x/a < +0.2$ the modes with $5 \lesssim n_z \lesssim 6$ deposit their energy. When x/a > +0.2 we are again in the decreasing temperature range and, since the modes that could damp at these lower T_e did so on the way into the plasma, the spectrum changes very little at x/a = .2, .6, 1.0. Integrating the power flow over k_z, and similarly integrating the power dissipated, we determine their x-dependency which is plotted in Fig. X-23c. Again the power propagates from left to right. The power flow is normalized to the total incident power, $S_x(0) = .80$; 3.4% of the incident power is in the inaccessible region of the spectrum, and the remaining 17% of the power

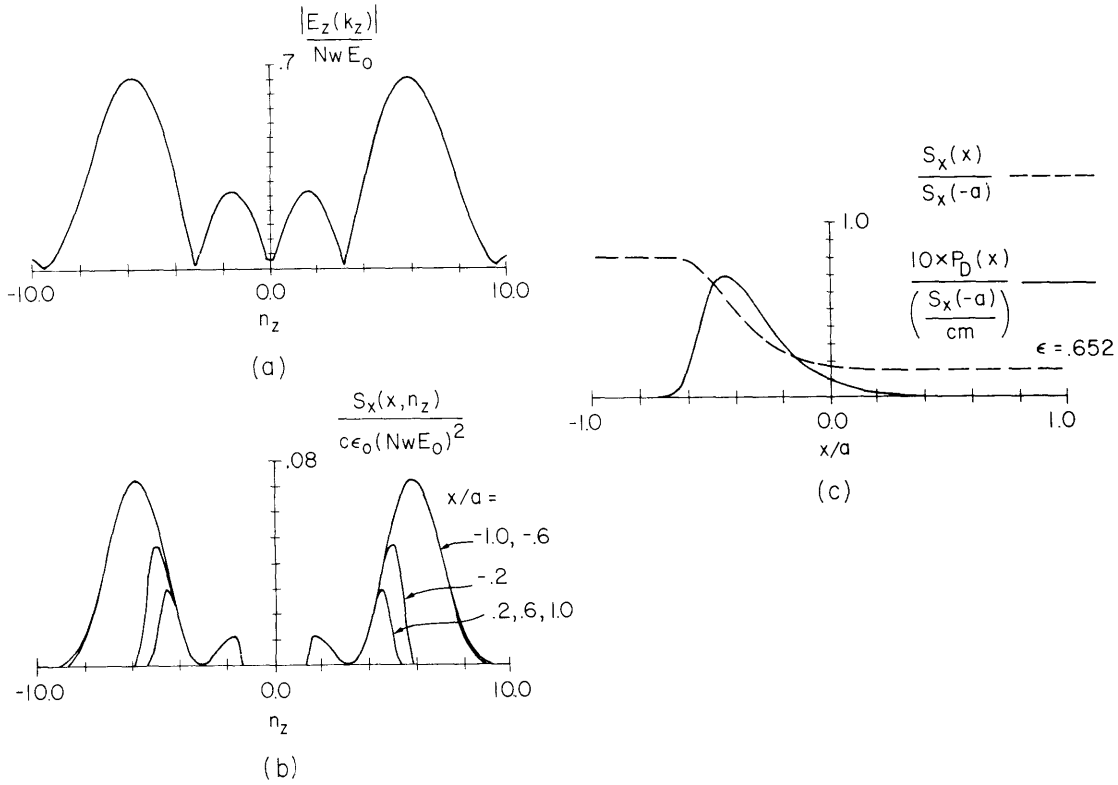

Fig. X-23. Full calculation of power dissipated, $P_D(x)$, and efficiency of heating, ϵ, for plasma, machine, and excitation parameters from Table X-2.
(a) Initial spectrum in $E_z(k_z)$ vs n_z excited by the launching array.
(b) Spectral power flux $S_x(n_z, x)$ vs n_z at various positions in the plasma.
(c) Power flux $S_x(x)$ and power dissipated $P_D(x)$ vs x/a.

lies at $|n_z| > 10.0$ and will be deposited near the plasma edge. On the right-hand side, 15% of the power emerges, so 65% of the power is absorbed, $\epsilon = .65$. The solid line in Fig. X-23c shows where in the profile the power is dissipated. Most of the power is deposited between x/a = -.6 and x/a = 0.2. The sharp rising edge occurs when the high n_z modes damp in the region of the sharp temperature rise. The trailing edge passing through the center of the plasma at x = 0 is due to the lower n_z modes. Thus for these parameters in the linear approximation electron Landau damping is an effective heating mechanism for depositing a sizable fraction of the RF energy into a reasonably large cross section of the plasma.

Figure X-24 illustrates the variation of the power dissipated with varying maximum electron temperature and waveguide array phasing. Figure X-24a shows power dissipated vs x for the data set of Table X-2 and the array previously described with the

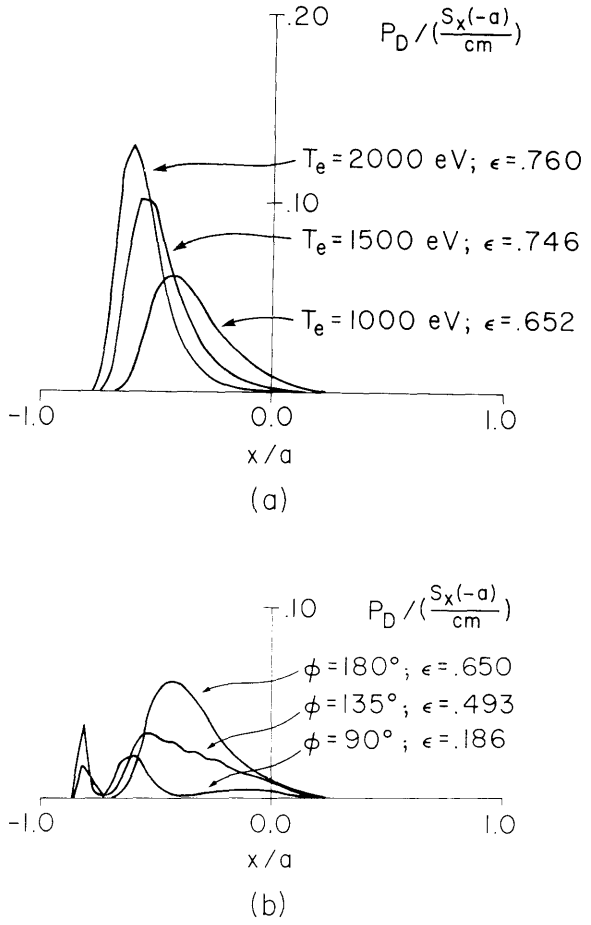

Fig. X-24. Power dissipated and heating efficiency.
(a) With plasma temperature varied.
(b) With relative phasings, ϕ, of the waveguides varied.

maximum electron temperature varied from 1000 eV to 2000 eV. With increased temperature the heating efficiency ϵ increases because the lower n_z modes will damp but the power becomes dissipated nearer the plasma edge and in a more peaked spatial pattern. In Fig. X-24b the relative phase between adjacent waveguides is changed to ϕ = 135° and 90° and the two lobes of $E_z(k_z)$ (Fig. X-23a) are shifted to differing values of n_z. One lobe is shifted to higher n_z and hence damps more strongly and farther out toward the plasma edge, while the other lobe is shifted to lower n_z and tends to be transmitted rather than absorbed. The symmetric pattern in n_z produced with ϕ = 180° is optimal for heating in our chosen example. Phase shifting does allow us to move one lobe to the optimal n_z for damping during the discharge to maintain optimal heating as the plasma parameters change with time. This may be useful for current profile control, as well as for heating.

Thus far we have considered only x-direction propagation and damping of a superposition of various n_z components. We have not considered the localization of the wave electric fields in resonance cones or the three-dimensional effects of the curved Tokamak. By taking advantage of known solutions for the ray trajectories for undamped lower hybrid waves in slab geometries[3] and toroidal geometries,[4] we can determine where the energy is deposited in both $\hat{x}$ and $\hat{z}$ directions. In Fig. X-25 we give the ray trajectories for lower hybrid waves in a slab and a torus. The power is deposited in the resonance cone regions contained by the rays in the $\hat{z}$ direction at the penetration depths

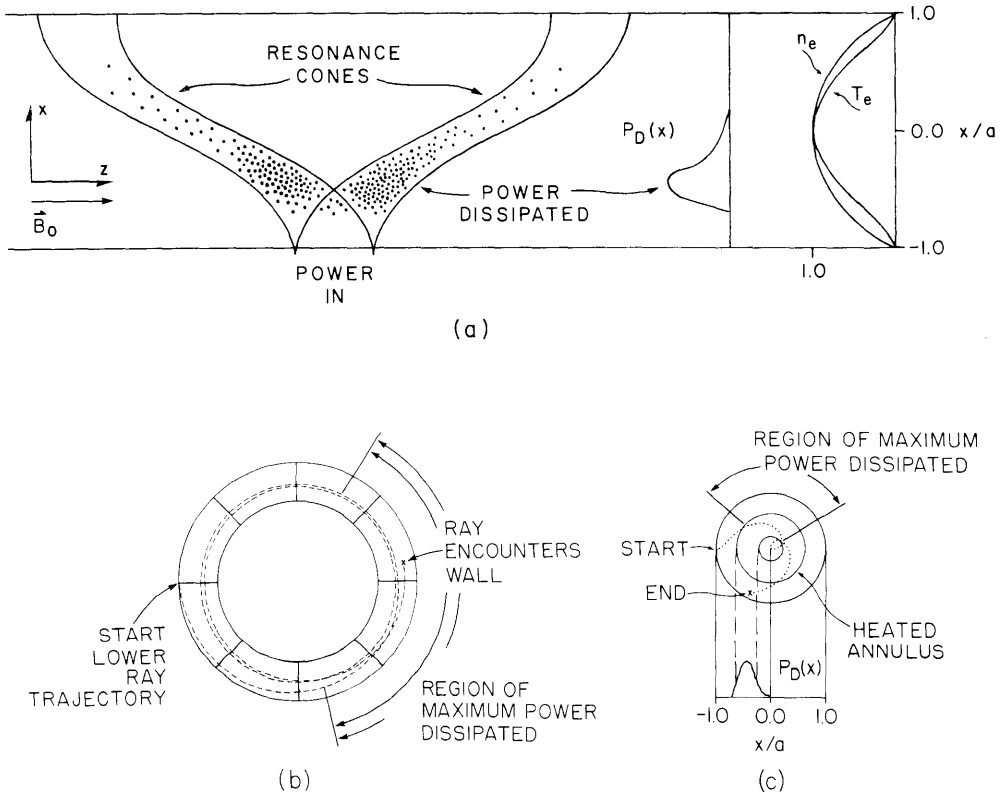

Fig. X-25. Energy deposition in two and three dimensions. In two dimensions (a), the power is deposited in x as determined by the calculations and in $\hat{z}$ within the two resonance cones. In three dimensions (b) and (c), the ray trajectory becomes more complex (one cone is shown) and power is deposited around the Tokamak.

in x which have been calculated. Viewing the three-dimensional ray plots (Fig. X-25b,c), we can see that the calculated energy deposition occurs on an extended region in the major (Fig. X-25b) and minor (Fig. X-25c) cross sections. The circulating electrons traversing these regions will lead to an effectively uniform heating of a toroidal annulus, as indicated in Fig. X-25c.

Nonlinear Effects in Electron Landau Damping

In calculating the steady-state linear damping rate of the field we must take into account the balance between the quasi-linear tendency of the resonant particle distribution to form a velocity plateau as it absorbs wave energy and the effect of Coulomb collisions that tend to destroy the plateau and restore the plasma to a Maxwellian distribution. Furthermore, in the presence of large fields the particles execute highly nonlinear bouncing in the wave troughs which renders invalid assumptions made in the linear theory. Both nonlinear effects lead to a damping rate less than that of zero-amplitude waves, as we shall show in Eq. 30. To find the modified growth rate accounting for large fields and collisional plateau destruction, we must examine the diffusion coefficient. We employ here a phenomenological approach that will enable us to find the correct scaling of the modifications in the presence of finite fields and will give numerical agreement in various well-known limits.

The diffusion coefficient may be written phenomenologically (for example, in a Fokker-Planck description) as

$$D = (\Delta v_z)^2/2\Delta t, \tag{16}$$

where Δv is the typical velocity step size arising from a collision between the particle and the field, and Δt is the length of time between collisions. We consider two limiting cases for D depending upon the ratio τ_{ac}/τ_{tr}, where $\tau_{ac} \equiv 2\pi[\Delta k_z | v_{gz}-v_z|]^{-1}$ is the correlation time of the field in the frame of a resonant particle, and $\tau_{tr} \equiv 2\pi\sqrt{m/qk_z E_{rms}}$ is the bounce or trapping time of a particle in a typical wave trough. In the limit $\tau_{ac}/\tau_{tr} \ll 1$ (where quasi-linear theory is valid), we write $\Delta v = (qE_{rms}/m)\tau_{ac}$, since the particle undergoes free acceleration for a time τ_{ac}. The length of time between collisions (or the periods of free acceleration) is $\Delta t = \tau_{ac}/\alpha$, where α is the ratio of the volume of the plasma occupied by the electric field to the total plasma volume. Thus, in the limit $\tau_{ac}/\tau_{tr} \ll 1$, from Eq. 16 we have

$$D = \alpha\left(\frac{q}{m}\right)^2 \frac{E_{rms}^2}{\Delta k_z} \frac{\pi}{|v_{gz}-v_z|}. \tag{17}$$

We may express D in more conventional form in terms of the spectral energy density $\mathscr{E}_k$. By definition,

$$\frac{\epsilon_o}{2} E_{rms}^2 \equiv \int_{-\infty}^{\infty} \mathscr{E}_{kz}\, dk_z \approx 2\mathscr{E}_{kz}\Delta k_z \tag{18}$$

so that Eq. 17 becomes

$$D = \alpha D_o, \tag{19}$$

where D_o is the usual one-dimensional quasi-linear diffusion coefficient

$$D_o = \frac{4\pi}{\epsilon_o}\left(\frac{q}{m}\right)^2 \frac{\mathscr{E}_{kz}}{|v_{gz}-v_z|}. \tag{20}$$

The factor α in Eq. 19 occurs because diffusion only takes place in a region of limited spatial extent in the plasma (within the resonance cones).

In the opposite limit, $\tau_{ac}/\tau_{tr} \gg 1$, particles do not undergo free acceleration while in the resonance cones. Instead, they bounce in the wave troughs and acquire a typical velocity change $\Delta v_z = 2\pi/k_z\tau_{tr} = \sqrt{qE_{rms}/mk_z} \equiv v_{tr}$. The time between collisions, $\Delta t = \tau_{ac}/\alpha$, remains the same. Thus, by using Eq. 16 in the limit $\tau_{ac}/\tau_{tr} \gg 1$, the diffusion coefficient is written as

$$D = \alpha\left(\frac{q}{m}\right)^2 \frac{E_{rms}}{\Delta k_z} \frac{\pi}{|v_{gz}-v_z|} \frac{\tau_{tr}^2}{\tau_{ac}^2} \frac{1}{(2\pi)^2} = \frac{\alpha D_o}{(2\pi\tau_{ac}/\tau_{tr})^2}. \tag{21}$$

We may combine the results (21) and (19) to write

$$D = \frac{\alpha D_o}{\max\left[1, (2\pi\tau_{ac}/\tau_{tr})^2\right]} \equiv \alpha D_o/M_1, \tag{22}$$

which agrees with the previous results in the limits $\tau_{ac}/\tau_{tr} \gg 1$ or $\tau_{ac}/\tau_{tr} \ll 1$. When using Eq. 22, care must be taken to determine the particles that are, in fact, subject to diffusion. In the limit $\tau_{ac}/\tau_{tr} \ll 1$, the velocity width of the resonant particles is only $\Delta(\omega/k_z) = \Delta k_z |v_{gz}-v_z|/k_z$, whereas in the limit $\tau_{ac}/\tau_{tr} \gg 1$ the velocity width is $2v_{tr}$. This is related to the resonance broadening effect.[5]

In order to calculate the damping rate of the spectrum, we use the equation of conservation of energy,

$$\frac{d}{dt}\int dV \left[\int \mathscr{E}_{kz}\, dk_z + \int d^3v \frac{1}{2} mnv_z^2 f_o(v)\right] = 0 \tag{23}$$

where for the first term $d/dt \equiv \partial/\partial t + \bar{v}_g \cdot \nabla$. For the problem of steady-state spatial damping in the x direction across the magnetic field, $d/dt \rightarrow v_{gx}k_{xi}$. In dealing with the second term in Eq. 23 we note that $(d/dt)\, f_o = (\partial/\partial v_z)\, D(\partial/\partial v_z)\, f_o$. Since f_o is subject only to parallel diffusion, we may integrate Eq. 23 by parts over parallel velocities to obtain

$$\int dV \int dk_z\, 2v_{gx}k_{xi}\mathscr{E}_{kz} = \frac{1}{2}\int dV \int dv_z\, mnv_z D(v_z) \int dv_\perp \frac{\partial}{\partial v_z} f_o(v). \tag{24}$$

The factor 1/2 arises because the change in the resonant-particle kinetic energy is twice the change in the field energy. In the presence of collisions, the steady state $\partial f_o/\partial v_z$ will differ from $\partial f_m/\partial v_z$, a Maxwellian distribution,[6,7] by

$$\frac{\partial f_o}{\partial v_z} = \frac{\partial f_m}{\partial v_z} \frac{1}{1 + D(v_z)/D_c}, \tag{25}$$

where D_c is the diffusion attributable to collisional scattering which, in general, is a function of $v_\perp$. Note that in the limit $D_c \to 0$, a velocity plateau is formed in the steady state that, from Eq. 24, implies $v_{gx}k_{xi} \to 0$. If we approximate

$$\int dk_z \approx 2\Delta k_z \tag{26}$$

and

$$\int dv_z \approx \max(\Delta v_z, 2v_{tr}) = \frac{\Delta k}{k} |v_{gz}-v_z| \max\left[1, 2\frac{\tau_{ac}}{\tau_{tr}}\right]$$

$$\equiv \frac{\Delta k}{k} |v_{gz}-v_z| M_2, \tag{27}$$

then we may write Eq. 24 as

$$2v_{gx}k_{xi}\mathscr{E}_{k_z}(2\Delta k_z)\, a \approx \frac{1}{2} mnD(v_z) \frac{\partial f_o(v_z)}{\partial v_z} \frac{\Delta k_z}{k_z} |v_{gz}-v_z|\, M_2 H\left(\frac{D}{D_c}\right), \tag{28}$$

where

$$H\left(\frac{D}{D_c}\right) = \int_0^\infty \frac{e^{-v^2/2v_{Te}^2}}{1 + \frac{D}{D_c}}. \tag{29}$$

The various coefficients $D(v_z = \omega/k_z)$, k_z, v_{gz}, etc. are taken to be typical coefficients within the resonant region. Using Eqs. 22 in Eq. 28, we write

$$v_{gx}k_{xi} = (v_{gx}k_{xi})_o (M_2/M_1)\, H(aD_o/M_1 D_c) \tag{30}$$

where $(v_{gx}k_{xi})_o$ is the usual linear damping rate based on the unperturbed Maxwellian distribution. That is,

$$(v_{gx}k_{xi})_o = \frac{\pi}{2}\frac{\omega_p^2}{|k|}\left.\frac{\partial f_m}{\partial v_z}\right|_{v_z=\omega/k_z}. \tag{31}$$

For $v_z > v_{Te}$, H can be approximated[7] as

$$H(y) = 1 + y\exp(1/2+y)\,\mathrm{Ei}(-1/2-y) \tag{32}$$

where

$$y = \frac{\alpha D_o v_z^3 \tau_c}{4M_1 v_{Te}^5} \tag{33}$$

$$\tau_c = \frac{8\pi n_e v_{Te}^3}{\omega_{pe}^4 \log\Lambda} \tag{34}$$

$$\mathrm{Ei}(-x) = -\int_x^\infty dt\,\frac{e^{-t}}{t}. \tag{35}$$

In the limit $(\tau_{ac}/\tau_{tr}) \ll 1$, we find

$$\frac{k_{xi}}{(k_{xi})_o} \approx H(y) \approx \begin{cases} 1, & y \ll 1 \\ 3D_c/2\alpha D_o, & y \gg 1 \end{cases} \tag{36}$$

and k_{xi} can be calculated for each mode of the k_z spectrum. On the other hand, for $(\tau_{ac}/\tau_{tr}) \gg 1$,

$$\frac{k_{xi}}{(k_{xi})_o} \approx \frac{H(y)}{2\pi^2\tau_{ac}/\tau_{tr}} \approx \begin{cases} \tau_{tr}/2\pi^2\tau_{ac}, & y \ll 1 \\ 3\tau_{ac}D_c/\alpha\tau_{tr}D_o, & y \gg 1 \end{cases} \tag{37}$$

and since the whole k_z spectrum behaves essentially as one wave, it is only meaningful to calculate an average (over v_{tr} in the corresponding velocity space) damping rate $\langle k_{xi}\rangle$ for the whole spectrum.

In order to use Eq. 30 in calculating the nonlinear effect of trapping and plateau formation, we must first find the electric fields within the plasma. The power flux for a given n_z mode at x, $S_x(x, n_z)$, is determined by Eq. 15. This power flux can be related to the electric field magnitude through the plasma impedance for the lower hybrid mode[2]

$$S_x(x, n_z) = -\frac{1}{4}\epsilon_o |E(n_z, x)|^2 \omega \frac{2K_\perp k_x}{k^2}. \tag{38}$$

To estimate the actual electric field magnitude from the known amplitudes of the spectral components, we must postulate a spatial profile in z for the field. Consider the field excited by the waveguide array with 180° phase shift between adjacent waveguides. If we assume that the field magnitude is constant in z at some level E(x) and that the z extent of the field is approximately 2(Nw), then we can write Parseval's theorem:

$$\int_{-\infty}^{\infty} \frac{dk_z}{2\pi} |\vec{E}(n_z, x)|^2 = \int_{-\infty}^{\infty} dz \, |\vec{E}(z, x)|^2 \approx 2(Nw) |E(x)|^2. \tag{39}$$

Combining Eqs. 38 and 39 yields an expression for the electric field within the resonance cone

$$|E(x)|^2 = \frac{1}{2Nw} \int_{-\infty}^{\infty} \frac{S_x(x, n_z)}{\left\{-\frac{1}{4}\epsilon_o \omega \frac{2K_\perp k_x}{k^2}\right\}} \frac{dk_z}{2\pi}. \tag{40}$$

Since for the cold electrostatic lower hybrid modes the $\vec{k}$ for all modes are collinear, we can express the parallel electric field as

$$E_z(x) = \left(\frac{+K_\perp}{-K_{||}}\right)^{1/2} E_x(x) \approx \left(\frac{K_\perp}{-K_{||}}\right)^{1/2} E(x). \tag{41}$$

The electric fields E(x) and $E_z(x)$ are plotted in Fig. X-26 for the data set of Table X-2. The electric fields have been normalized to E_o, the electric field in the waveguide related to the power through Eq. 12. The total field (solid line) grows as the lower hybrid modes propagate into the plasma; this is the WKB enhancement.

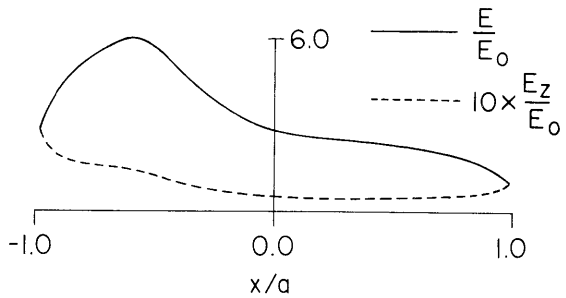

Fig. X-26. Total electric field, E, and electric field parallel to the magnetic field, E_z, vs x for the parameters of Fig. X-23 from Table X-2.

If there were no damping the enhancement at x = 0 would be ~10. In Fig. X-26 the parallel field $E_z(x)$ decreases as x increases even where E(x) is increasing because the waves turn their $\vec{k}$ toward the perpendicular direction as they propagate inward, and hence the parallel component of $\bar{E}$ decreases even while the magnitude of $\bar{E}$ increases. After x = -.6 the field amplitudes decrease because of the damping of the modes. (We have neglected the change in spectrum width caused by damping that would affect Eqs. 39 and 40.) As an example, with 50 kW per waveguide E_o = 1400 V/cm and typical values for E_z are ~200-300 V/cm in the regions in x where the damping occurs. For these numbers $\tau_{ac}/\tau_{tr} \approx 1/4$, whereas $\alpha D_o/D_c \approx 10^3$. Thus the major nonlinear effect is due to the velocity plateauing of the distribution, and the steady-state damping rate can be estimated from Eq. 36 to be <1% of the linear (no plateauing) damping rate. In Fig. X-27 we plot the power dissipated with 150-kW incident power for both the array of Fig. X-23 and Table X-2 and a more narrow array with d = w = 1.75 cm. For the usual array (Fig. X-27a) the plateauing has nearly eliminated the dissipation; only 7% of the energy is deposited in the plasma. With the redesigned array (Fig. X-27b) the

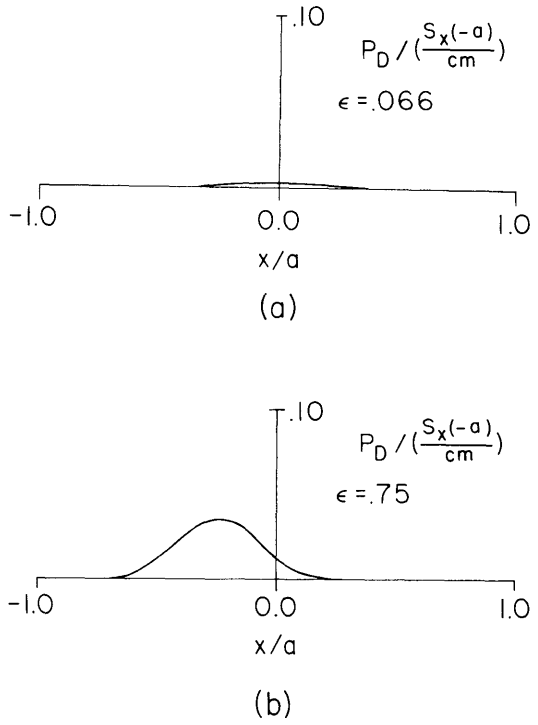

Fig. X-27. Power dissipated vs x including the effects of quasi-linear plateauing with 150 kW of incident power.
(a) Plasma and array used for the linear calculation in Fig. X-23 where the spectrum peaked at $n_z \sim 6.0$.
(b) New array with d = w = 1.75 cm so that the spectrum peaks near $n_z = 10.0$.

higher n_z modes damp and deposit ~75% of their energy. The modes with the higher n_z have lower phase velocities, and hence the Landau damping is stronger and the collisional diffusion is larger. Once the modes begin to damp, the electric fields in the plasma are reduced and the nonlinear diminution of the damping is lessened which leads to increased absorption.

Diffusion Caused by RF Fields

In the preceding analysis we have neglected the influence of the large perpendicular electric field. In the limit $\tau_{ac}/\tau_{tr} \ll 1$, the perpendicular field could, perhaps, lead to spatial diffusion across the magnetic field, but it is hardly expected to affect the rate of parallel diffusion in velocity space. The reason for this is that the parallel and perpendicular motions are uncoupled in this limit, and hence only very strong spatial diffusion or deflection of the particles out of the resonant region could affect the parallel diffusion. The situation, however, is not as clear intuitively in the regime of more interest in our problem, i.e., when $\tau_{ac}/\tau_{tr} > 1$. The motions perpendicular and parallel to the field are now strongly coupled and an approach starting from first principles is necessary in recomputing the parallel velocity diffusion coefficient.

Consider the idealized problem of motion of a trapped (resonant) particle in an electrostatic potential in rectangular coordinates of the form

$$\phi = -\phi_o \cos k_y y \cos (k_x x + k_z z - \omega t). \tag{42}$$

Such a potential may be unavoidable in our problem, since standing waves are naturally set up in the poloidal direction. Also, it leads to very interesting trapped-particle motion. We assume that the magnetic field is large ($k_\perp a_e \ll 1$) so the the guiding-center equations of motion are valid

$$\dot{\mathbf{r}} = \hat{z} \times \nabla\phi / B \tag{43}$$

$$\ddot{z} = (q/m)\, \nabla_z \phi \tag{44}$$

In order to analyze (43) and (44) we transform to the reference frame of the resonant particles $\tilde{z} = z - (\omega/k_z)t$. We now consider only well-trapped particles, i.e.,

$$k_x x + k_z \tilde{z} \ll 1 \tag{45}$$

$$k_y y \ll 1. \tag{46}$$

Under these assumptions, it follows that

$$\ddot{\tilde{z}} + \omega_B^2 \tilde{z} = -\omega_B^2 \frac{k_x}{k_z} x \tag{47}$$

$$\ddot{x} + \omega_D^2 x = -\omega_D^2 \frac{k_z}{k_x} \tilde{z}, \tag{48}$$

where

$$\omega_B^2 \equiv \frac{q}{m} k_z^2 \phi_o \tag{49}$$

$$\omega_D^2 \equiv k_x^2 k_y^2 \phi_o^2 / B_o^2. \tag{50}$$

Equations 47 and 48 represent the coupling between harmonic oscillation in the parallel wave troughs and circular motion in the perpendicular plane. The solution may be expressed in terms of the four initial conditions x_o, $\tilde{z}_o$, $v_{\tilde{z}o}$, and v_{xo}, e.g.,

$$v_{\tilde{z}} = -\tilde{z}_o \frac{\omega_B^2}{\omega_s} \sin \omega_s t - x_o \frac{\omega_B^2 k_x}{\omega_s k_z} \sin \omega_s t + v_{xo} \frac{k_x \omega_B^2}{k_z \omega_s^2} (\cos \omega_s t - 1)$$

$$+ v_{\tilde{z}o} \left(\frac{\omega_B^2}{\omega_s^2} \cos \omega_s t + \frac{\omega_D^2}{\omega_s^2} \right) \tag{51}$$

$$x = \tilde{z}_o \frac{k_z}{k_x} \frac{\omega_D^2}{\omega_s^2} (\cos \omega_s t - 1) + x_o \left(\frac{\omega_D^2}{\omega_s^2} \cos \omega_s t + \frac{\omega_B^2}{\omega_s^2} \right)$$

$$+ v_{xo} \left(\frac{\omega_D^2}{\omega_s^2} \frac{\sin \omega_s t}{\omega_s} + \frac{\omega_B^2}{\omega_s^2} t \right) + v_{zo} \frac{k_z \omega_D^2}{k_x \omega_s^2} \left(\frac{\sin \omega_s t}{\omega_s} - t \right), \tag{52}$$

where $\omega_s^2 \equiv \omega_D^2 + \omega_B^2$. The solution in the x-z plane appears as a bouncing at frequency ω_s

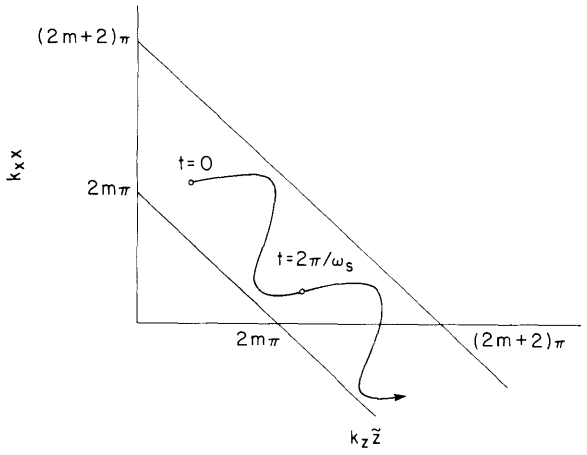

Fig. X-28.
Guiding-center motion in the x-z plane.

between lines of constant phase superposed on a drift between the lines (see Fig. X-28).

The implication of this picture is a change of the typical step sizes in the calculation of diffusion coefficients. As we can see from Eqs. 51 and 52, typical step sizes are

$$\Delta v_z = \begin{cases} qE_z\tau_{ac}/m, & \tau_{ac}\omega_s < 2\pi \\ v_{tr}\omega_B/\omega_s, & \tau_{ac}\omega_s > 2\pi \end{cases} \tag{53}$$

$$\Delta x = \begin{cases} \omega_D\tau_{ac}/k_x, & \tau_{ac}\omega_s < 2\pi \\ \omega_D^2/\omega_s^2 k_x, & \tau_{ac}\omega_s > 2\pi \text{ and } \tau_{ac}/\tau_{tr} < 1 \\ \omega_D\omega_B^2\tau_{ac}/\omega_s^2 k_x, & \tau_{ac}\omega_s > 2\pi \text{ and } \tau_{ac}/\tau_{tr} > 1 \end{cases} \tag{54}$$

Note that the definition of $\tau_{ac} \equiv 2\pi/\Delta k_z \left| V_{gz} - v_z \right|$ remains unchanged because $\Delta k_\perp$ never enters into the problem. Equations 53 and 54 may be used to estimate the relative importance of spatial-to-velocity diffusion. For example, in the regime $\tau_{ac}/\tau_{tr} > 1$ the relative importance is indicated by the ratio

$$\frac{\left(\tau_D^{-1}\right)_x}{\left(\tau_D^{-1}\right)_{v_z}} = \frac{D_{xx}/\delta x^2}{D_{vz}/\delta v_z^2} = \left(\frac{k_z}{k_x}\frac{\omega_D}{\omega_s}\frac{a_e}{r}\right)^2 \ll 1 \tag{55}$$

where $\delta v_z/\delta x$ are the typical scale lengths v_{Te} and r (the minor radius). Equation 55 indicates that the time scale for spatial diffusion is much longer than that for velocity diffusion.

Spatial diffusion per se may be unimportant, but the perpendicular fields might play a large role in reducing the parallel diffusion and hence the damping rate. For example, if $\omega_D \gg \omega_B$, then by using Eq. 53 in Eqs. 16 and 28, it can be seen that the diffusion coefficient will be reduced by a factor $(\omega_B/\omega_D)^2$ and possibly k_{xi} will be reduced. Also, note that the criterion for quasi-linear theory to be valid becomes $\tau_{ac}\omega_D \ll 2\pi$, rather than $\tau_{ac}\omega_B \ll 2\pi$.

In conclusion, let us note that there may be important nonlinear effects that we have not yet considered. One of these effects of particular interest is the trapped-particle or sideband instability. We expect that this instability will modify the distribution of spectral energy so as to ensure $\tau_{ac}/\tau_{tr} \approx 1$ and we are looking into this possibility.

References

1. A. Bers, "Ion Heating in Tokamaks by Wave Penetration and Parametric Downconversion of RF Power," in R. C. Cross (Ed.), Proceedings of the U.S.-Australian Workshop on Plasma Waves, University of Sydney, Sydney, Australia, February 13-18, 1975, Sec. 5.1.
2. A. Bers and C. F. F. Karney, Quarterly Progress Report No. 114, Research Laboratory of Electronics, M.I.T., July 15, 1974, pp. 123-131.
3. R. J. Briggs and R. R. Parker, "Transport of rf Energy to the Lower Hybrid Resonance in an Inhomogeneous Plasma," Phys. Rev. Letters 29, 852-855 (1972).
4. J. L. Kulp, G. L. Johnston, and A. Bers, RLE Progress Report No. 117, Research Laboratory of Electronics, M.I.T., January 1976, pp. 223-241.
5. N. J. Fisch and A. Bers, Phys. Rev. Letters 35, 373 (1975).
6. A. A. Vedenov, "Theory of a Weakly Turbulent Plasma," in Reviews of Plasma Physics, Vol. 3 (Consultants Bureau, New York, 1967).
7. J. Rowlands, V. L. Sizonenko, and K. N. Stepanov, Sov. Phys. – JETP 23, 661 (1966).

2. STOCHASTIC ION HEATING BY A PERPENDICULARLY PROPAGATING ELECTROSTATIC WAVE

U.S. Energy Research and Development Administration (Contract E(11-1)-3070)

Charles F. F. Karney, Abraham Bers

Introduction

In RLE Progress Report No. 117 (pp. 193-197) we considered the nonlinear motion of an ion in a perpendicularly propagating electrostatic wave. We found the condition under which the ion becomes momentarily trapped by the wave and so exchanges significant energy with the wave. In this report we examine the subsequent behavior of the ions and the conditions under which the ions are stochastically heated.

Hamiltonian Formulation

To study the long-term behavior of an ion, it is convenient to work with its Hamiltonian. The applied electric field is $\hat{y}E\cos(ky-\omega t-\phi)$. The equations of motion (discussed in our previous report) are

$$\ddot{y} + y = a\cos(y-\nu t-\phi); \quad \dot{x} = y \tag{1}$$

where lengths are normalized to $1/k$ and times to $1/\Omega$, $a = qkE/\Omega^2 m$, and $\nu = \omega/\Omega$.

By evaluating the Hamiltonian equations, it can be verified that the Hamiltonian is $1/2\left(p_y^2+y^2\right) - a\sin(y-\nu t-\phi)$. In order to work with a conservative system, we recast the Hamiltonian into

$$H = J_1 + \nu J_2 - \alpha \sin (\sqrt{2J_1} \sin w_1 - w_2), \tag{2}$$

where J_1, w_1, and J_2, w_2 are conjugate action angle variables, and $p_y = \sqrt{2J_1} \cos w_1$, $y = \sqrt{2J_1} \sin w_1$. The Hamiltonian equation $\dot{w}_2 = \partial H/\partial J_2$ may be integrated directly to give $w_2 = \nu t + \phi$. Thus w_2 is the wave phase and J_2 its conjugate action. Equation 2 may be viewed as describing two harmonic oscillators (the ion with frequency 1 described by J_1, w_1 and the wave with frequency ν described by J_2, w_2) coupled by the last term of the equation.

Phase Plane Trajectories

We begin our study of an ion with the Hamiltonian given by Eq. 2 by solving numerically for its trajectory in phase space. To picture the trajectory most easily, we plot only the cross section defined by $w_1 = \pi$ (the ion traveling in the -y direction). We plot $r(=\sqrt{2J_1})$ against w_2 for each crossing of the $w_1 = \pi$ plane where r is the normalized velocity of the ion. Figure X-29 shows such plots for $\nu = 30.11$ and 30.23, and $\alpha = 1$, 2, and 3. The trajectories of 15 particles are followed in each case. In these plots the condition that the ions travel at the wave phase velocity is given by $r = \nu$. If $r < \nu - \sqrt{\alpha}$, we expect negligible interaction with the wave. With $\alpha = 1$ the trajectories all lie on smooth curves. The existence of such continuous curves indicates that with small but finite α there is a new conserved quantity. (With $\alpha = 0$ the trajectories would all lie on horizontal straight lines, since J_1 is then a conserved quantity.) At $\alpha = 2$ we see the formation of "islands." The islands are first order for $\nu = 30.11$ but fourth order for $\nu = 30.23$ (in the latter case the particle takes four crossings of the $w_1 = \pi$ plane to return to the island on which it started). Outside the islands we see the beginning of stochastic behavior, but the stochastic regions are separated from one another by coherent regions, which prevents the movement of particles from one stochastic region to another. Finally, at $\alpha = 3$, the stochastic regions have begun to merge, although island formations are still evident.

Conditions for Island Formation

Following Walker and Ford,[1] we transform our Hamiltonian into one that is cyclic in the angle variables and so obtain conserved actions. (The technique is valid only for small α.) We begin by expanding the last term of Eq. 2 in a Fourier series.

$$H = J_1 + \nu J_2 - \alpha \sum_{m=-\infty}^{\infty} J_m(\sqrt{2J_1}) \sin (mw_1 - w_2). \tag{3}$$

Here J_m is a Bessel function of the first kind. Using the generating function[2]

$$F_2 = \mathcal{J}_1 w_1 + \mathcal{J}_2 w_2 - \alpha \sum_m \frac{J_m(\sqrt{2\mathcal{J}_1}) \cos (mw_1 - w_2)}{m - \nu}, \tag{4}$$

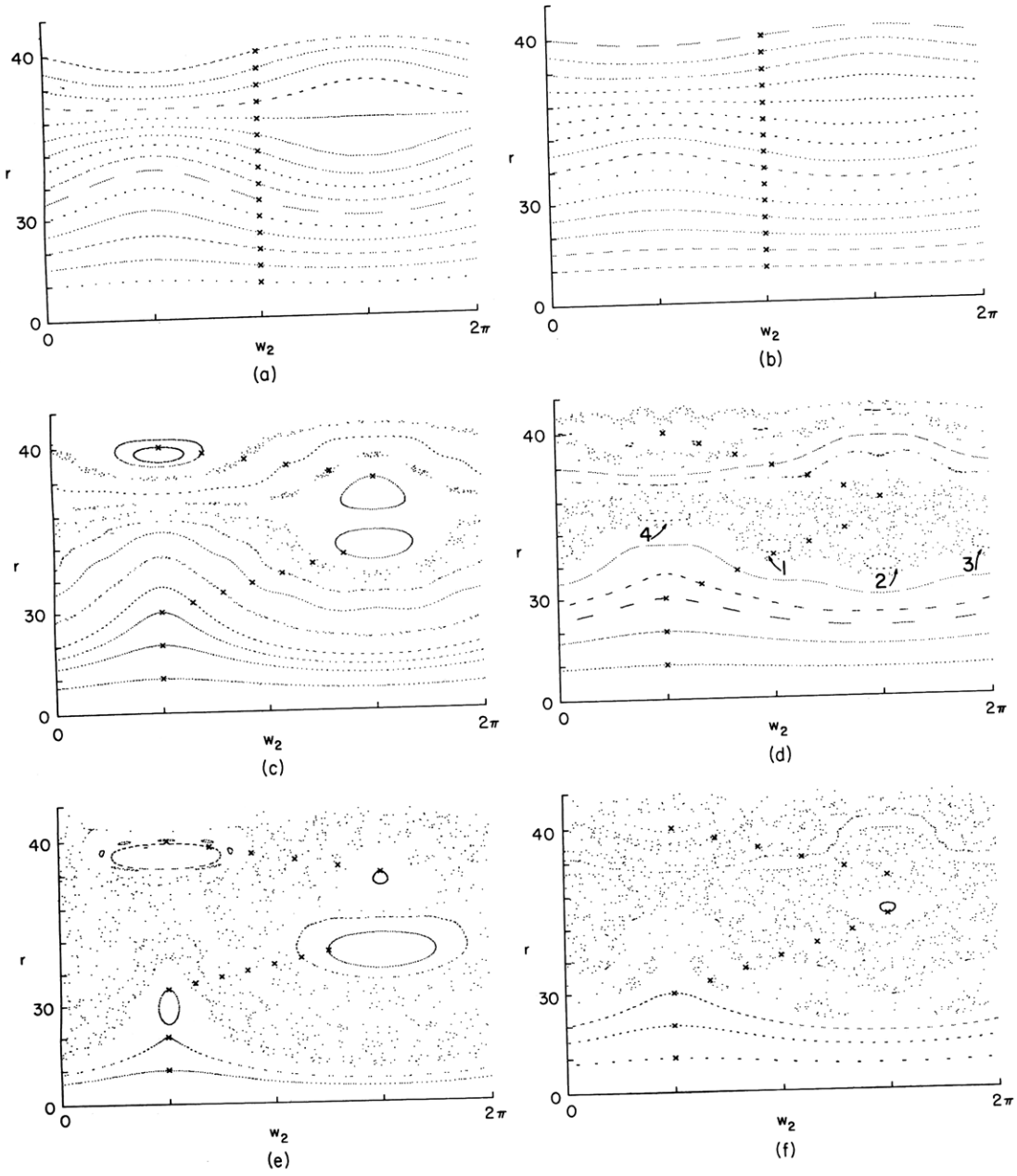

Fig. X-29. $w_1 = \pi$ cross section of phase space. Crosses (X) indicate initial conditions, dots (•) subsequent crossings. In (d) numbers indicate positions of fourth-order island formations and the order in which they are visited.

(a) $\nu = 30.11$, $\alpha = 1$ (b) $\nu = 30.23$, $\alpha = 1$
(c) $\nu = 30.11$, $\alpha = 2$ (d) $\nu = 30.23$, $\alpha = 2$
(e) $\nu = 30.11$, $\alpha = 3$ (f) $\nu = 30.23$, $\alpha = 3$

we obtain the following canonical transformation into action-angle variables $\mathcal{J}_1$, w_1 and $\mathcal{J}_2$, w_2:

$$J_1 = \frac{\partial F_2}{\partial w_1} = \mathcal{J}_1 + a \sum_m \frac{m J_m(\sqrt{2\mathcal{J}_1}) \sin(mw_1 - w_2)}{m - \nu} \tag{5}$$

$$J_2 = \frac{\partial F_2}{\partial w_2} = \mathcal{J}_2 - a \sum_m \frac{J_m(\sqrt{2\mathcal{J}_1}) \sin(mw_1 - w_2)}{m - \nu}. \tag{6}$$

The transformed Hamiltonian

$$\mathcal{K} = H = \mathcal{J}_1 + \nu \mathcal{J}_2 + a \sum_m \left[J_m(\sqrt{2\mathcal{J}_1}) - J_m(\sqrt{2J_1})\right] \sin(mw_1 - w_2). \tag{7}$$

Under the assumption that the transformation is nearly an identity transformation, i.e., $\mathcal{J}_1 = J_1 + O(a)$,

$$\mathcal{K} = \mathcal{J}_1 + \nu \mathcal{J}_2 + O(a^2), \tag{8}$$

so that $\mathcal{J}_1$ and $\mathcal{J}_2$ are approximate constants of the motion. From (5)

$$\mathcal{J}_1 \approx J_1 - a \sum_m \frac{m J_m(\sqrt{2J_1}) \sin(mw_1 - w_2)}{m - \nu}. \tag{9}$$

In order to compare this with the numerical solutions of Fig. X-29, we take $w_1 = \pi$. Equation 9 then reduces to

$$\mathcal{J}_1 \approx J_1 + a \sum_{m=-\infty}^{\infty} \frac{m(-1)^m J_m(\sqrt{2J_1})}{m - \nu} \sin w_2. \tag{10}$$

In Fig. X-30 we use Eq. 10 to plot curves of constant $\mathcal{J}_1$ for the parameters in Fig. X-29. We see that the general features of the primary island formation for $\nu = 30.11$ are well predicted by Eq. 10. The higher order islands formed with $\nu = 30.23$ and $a = 2$ are not predicted by Eq. 10, although for $a = 3$ we see the same first-order island that was observed in Fig. X-29.

From Eq. 10 we can derive the condition for primary island formation by setting $\partial \mathcal{J}_1/\partial w_2 = \partial \mathcal{J}_1/\partial J_1 = 0$. We find that islands occur where

$$a > \left| \frac{r}{\sum_m \frac{m(-1)^m J'_m(r)}{m - \nu}} \right|. \tag{11}$$

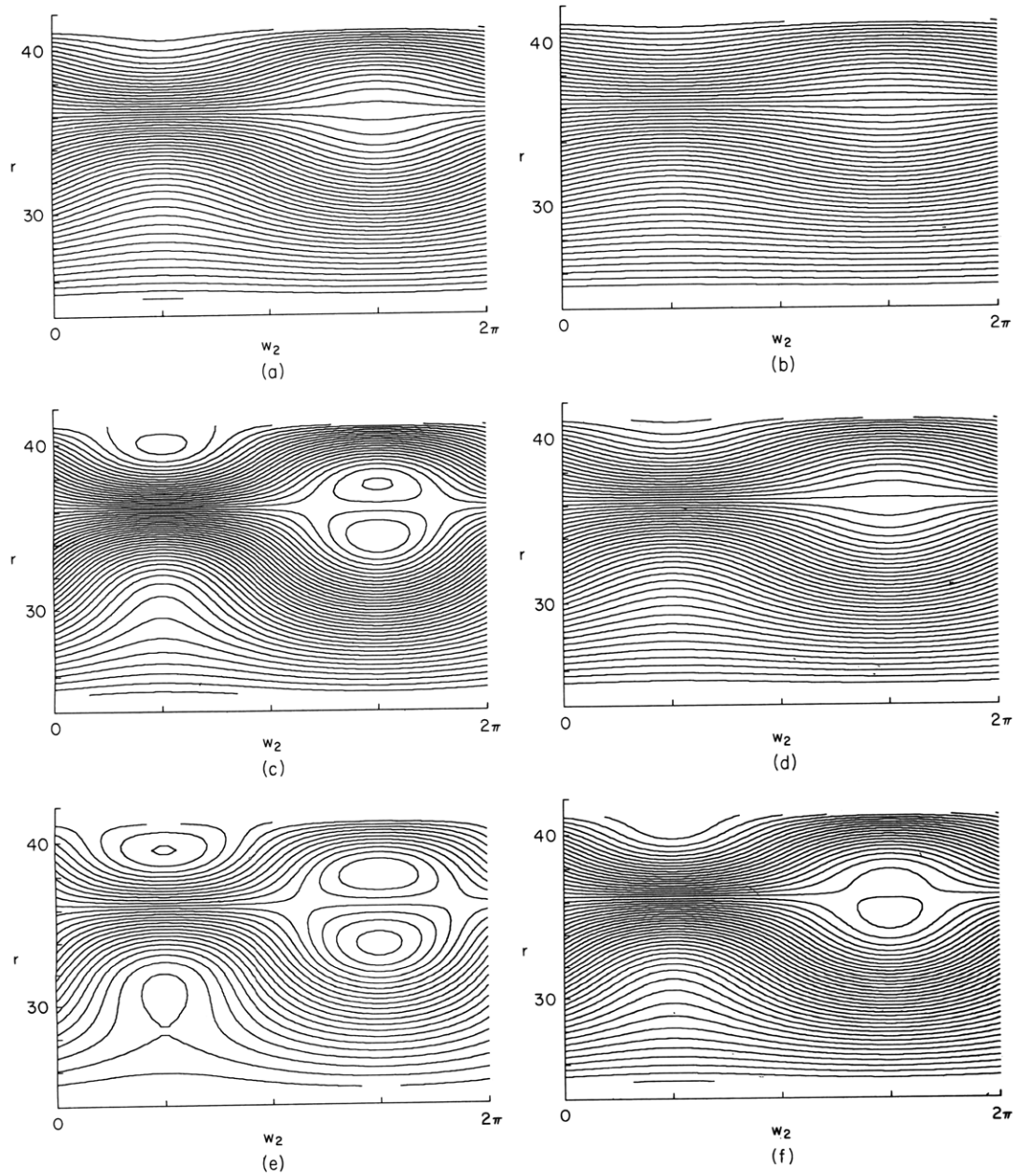

Fig. X-30. Contour plots of the approximate constant of the motion $\mathcal{J}_1$ (see Eq. 9). Parameters for a-f are the same as in Fig. X-29.

If $\nu \approx n$ (an integer), then Eq. 11 can be simplified to give[3]

$$a > \left| \frac{r\delta}{nJ_n'(r)} \right|, \tag{12}$$

where $\delta = \nu - n$.

Conditions for Stochasticity

Although we see from Eq. 12 that the field for primary island formation has a strong dependence on δ, the numerical results in Fig. X-29 indicate that the condition for the merging of stochastic regions is insensitive to δ. This stochasticity criterion is most important from the point of view of heating, since it gives the conditions under which an ion can be heated appreciably.

In Fig. X-31 we plot the extent of the connected stochastic regions as a function of a for $\nu = 30.11$ and 30.23. Since the boundaries of the stochastic region are not necessarily lines of constant r, we plot the intersection of the boundaries with the line $w_2 = 0$.

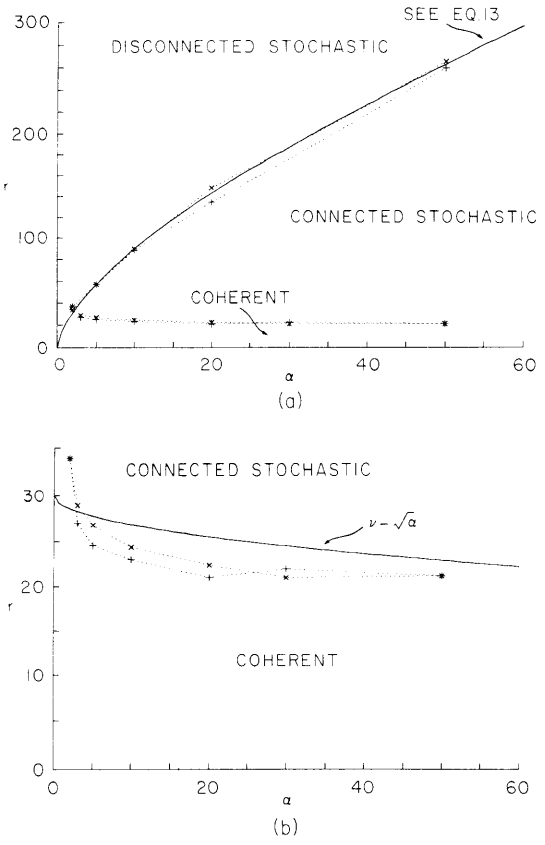

Fig. X-31. (a) Extent of connected stochastic regions as a function of a.
(b) Lower portion of (a) on an expanded scale.
Plus (+) indicates $\nu = 30.11$, cross (X) $\nu = 30.23$.

We observe only coherent motion for r below the lower curves, and disconnected stochastic regions above the upper curves. We may derive an approximate equation for the upper data points by assuming that Eq. 12 gives the correct scaling of the stochasticity condition with r, although not its scaling with δ. We expand asymptotically the Bessel function in Eq. 12, solve for r, and replace δ with Δ to serve as an adjustable parameter, to obtain

$$r = \left(\frac{an}{\Delta}\right)^{2/3} \left(\frac{2}{\pi}\right)^{1/3}. \tag{13}$$

Equation 13 with n = 30 and Δ = 0.28 is shown as a solid curve in Fig. X-31. The close fit suggests that Eq. 13 gives correctly the upper limit to the heating.

Since linear theory shows such a pronounced dependence on δ it is somewhat surprising that Eq. 13 should not depend at all on δ. To understand this, we go back to the linear theory. Consider a particle that at t = 0 has $\dot{y} = -r$ and y = 0. If the particle equation of motion (1) is integrated along its unperturbed orbit for a time 2π, we find that the change in the particle Larmor radius is

$$\Delta r = \frac{2\pi\nu}{r}\, a \cos(\nu\pi + \phi)\, J_\nu(r). \tag{14}$$

(We have approximated the Anger's function arising from this integration by the corresponding Bessel function, since ν is assumed large.) Observe that Eq. 14 does not exhibit a strong δ-dependence (that dependence comes into linear theory when we sum Eq. 14 over many cyclotron periods) and the cos $(\nu\pi + \phi)$ term constructively or destructively interferes, depending on whether or not ν is integral. Substituting Eq. 13 in Eq. 14, we find that at the upper limit of the stochasticity region we have $\Delta r = 2\pi\Delta \cos(\nu\pi + \phi) \cos(r - \nu\pi/2 - \pi/4)$. Thus in order for the motion to be stochastic, we require that the jump in the Larmor radius which the particle makes in one cyclotron orbit be some fraction of the period of the Bessel function appearing in Eq. 14.

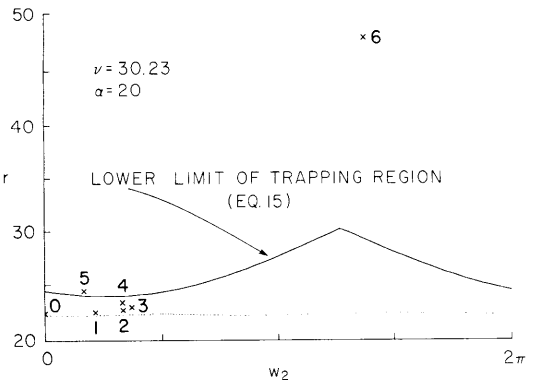

Fig. X-32.

$w_1 = \pi$ cross section of phase space showing the effect of trapping. Dots (•) indicate the particle orbit in the coherent region, crosses (×) the particle orbit just inside the stochastic region. Numbers refer to successive crossings of the $w_1 = \pi$ plane.

This explanation does not satisfactorily explain the lower set of data in Fig. X-31. Presumably, the reason is that whereas the upper limit of the stochastic region is generally quite far removed from $r = \nu$, the lower limit is not, and we expect the strongly nonlinear effect of trapping to be important. In RLE Progress Report No. 117 (pp. 193-197) we gave $r > \nu - \sqrt{a}$ as the condition for trapping; however, it is evident from Fig. X-31b that the stochastic region extends somewhat below the trapping region. Figure X-32 illustrates nicely the distinction between stochastic and trapping regions. The dotted line gives the phase space trajectory of a particle just outside the stochastic region. The solid line above which particles are trapped is

$$r = \nu - \sqrt{a(1 + \sin(w_2 + \nu\pi))}. \tag{15}$$

Crosses show the position of a particle starting within the stochastic region but below the trapping region. Note that the ion gains energy slowly and after the fifth cyclotron orbit it is just inside the trapping region. The sixth cyclotron orbit where the particle velocity is roughly doubled has the same characteristics of the trapped orbits discussed in our previous report. In this case, trapping is clearly the most important mechanism by which the ion becomes heated initially. The importance of the initial slow ion heating is that it allows particles closer to the bulk of the ion distribution to become trapped.

Long-Term Effects and Asymptotic State

In order to understand the long-term behavior of the ions, we integrate the equations for 40 particles with velocities just above the lower limit of the stochastic region and with evenly distributed phases. (This is a model for the heating of the tail of the ion distribution.) In Fig. X-33 we plot rms, maximum, and minimum speeds of the

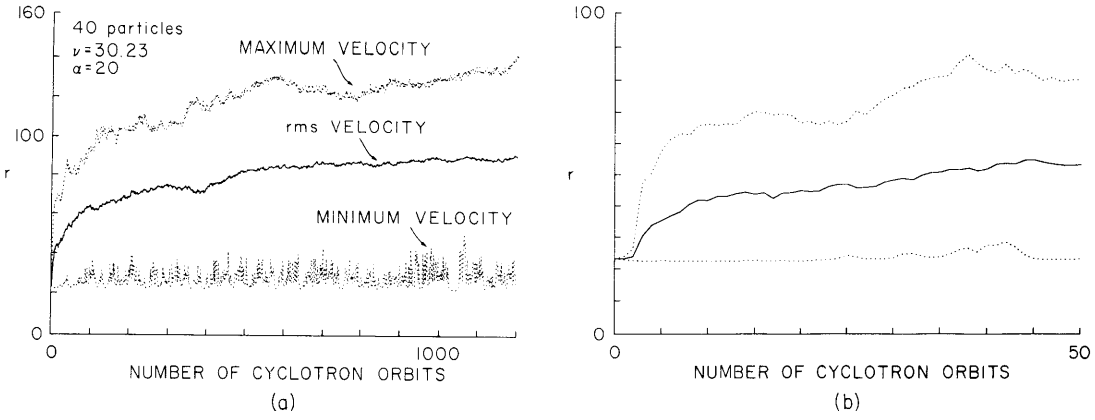

Fig. X-33. (a) Heating of a group of 40 particles with initial velocity r = 23 and evenly distributed phases.
(b) Same as (a) on an expanded scale.

particles as a function of cyclotron orbit number (which is nearly proportional to time) for $\alpha = 20$ and $\nu = 30.23$. We note that for two or three cyclotron orbits the ions are

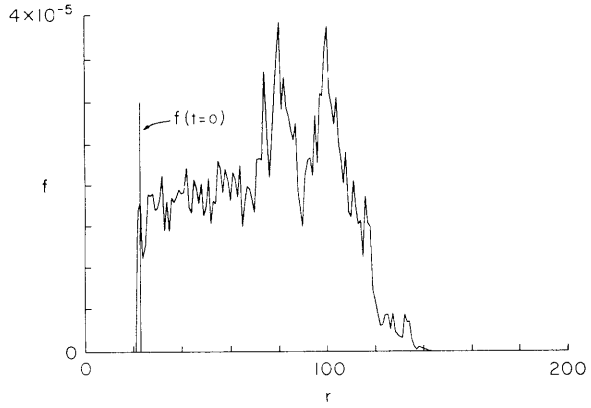

Fig. X-34. Asymptotic distribution function for the particles in Fig. X-33 averaged over cyclotron orbits 900-1200. Normalization is such that $\int_0^\infty 2\pi rf\, dr = 1$. Also shown is the position of the initial δ-function distribution.

heated quite slowly. This is followed by a rapid energy gain as the particles become trapped by the wave, and then by slower heating to an asymptotic rms velocity of approximately 90. The distribution function (Fig. X-34) at this asymptotic state is obtained by averaging over the last 300 cyclotron orbits in Fig. X-33. Note that the effect of the wave is to cause the perpendicular distribution to form a plateau within the stochastic region.

References

1. G. H. Walker and J. Ford, Phys. Rev. 188, 416 (1969).
2. H. Goldstein, Classical Mechanics (Addison-Wesley Press, Inc., Cambridge, Mass., 1951).
3. Equation 12 is identical to the condition for onset of secular perturbations in the particle's phase, and is given by D. J. Sigmar and J. D. Callen, Phys. Fluids 14, 1423 (1971).

3. COMMENT ON "The Nonlinear Filamentation of Lower-Hybrid Cones"

U. S. Energy Research and Development Administration (Contract E(11-1)-3070)

George L. Johnston, Flora Y. F. Chu, Charles F. F. Karney, Abraham Bers

In a recent letter, Morales and Lee[1] investigated the nonlinear distortion of lower hybrid resonance cones in a uniform plasma. Treating nonlinear and dispersive (thermal) effects as small perturbations to the steady-state linearized cold-plasma propagation along a single resonance cone, and assuming that the amplitude of the potential at frequency ω is real, they obtained a modified Korteweg-de Vries (mKdV) equation for the amplitude of the electric field, in the resonance cone. From the existence of soliton solutions of the mKdV equation, they inferred that an external excitation of large-amplitude lower hybrid fields should result in the generation of multiple filaments along which intense electric fields of the soliton shape are formed.

We shall show, however, that in the case of linearized cold-plasma propagation, the condition that power flow into the plasma requires that the amplitude of the potential be complex. Extending this requirement to the case of weakly nonlinear and dispersive propagation, we shall show that the resulting complex form of the mKdV equation has solutions very different from the real form of the equation treated by Morales and Lee.

Consider the case of linearized two-dimensional cold-plasma propagation of lower hybrid waves in a uniform plasma. The potential is $\phi(x, z, t) = \frac{1}{2}\,\tilde{\phi}(x, z)\exp(-i\omega t) + \text{c. c.}$ The partial differential equation satisfied by the complex amplitude $\tilde{\phi}(x, z)$ is

$$K_\perp \frac{\partial^2}{\partial x^2}\tilde{\phi} - |K_\parallel| \frac{\partial^2}{\partial z^2}\tilde{\phi} = 0. \tag{1}$$

The general solution of (1) is

$$\tilde{\phi}(x, z) = \tilde{\phi}_+(z-x/d) + \tilde{\phi}_-(z+x/d), \tag{2}$$

where $d = (K_\perp/|K_\parallel|)^{1/2}$. We determine $\tilde{\phi}_+$ and $\tilde{\phi}_-$ from the boundary condition $\tilde{\phi}(0, z) = \tilde{\phi}_o(z)$, together with the "radiation condition" that the time-averaged power flows away from the boundary $x = 0$ for arbitrary boundary conditions, $\tilde{\phi}_o(z)$. We represent the resonance cone amplitudes $\tilde{\phi}_\pm(z\mp x/d)$ and the boundary-value amplitude $\tilde{\phi}_o(z)$ as Fourier integrals:

$$\tilde{\phi}_\pm(z \mp d^{-1}x) = \frac{1}{2\pi}\int_{-\infty}^{\infty} \exp(ik(z \mp d^{-1}x))\,\tilde{\phi}_\pm(k)\,dk \tag{3}$$

and

$$\tilde{\phi}_o(z) = \frac{1}{2\pi}\int_{-\infty}^{\infty} e^{ikz}\,\tilde{\phi}_o(k)\,dk. \tag{4}$$

Note that $\tilde{\phi}_o(k) = \tilde{\phi}_+(k) + \tilde{\phi}_-(k)$. Making use of the Maxwell equation curl $\underline{\tilde{H}}(x, z) = -i\omega\epsilon_o K(\omega) \cdot \underline{\tilde{E}}(x, z)$ and the relation $\underline{E} = -\text{grad}\ \tilde{\phi}$, we obtain $\tilde{H}_y(k)$ and $\tilde{E}_z(k)$ in terms of $\tilde{\phi}_\pm(k)$, and through the use of Parseval's theorem,

$$\int_{-\infty}^{\infty} \overline{S_x(x, z)}\, dz = \frac{1}{4\pi}\omega\epsilon_o K_\perp d^{-1} \int_{-\infty}^{\infty} k\left[|\tilde{\phi}_+(k)|^2 - |\tilde{\phi}_-(k)|^2\right] dk. \tag{5}$$

From the requirement that the power-flow integral be positive for arbitrary boundary conditions, $\tilde{\phi}_o(z)$, we conclude that $\tilde{\phi}_+(k)$ vanishes for negative values of k and $\tilde{\phi}_-(k)$ vanishes for positive values of k. This conclusion permits us to represent the resonance-cone functions in terms of $\tilde{\phi}_o(z)$ by

$$\tilde{\phi}_\pm(z) = \frac{1}{2}\tilde{\phi}_o(z) \pm \frac{1}{2\pi i} P \int_{-\infty}^{\infty} \frac{\tilde{\phi}_o(s)}{s - z}\, ds \tag{6}$$

which shows that $\tilde{\phi}_\pm(z)$ are necessarily complex functions of z.

The same requirement must be extended to the case of weakly nonlinear and dispersive propagation. Instead of the mKdV equation

$$v_\tau + (v^3)_\xi + v_{\xi\xi\xi} = 0, \tag{7}$$

in which the field amplitude v is real, we then, by means similar to (1), obtain

$$v_\tau + (|v^2|\, v)_\xi + v_{\xi\xi\xi} = 0, \tag{8}$$

in which the field amplitude v is complex. We shall henceforth refer to (7) as RmKdV and to (8) as CmKdV.

We have found traveling-wave solutions $v(\xi - u\tau)$ of CmKdV. Let $v(\zeta) = A(\zeta)\, e^{i\theta(\zeta)}$ (A and θ are real variables). Then upon integration CmKdV becomes

$$A_{\zeta\zeta} - \theta_\zeta^2 A + A^3 - uA = 0 \tag{9}$$

$$2A_\zeta\theta_\zeta + A\theta_{\zeta\zeta} = 0 \tag{10}$$

where we have set the integration constants equal to zero. Equation 10 may be integrated to give

$$\theta_\zeta = \frac{C_1}{A^2}. \tag{11}$$

Substitution of (11) in (9) yields

$$\xi = \frac{1}{\sqrt{2}} \int \frac{dA^2}{\left(-A^6 + 2uA^4 + 2C_2A^2 - 2C_1^2\right)^{1/2}}, \tag{12}$$

where C_2 is a second constant of integration. There are two cases to be considered. If C_1 is zero, then taking $C_2 = 0$ we find the only solitary wave solution to Eq. 12:

$$v = e^{i\theta} \sqrt{2u} \operatorname{sech} \left[\sqrt{u}\ (\xi - u\tau)\right] \tag{13}$$

and θ is constant. This is a trivial extension of the RmKdV soliton but it cannot be a solution of the physical system, since it has both positive and negative k components.

If C_1 is nonzero, then the requirement that A be real gives the envelope of v as an elliptic function. One special solution in this class is

$$v(\xi, \tau) = A\, e^{i\kappa(\xi - u\tau)} \tag{14}$$

where the amplitude, A, is a constant. A, κ, and u satisfy the nonlinear dispersion equation

$$u = |A|^2 - \kappa^2. \tag{15}$$

This is just the linear dispersion relation for a uniform plane wave, except that the presence of the finite-amplitude wave has reduced the plasma density everywhere. Note that (14) can satisfy the requirement that only positive k components exist.

We have conducted a preliminary investigation of the stability of the solution given in (14). We find that it is unstable when $|A|^2 < 6\kappa^2$.

Professor Chu's research is supported by funds from the Dugald C. Jackson Professorship of the Department of Electrical Engineering and Computer Science.

Reference

1. G. J. Morales and Y. C. Lee, Phys. Rev. Letters 35, 930 (1975).

4. ELECTROMAGNETIC CORRECTIONS TO THE LOWER HYBRID WAVE AND ITS GROUP VELOCITY RAY

U. S. Energy Research and Development Administration (Contract E(11-1)-3070)

Kim S. Theilhaber, Abraham Bers

In this report we consider rather qualitatively the penetration of lower hybrid waves into a magnetized plasma with a density gradient. Several authors, using an electrostatic approximation for the dispersion relation of the lower hybrid waves, have treated this problem.[1-3] We shall show here that electromagnetic corrections to the dispersion relation can be important and may modify considerably the field structure predicted by the relatively simple electrostatic approximation.

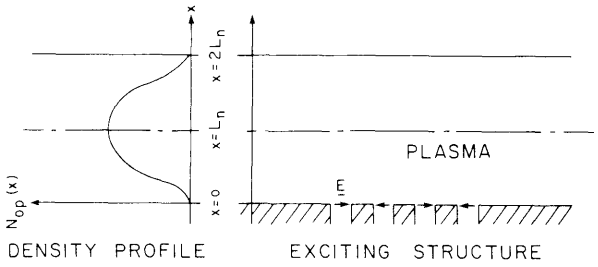

Fig. X-35. Geometry for wave penetration into the plasma.

We consider a two-dimensional geometry (Fig. X-35) in which the density profile, given by $N_{op}(x)$, is taken as arbitrary, with the maximum density occurring at $x = L_n$. For an infinite sinusoidal excitation along the $x = 0$ boundary

$$\underline{E}(x=0, z) \sim \exp -i \frac{\omega}{c} n_z z \tag{1}$$

the "local" cold-plasma dispersion relation for n_x is

$$K_\perp n_x^4 + \left\{(K_\perp + K_\parallel)\left(n_z^2 - K_\perp\right) + K_x^2\right\} n_x^2 + K_\parallel \left\{\left(n_z^2 - K_\perp\right)^2 - K_x^2\right\} = 0, \tag{2}$$

where in the frequency range $\Omega_i \ll \omega \ll \Omega_e$ ($\Omega_{i,e}$ denote the cyclotron frequencies)

$$K_\perp \cong 1 + \frac{\omega_{pe}^2(x)}{\Omega_e^2} - \frac{\omega_{pi}^2(x)}{\omega^2}$$

$$K_x \cong \frac{\omega_{pe}^2(x)}{\omega \Omega_e}$$

$$K_{\parallel} = 1 - \frac{\omega_{pe}^2(x)}{\omega^2}. \tag{3}$$

In the bulk of the density profile, $|K_{\parallel}|$ and $K_x^2 \gg 1$. The "slow-wave" (lower hybrid) solution of Eq. 2 is then

$$n_x^2 = -\frac{K_{\parallel}}{2K_{\perp}}\left[\left(n_z^2 - K_{\perp} - a^2\right) + \sqrt{\left(n_z^2 - K_{\perp} - a^2\right)^2 - 4a^2 K_{\perp}}\right], \tag{4}$$

where $a^2 \equiv \omega_{pe}^2(x)/\Omega_e^2$. The accessibility condition,[4] $n_z > n_{z\ell}$, guarantees that n_x^2 is real in the entire length of the density profile, or equivalently that

$$\left[n_z^2 - K_{\perp}(x) - a^2\right]^2 \geq 4a^2(x)\, K_{\perp}(x), \tag{5}$$

over $0 \leq x \leq L_n$. If for a given x we have

$$\left(n_z^2 - K_{\perp} - a^2\right)^2 \gg 4a^2 K_{\perp}, \tag{6}$$

then by a Taylor's expansion the radical in Eq. 4 yields

$$n_x^2 \cong -\frac{K_{\parallel}}{K_{\perp}}\left(n_z^2 - K_{\perp} - a^2\right). \tag{7}$$

Furthermore, if

$$n_z^2 \gg K_{\perp} + a^2, \tag{8}$$

then the slow-wave dispersion relation yields

$$n_x^2 \cong -\frac{K_{\parallel}}{K_{\perp}} n_z^2, \tag{9}$$

which is simply the electrostatic dispersion relation found from $\hat{k} \cdot \underline{\underline{K}} \cdot \hat{k} = 0$. Since in general $K_{\perp}$ and $a^2 \sim O(1)$, Eq. 8 requires that $n_z^2 \gg 1$ for Eq. 9 to be valid. When $n_z^2 \sim O(1)$, electromagnetic "corrections" become important and Eq. 4 or Eq. 7 must be used. Since $n_{z\ell} \sim O(1)$, in most cases there will be a range of values of n_z near accessibility where the electromagnetic corrections are important.

We shall now consider the effect of the corrections on the ray trajectories in the plasma. The rays $z = z_R(x, n_z)$ are given by

$$\frac{dz_R}{dx} = -\frac{\partial n_x}{\partial n_z}.$$

From Eq. 4 we get

$$\frac{dz_R}{dx} = \frac{n_z}{n_x}\left(\frac{K_\parallel}{2K_\perp}\right)\left(\frac{\left(n_z^2-K_\perp-a^2\right)}{\sqrt{\left(n_z^2-K_\perp-a^2\right)^2 - 4a^2K_\perp}} + 1\right). \tag{10}$$

For large n_z this expression is independent of n_z:

$$\frac{dz_R}{dx} = \left(-\frac{K_\parallel}{K_\perp}\right)^{1/2}; \qquad (n_z \gg 1). \tag{11}$$

Linear and parabolic density profiles are shown in Fig. X-36, and plots of ray trajectories are shown in Fig. X-37. Note that for values of $n_z \gg 1$, the ray trajectories differ

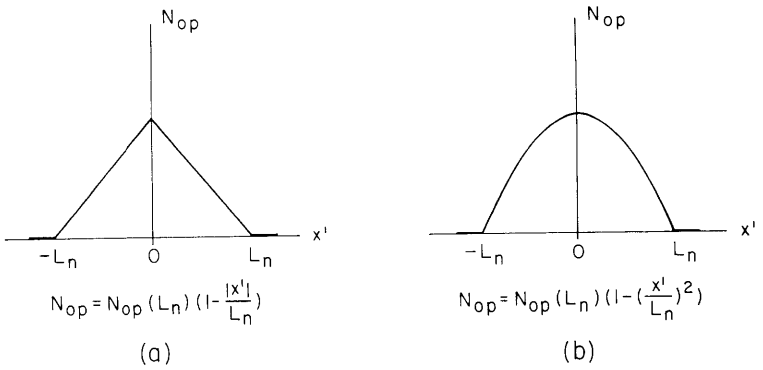

Fig. X-36. (a) Linear and (b) parabolic density profiles.

very little, as predicted by Eq. 11. On the other hand, when $n_z \to n_{z\ell}$, the rays are strongly divergent. With $n_z = n_{z\ell}$, the radical in Eq. 10 is zero at some $x = x_o$ inside the density profile and the ray trajectory is asymptotic to the line $x = x_o$. More spreading is also obtained with a parabolic density profile, since higher densities where dz_R/dx is larger are encountered earlier along the ray trajectory (compare Fig. X-37a and X-37b). Finally, the effect of the lower hybrid resonance is illustrated in Fig. X-37c. The rays travel a finite distance in z before encountering the lower hybrid resonance layer.

A source of finite extent in z at x = 0 imposes an excitation spectrum composed of many n_z components. Now the field structure inside the plasma is determined in part by the structure of the ray trajectories of Eq. 10, which give the direction of energy flow in the plasma. Thus, unless the source is designed to exclude n_z components near accessibility, the extent of the fields inside the plasma may be many times larger than

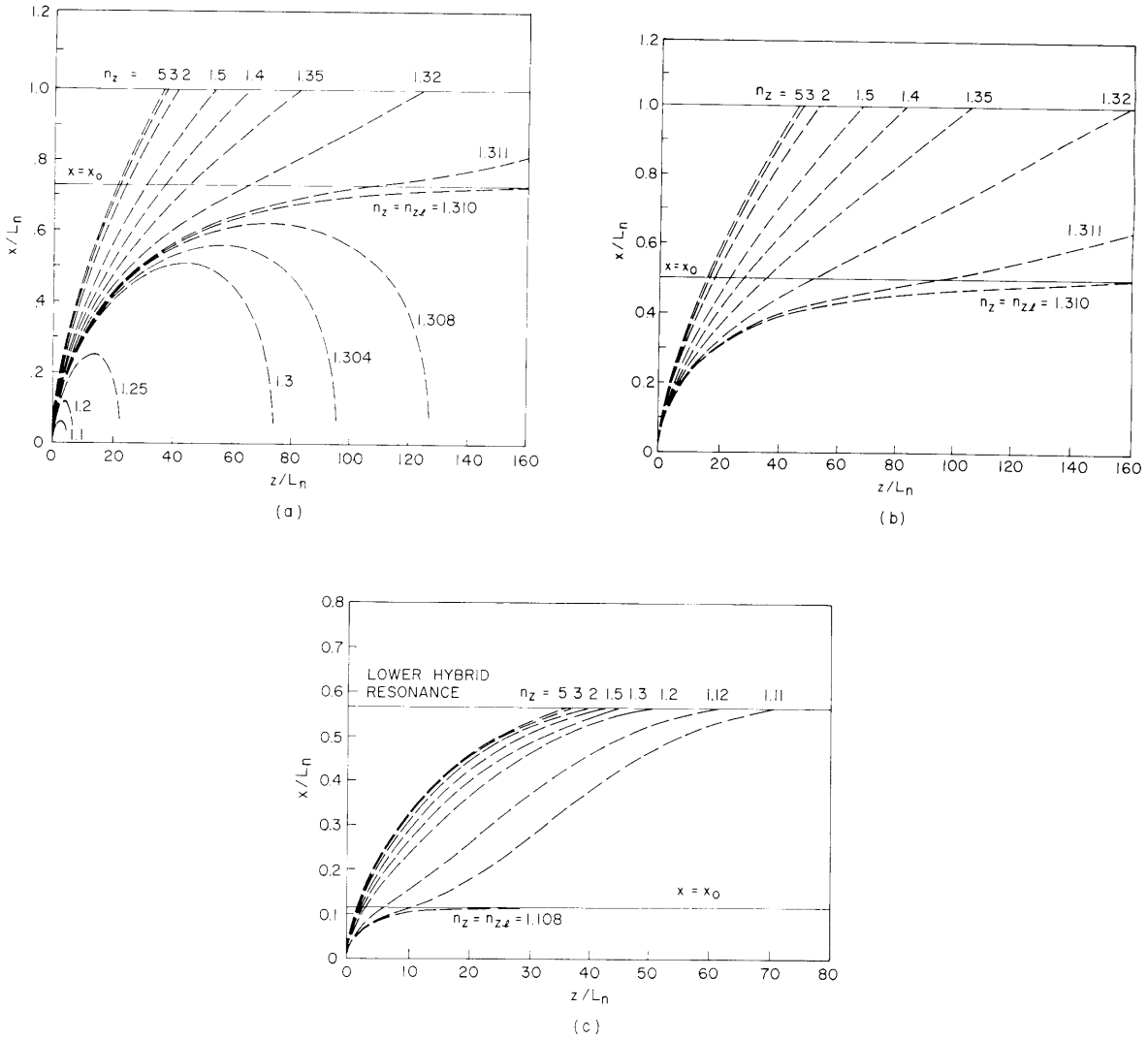

Fig. X-37. (a) Ray trajectories in a linear density profile. Parameters: B_o = 5T, $N_{op}(L_n) = 10^{14}$ cm^{-3}, $\omega = 1.2\ \omega_{LH}$ (ω_{LH} refers to the resonance frequency at the maximum density). For this case $n_{z\ell} = 1.310$.

(b) Same parameters as in (a) with a parabolic density profile.

(c) Ray trajectories with lower hybrid resonance layer: B_o = 5T, $N_{op}(L_n) = 10^{14}$ cm^{-3}, $\omega = 0.8\ \omega_{LH}$. For this case $n_{z\ell}$ = 1.108.

that predicted by the electrostatic approximation alone (Eq. 11). In the latter case, the fields are limited to a region between the two "resonance cone" lines, and the extent of the field in z remains essentially that of the source. With electromagnetic corrections the rays diverge and the field extent is greatly increased.

We should not conclude on the basis of Fig. X-37, where the $n_z = n_{z\ell}$ ray is infinite, that the field extent will also be infinite. The ray trajectory concept is a WKB approximation that breaks down when n_z is close to $n_{z\ell}$. Theilhaber has found[5] that this breakdown occurs when $n_z - n_{z\ell} < O(0.1)$. Inspection of Fig. X-37 shows that considerable spreading of the rays still occurs in the range where WKB is valid. When n_z is close to accessibility, we presume that the slow wave is linearly converted (in part or completely) into the fast wave of the cold-plasma dispersion relation. In particular, waves in the range $1 \leq n_z \leq n_{z\ell}$ will be completely reflected back to the walls. The "return trajectories" of these waves are shown in Fig. X-37a.

We have shown that electromagnetic corrections are important in predicting the lower hybrid field structure in a plasma. A more rigorous treatment of this problem will be offered in a future report.

References

1. R. J. Briggs and R. Parker, "Transport of RF Energy to the Lower Hybrid Resonance in an Inhomogeneous Plasma," Phys. Rev. 29, 852 (1972).
2. R. R. Parker, "Alcator Lower Hybrid-Heating Experiment," Quarterly Progress Report No. 102, Research Laboratory of Electronics, M.I.T., Cambridge, Mass., July 15, 1971, pp. 97-111.
3. P. M. Bellan and M. Porkolab, "Propagation and Mode Conversion of Lower Hybrid Waves Generated by a Finite Source," Phys. Fluids 17, 1592 (1974).
4. A. Bers, C. F. F. Karney, and K. S. Theilhaber, "Whistler Wave Excitation and Its Parametric Down-conversion to Electrostatic Ion Cyclotron Waves," RLE Progress Report No. 115, Research Laboratory of Electronics, M.I.T., January 1975. pp. 184-204.
5. K. S. Theilhaber, "Microwave Heating of a Plasma by Whistler Waves." S.M. Thesis, Department of Electrical Engineering and Computer Science, M.I.T., June 1976.

5. WHISTLER WAVE FIELD STRUCTURE INSIDE A LINEAR DENSITY PROFILE

U.S. Energy Research and Development Administration (Contract E(11-1)-3070)

Kim S. Theilhaber, Abraham Bers

Introduction

In previous reports[1, 2] we examined the feasibility of using whistler waves to heat a Tokamak plasma. We present here a more rigorous treatment of the problem of field penetration into the density of a Tokamak. As before, we consider the two-dimensional geometry illustrated in Fig. X-38. A waveguide array radiates into the plasma, whistler waves are excited and carry energy into the plasma interior. We shall review some results obtained by Theilhaber[3] pertaining to the field structure inside the plasma.

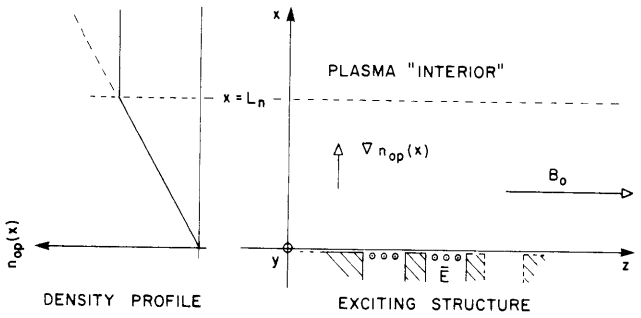

Fig. X-38. Geometry for wave penetration into the linear density profile with input field polarizations.

Infinite Excitation

We consider first the effect of a simple sinusoidal excitation along the plasma boundary. The imposed field is given by

$$\underline{E}(x=0, z) = \hat{y}E_{yo} \exp\left(i\frac{\omega}{c} n_z z\right) \tag{1}$$

and we assume that n_z satisfies the accessibility conditions[1] for penetration into the plasma interior, i.e., $n_z > n_{z\ell}$. For simplicity, we assume that the density profile is linear, with particle density given by

$$N_{op}(x) = \frac{x}{L_n} N_{op}(L_n). \tag{2}$$

Written in component form, the wave equation for the electric field is

$$in_z \frac{dE_z}{d\xi} + \left(K_\perp - n_z^2\right) E_x - iK_x E_y = 0 \tag{3a}$$

$$\frac{d^2E_y}{d\xi^2} + iK_x E_x + \left(K_\perp - n_z^2\right) E_y = 0 \tag{3b}$$

$$\frac{d^2E_z}{d\xi^2} + in_z \frac{dE_x}{d\xi} + K_\parallel E_z = 0 \tag{3c}$$

where for simplicity we define $\xi = \frac{\omega}{c}x = k_o x$. The factors $K_\perp$, $K_\parallel$, and K_x are components of the cold-plasma dielectric tensor. With Eq. 2 we have

$$K_x = \beta\xi \qquad \text{where} \qquad \beta = \frac{\omega_{pi}^2(L_n)}{\omega\Omega_i} \cdot \frac{1}{k_o L_n} \tag{4a}$$

$$K_{\parallel} = 1 - a_o\xi \qquad a_o = \frac{\Omega_e}{\omega}\beta \tag{4b}$$

$$K_{\perp} = 1 - \gamma\xi \qquad \gamma = \frac{\Omega_i}{\omega}\left(1 - \frac{\omega^2}{\Omega_e\Omega_i}\right)\beta \tag{4c}$$

The "fast" (whistler) wave and "slow" (lower hybrid) wave cutoffs occur, respectively, at

$$\xi_{cs} = \frac{1}{a_o} \ll 1$$

$$\xi_{cf} = \frac{n_z^2 - 1}{\beta} \sim O(1). \tag{5}$$

By eliminating two components of the electric field, we can obtain from Eqs. 3 a single fourth-order equation for E_y.

$$\sum_{j=0}^{4} A_j(\xi) \cdot \frac{d^j}{d\xi^j} E_y(\xi) = 0. \tag{6}$$

In the bulk of the plasma ($\xi \gg \xi_{cf} \gg \xi_{cs}$) we have

$$A_4(\xi) \cong K_{\perp} \sim O(1)$$

$$A_3(\xi) \cong -\left(\frac{3 - \gamma\xi}{\xi}\right) \sim O(1)$$

$$A_2(\xi) \cong -K_{\parallel}\left(n_z^2 - K_{\perp} - a^2\right) \sim O\left(\frac{1}{\epsilon^2}\right)$$

$$A_1(\xi) \cong -\beta^2 \sim O(1)$$

$$A_o(\xi) \cong -K_{\parallel}K_x^2 \sim O\left(\frac{1}{\epsilon^4}\right), \tag{7}$$

where ϵ is an ordering parameter, $\epsilon \ll 1$. In the bulk of the plasma we can solve Eq. 6 by WKB. We write

$$E_y \sim \exp[S_o(\xi) + S_1(\xi) + S_2(\xi) + \ldots], \tag{8}$$

where $S_o \sim O\left(\frac{1}{\epsilon}\right)$, $S_1 \sim O(1)$ and $S_2 \sim O(\epsilon)$. We obtain, for the first two terms of the expansion,

$$S_o(\xi) = \pm i \int_{\xi_{cf}}^{\xi} n_{xf}(\xi')\, d\xi' \tag{9a}$$

$$\frac{dS_1}{d\xi} = -\left(\frac{3A_4\left(n_x^2\right)' + A_3\left(n_x^2\right) - A_2(\log n_x)'}{4A_4 n_x^2 - 2A_2} \right) \tag{9b}$$

where $n_x = n_{xf}$ is given by the fast branch of the homogeneous cold-plasma dispersion relation. We shall assume only outgoing waves and hence choose the minus sign in Eq. 9a. The "physical optics" WKB solution that we use is obtained by retaining only S_o and S_1 in the expansion of Eq. 8.

Equation 6 has two turning points occurring near the fast- and slow-wave cutoffs. Near the fast-wave cutoff, the solution that connects to the fast-wave WKB solution (Eq. 8) satisfies approximately

$$\frac{d^2}{d\xi^2} E_y^f + \left(\frac{\beta^2 \xi^2}{n_z^2 - 1} - \left(n_z^2 - 1\right) \right) E_y^f = 0, \qquad \xi \gg a_o^{-1/3}. \tag{10}$$

Near the slow-wave cutoff Eq. 6 cannot be approximated by a second-order equation. Tang and Wong[4] have treated the problem of propagation near the slow-wave cutoff and in his Master's thesis Theilhaber[3] has used their results to show that the effect on $E_y(x)$ of "tunneling" near the slow-wave cutoff is small. We can take $E_y(x=0) = E_{yo}$ as the approximate boundary condition to Eq. 10. We then complete the solution of the problem by matching the solutions of Eq. 10 (which are parabolic cylinder functions) with the WKB solution (8). In the bulk of the plasma $E_x = -i \frac{n_x^2}{K_x} E_y$ is the dominant component of the electric field. The complete WKB solution, which includes tunneling through the cut-offs, is

$$E_x^f(x, n_z) = B(x, n_z) \left[\exp(-i\Phi(x, n_z)) \right] E_{yo}(n_z), \tag{11}$$

where

$$\Phi(x, n_z) = k_o \int_{x_{cf}}^{x} n_{xf}(x')\, dx' \tag{12}$$

$$B(x, n_z) = \frac{-i\left(\frac{\Omega_e}{\omega}\right)^{1/2} \left(n_z^2 - 1\right)^{5/4}}{(2a)^{1/4}\,(1+e^{\pi a})^{1/4}\,W\left(\frac{a}{2}, 0\right)} \cdot e^{-iK_2}$$

$$\cdot \frac{n_x^{3/2}}{K_x} \left(-K_{\parallel} \sqrt{\left(n_z^2 - K_\perp - a^2\right)^2 - 4a^2 K_\perp}\right)^{-1/2}$$

$$\cdot \exp\left(\int_{x_{cf}}^{x} \frac{A_2' - n_x^2(2A_4' - A_3)}{(-2K_{\parallel})\sqrt{\left(n_z^2 - K_\perp - a^2\right)^2 - 4a^2 K_\perp}}\, d(k_o x)\right) \tag{13}$$

$$K_2 \cong \frac{\pi}{4} + \frac{a}{2}\left(\log \frac{(1+a^2)^{1/2}}{a} - 0.4\right) - \tan^{-1}(\kappa) \tag{14}$$

$$a = \xi_{cf}\left(n_z^2 - 1\right)^{1/2}; \qquad \kappa = (1+e^{\pi a})^{1/2} - \exp\left(\frac{\pi}{2} a\right) \tag{15}$$

and W refers to a parabolic cylinder function

$$W^2\left(\frac{a}{2}, 0\right) = \frac{1}{2^{3/2}} \left| \frac{\Gamma\left(\frac{1}{4} + i\frac{a}{4}\right)}{\Gamma\left(\frac{3}{4} + a\frac{a}{4}\right)} \right|. \tag{16}$$

The amplification $|B(x, n_z)|$ plotted as a function of x for several values of n_z is shown in Fig. X-39.

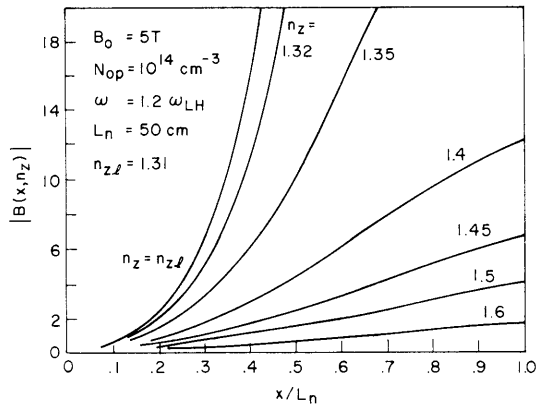

Fig. X-39. WKB amplification of the electric field.

Comparison of Power Coupled into Slow and Fast Waves

The field (1) imposed at x = 0 also excites slow (lower hybrid) waves in the plasma. The ratio of power densities coupled into fast and slow waves is given by

$$\frac{S_x^f}{S_x^s} = \frac{\left(n_z^2 - 1\right)^{7/2}}{2n_z} (2\alpha)^{-1/2} (1 + e^{\pi\alpha})^{-1/2} W\left(\frac{\alpha}{2}, 0\right)^{-2} \frac{\Omega_e}{\omega} \frac{1}{\beta}. \tag{17}$$

This ratio is plotted against n_z in Fig. X-40 for the case of Fig. X-39. In some cases the power coupled into the slow wave can be considerable. In particular, coupling to the fast wave becomes relatively inefficient for very abrupt density gradients.

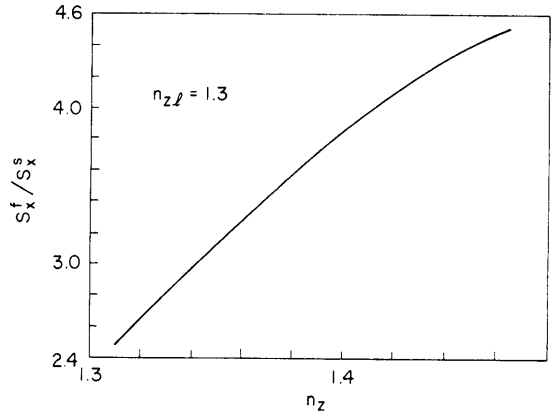

Fig. X-40. Ratio of powers coupled into fast and slow waves. Plasma parameters same as in Fig. X-39.

Validity of the WKB Approximation

The WKB solution of Eq. 11 is valid as long as the contribution from $S_2(\xi)$ in Eq. 8 is small. The results of Theilhaber[3] indicate that typically S_2 is small for $n_z - n_{z\ell} > O(0.1)$. When n_z is close to $n_{z\ell}$ WKB breaks down, and there is strong coupling between fast and slow waves in the bulk of the plasma. Presumably, the fast wave is linearly converted to the slow branch of the dispersion relation and its transmitted amplitude decreases. For instance, in the example (Fig. X-39), where $n_{z\ell} = 1.3$, WKB breaks down when $n_z < 1.4$. Since we have not solved the wave penetration problem in the range $1.3 < n_z < 1.4$, we shall assume in this case, as in others, that the transmitted wave amplitude for $n_z \lesssim 1.4$ is small and hence negligible.

Field Structure

We shall now find the field structure corresponding to a source of finite extent at the boundary. The contribution of the $n_z > 0$ components in the excitation spectrum is

$$E_x^{(R)}(x, z) = \int_{n_{zL}}^{\infty} B(x, n_z)\, E_{yo}(n_z)\, e^{-i\psi(x, z, n_z)}\, d(k_o n_z). \tag{18}$$

Here n_{zL} is the "effective" lower bound for accessibility below which WKB breaks down. In Fig. X-39, $n_{zL} \cong 1.4$. The total phase function $\psi = \phi + k_o n_z z$ is plotted in Fig. X-41. For a given z, the point of stationary phase, for which $\frac{\partial \psi}{\partial n_z} = 0$, occurs at an $n_z \equiv n_o$ given by

$$Z_R(x, n_o) = Z, \tag{19}$$

where Z_R defines the ray trajectory of an n_z component in the medium. $Z_R = Z_R(x, n_z)$ is obtained by integrating the equation

$$\frac{dZ_R}{dx} = -\frac{\partial n_x}{\partial n_z} = \frac{n_z}{n_x}\left(-\frac{K_\parallel}{K_\perp}\right)\left(\frac{\left(n_z^2 - K_\perp - a^2\right)}{\sqrt{\left(n_z^2 - K_\perp - a^2\right)^2 - 4a^2 K_\perp}} - 1\right). \tag{20}$$

A plot of ray trajectories for several values of n_z for the case of Fig. X-39 is shown in Fig. X-42. Note that for n_z close to n_{zL} the ray trajectories penetrate at a very shallow

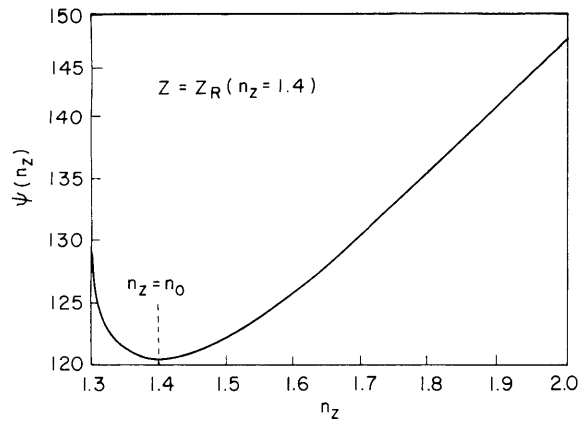

Fig. X-41.

Phase function for the superposition integral. Parameters same as in Fig. X-39.

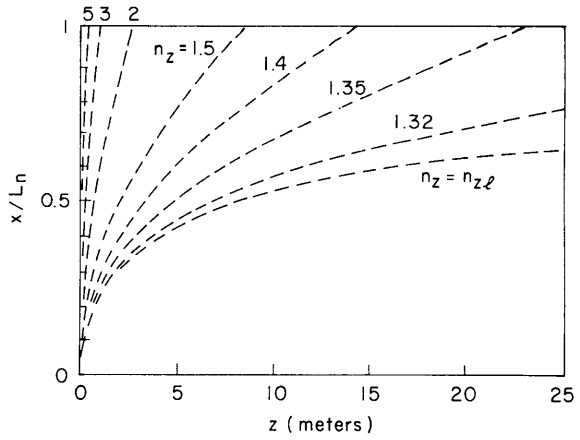

Fig. X-42.

Ray trajectories for several values of n_z. Parameters same as in Fig. X-39.

angle to the magnetic field.

To evaluate the integral of Eq. 18 we consider two kinds of excitation: a "broadband" excitation with a spectrum wide compared with the accessible regime in n_z, and a "narrow-band" excitation with a spectrum narrow in n_z.

In the first case we use stationary phase to evaluate the integral and obtain

$$E_x^{(R)} = B(x, n_o)\, E_{yo}(n_o)\quad e^{-i\frac{\pi}{4}} \left(\frac{2\pi k_o}{|Z'_R(x, n_o)|}\right)^{1/2} \exp[i(k_o n_o Z + \phi(x, n_o))], \tag{21}$$

where $Z'_R \equiv \partial Z_R/\partial n_z$ and, for a given z, n_o is found from Eq. 19. In this expression the fast modulation of $E_x^{(R)}$ is given by the phase factor

$$f = k_o Z n_o(Z) + \phi(n_o(Z)), \tag{22}$$

which has the derivative

$$\frac{df}{dZ} = k_o n_o(Z), \tag{23}$$

so that the local wavelength at a given z is simply that of the $n_z = n_o(Z)$ component in the spectrum. Figure X-43 is a graph of $E_x^{(R)}$ for an impulse excitation in z, $E_{yo}(n_z) = 1$. Note that as the value of z is increased, the value of the stationary phase point n_o, defined by Eq. 19, decreases. For large z, n_o is close to $n_{z\ell}$ (see Fig. X-42). Since for n_o close to $n_{z\ell}$ WKB breaks down, the value of $B(x, n_o(z))$ is unknown for large z. In Fig. X-43 we assume that $B(x, n_z) \to 0$ as $n_z \to n_{z\ell}$, and hence that the field amplitude decreases (broken line) for large z. For the second kind of excitation we consider a Gaussian:

$$E_{yo}(Z) = \exp\left(-\frac{\delta^2}{16}(k_o Z)^2\right) \cdot \cos(k_o N_o Z), \tag{24}$$

which corresponds to a spectrum with peaks of width 2δ in n_z space

$$E_{yo}(n_z) = \frac{1}{k_o \delta \sqrt{\pi}} \left(\exp -\frac{4}{\delta^2}(n_z - N_o)^2 + \exp -\frac{4}{\delta^2}(n_z + N_o)^2\right). \tag{25}$$

Again, using stationary phase but keeping the Gaussian exponential inside the integral, we obtain

$$E_x^{(R)}(Z) = \frac{1}{2} B(N_o) \cdot \exp[-i(k_o n_o Z + \phi(x n_o))] \cdot \frac{1}{(1+\rho^2)^{1/4}} \cdot \exp\left(-\frac{4}{\delta^2}(n_o - N_o)^2 \frac{\rho^2}{1+\rho^2}\right) \tag{26}$$

where $\rho = \dfrac{k_o \delta^2 Z'_R}{8}$ is a measure of the divergence of ray trajectories near $n_z = n_o$.

The field structure for the case of Fig. X-39 and $\delta = 0.1$, $N_o = 1.5$, is shown in Fig. X-44 for several values of x. Note that while the amplification of the field amplitude is not very large (at most 1.5 for $x/L_n = 1$), the total extent in Z is sizably increased

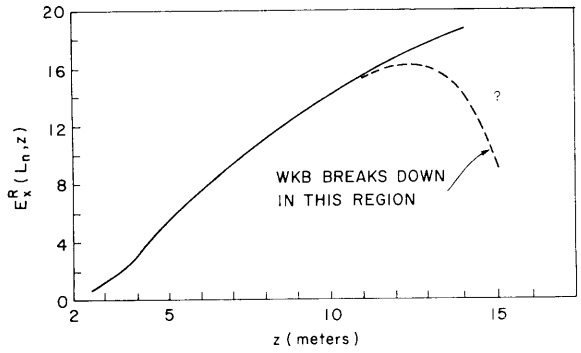

Fig. X-43. Response to a "broadband" excitation, $E_{yo}(n_z) = 1$.

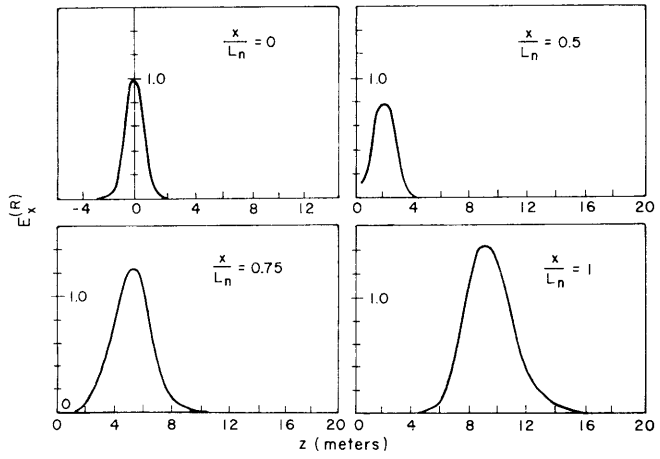

Fig. X-44. Response to a "narrow-band" excitation. Parameters same as in Fig. X-39. $E_x^{(R)}$ vs z (in meters) for several values of x. The excitation has $\delta = 0.1$ and $N_o = 1.5$.

by penetration into the plasma (by a factor of 3 for $x/L_n = 1$). In Figs. X-43 and X-44 we assumed a linear density profile $L_n = 50$ cm long. If we increase the value of L_n, the field structure is modified in two ways. First, the field extent, which is determined by the spread of the ray trajectories, increases in proportion to L_n. Second, the field amplitude decreases because $Z'_R = \partial Z_R/\partial n_z$ increases (Eq. 21) and also because the α-dependent "tunneling" factor in Eq. 13 decreases on account of the greater width of the cutoff region. Similarly, we can predict the effect of changing the shape of the

density profile, for instance, to a parabolic profile where higher densities occur for smaller values of x; the spread of the ray trajectories will be greater while the "tunneling" effect will be smaller. Thus, in this case, both field extent and field amplitude may increase.

Numerous approximations were made in this report. In particular, we ignored the contribution of n_z components near accessibility because the wave-penetration problem for this parameter range has not yet been solved.

References

1. A. Bers, C. F. F. Karney, and K. S. Theilhaber, "Whistler Wave Excitation and Its Parametric Down-conversion to Electrostatic Ion Cyclotron Waves," RLE Progress Report No. 115, Research Laboratory of Electronics, M. I. T., January 1975, pp. 184-204.
2. K. S. Theilhaber and A. Bers, "Whistler Wave Field Structure inside a Linear Density Profile," RLE Progress Report No. 116, Research Laboratory of Electronics, M. I. T., July 1975, pp. 117-127.
3. K. S. Theilhaber, "Microwave Heating of a Plasma by Whistler Waves," S. M. Thesis, Department of Electrical Engineering and Computer Science, M. I. T., June 1976.
4. T. W. Tang and K. C. Wong, "RF Coupling and Mode Conversion at the Lower Hybrid Resonance, University of Massachusetts, January 1975.

6. AC FLUCTUATIONS IN A MULTIFILAMENT ARC SOURCE

U. S. Energy Research and Development Administration (Contract E(11-1)-3070)

Leslie Bromberg, Louis D. Smullin

We have reported previously[1] on a model that describes quantitatively published results of the Berkeley source.[2] We shall now show that the same model can be used to explain the current fluctuations created by the magnetic field of the alternating heating current in the filaments. First, we solve for the effect of the magnetic field on the primary orbits. Then we estimate the effect of this change on the average length of the particles' path in the system. Finally, we include this change in the model for the source and obtain parametric curves.

To solve for the effect of the magnetic field arising from the filament current, we need to calculate the angle by which the primary particle orbit is deflected. Consider the geometry of Fig. X-45. The electric field is perpendicular to the wire. The magnetic field close to the wire is given by

$$I = \frac{\mu_o I}{2\pi r}. \tag{1}$$

Because of the presence of the other wires, it will deviate from the $1/r$ dependence far from the wire. We take this effect into account by introducing a cutoff distance r_c, and supposing the field is $1/r$ up to r_c. As the result will depend on r_c logarithmically, this choice will not be critical. We set r_c equal to one-half the filament interspacing distance.

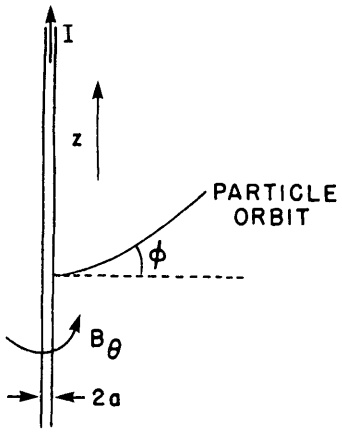

Fig. X-45.
Orbit of a primary electron.

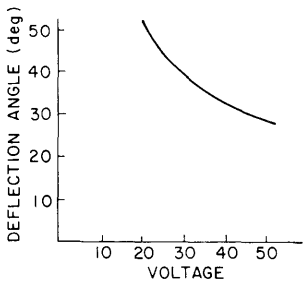

Fig. X-46.
Deflection angle vs sheath voltage drop for filament current = 25 A.

Solving the z-component of the equation of motion, for the deflection angle ϕ (Fig. X-46) we get

$$\phi = \sin^{-1}\left[\frac{e}{m}\frac{\mu_o I}{2\pi}\left(\frac{M_e}{2eV_o}\right)^{1/2}\ln\left(\frac{r_c}{a}\right)\right], \tag{2}$$

where a is the filament wire radius, and V_o the sheath voltage drop. Solutions for ϕ as a function of V_o are shown in Fig. X-46.

In the Berkeley source, as the current changes direction, the angle ϕ oscillates. Thus the electrons from a filament would have a distribution in angles between ϕ and $-\phi$ given by Eq. 2. When the current is zero (which happens twice during a period of oscillation of the heating current), then $\phi = 0$. This variation in angle can produce substantial variation in the mean path length of the multiple-bounce primary electrons.

Monte Carlo Simulation

Because of the nature of the problem, we used a Monte Carlo simulation in order to find the primary path-length distribution. This simulation was done in two dimensions. In our previous calculations,[1] the agreement between the experimental data and the two-dimensional computation was very good. The source geometry is modeled as shown in Fig. X-47. The walls that are not at anode potential reflect the primary electrons.

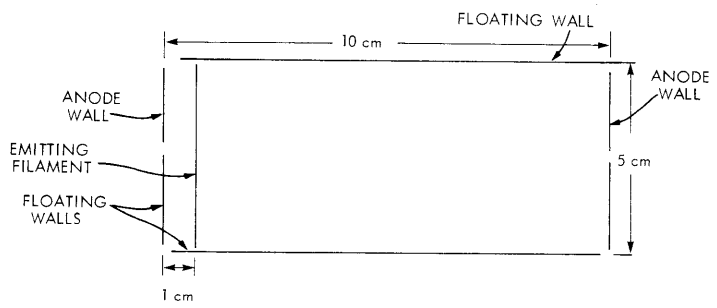

Fig. X-47. Geometry for the Monte Carlo simulation. Particles are started randomly along the filament with random inertial velocity and are followed until they reach the anode wall.

The model is incomplete in that the floating walls do not actually reflect all of the electrons (some have enough energy perpendicular to the wall to surmount the potential barrier), and the simulation is two-dimensional. The results, however, are indicative of what may be happening in the real source.

The electron trajectories are followed in time, and a random-number generator is used to simulate collisions. The mean free path between collisions is set equal to the

value calculated for the Berkeley source.[2]

In the simulation particles traveling more than 60 cm are stopped. The reason for this is that approximately 90% of those particles have lost energy because of excitation or ionizing collisions, and following them further will not change the results. Also, in the real three-dimensional source, particles are not expected to have such large paths.

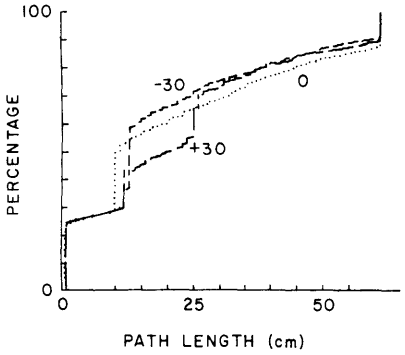

Fig. X-48.

Path-length distribution. Vertical axis is the percentage of particles with path lengths smaller than the number indicated on the ordinate. Parameter is the deflection angle of the primaries (in degrees).

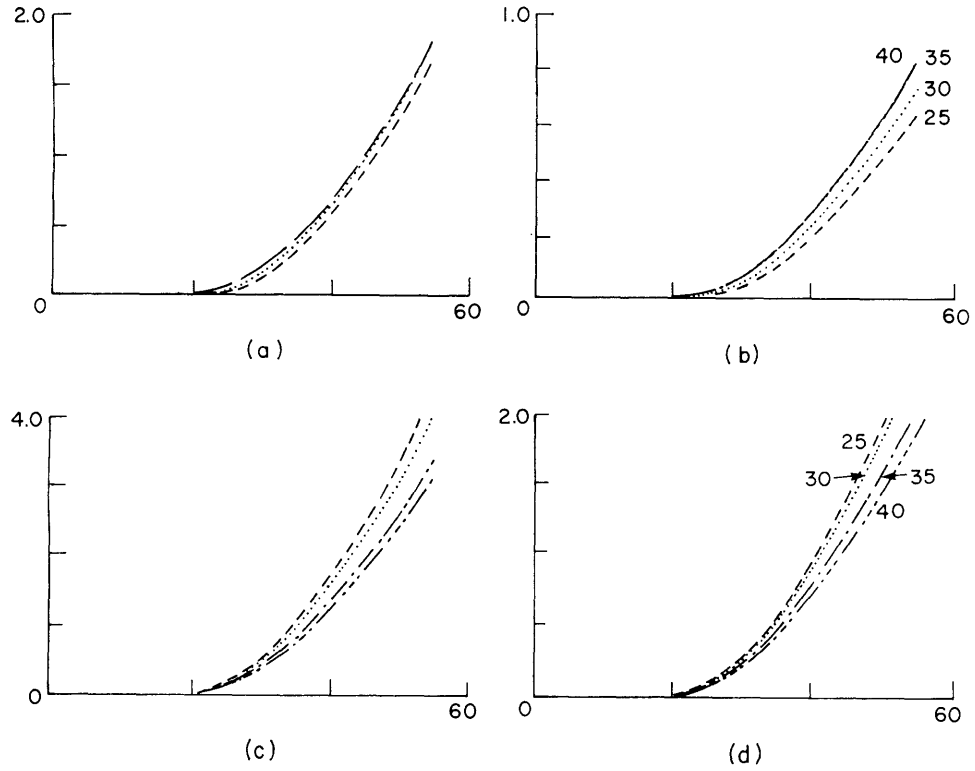

Fig. X-49. Path length of the multiple-bounce electrons = 25, 30, 35, 40 cm.
(a) Arc current vs voltage. Pressure = 7 μm.
(b) Ion saturation current vs voltage. Pressure = 7 μm.
(c) Arc current vs voltage. Pressure = 15 μm.
(d) Ion saturation current vs voltage. Pressure = 15 μm.

A representative result of the simulation is shown in Fig. X-48. The vertical scale gives the percentage of particles that have a path less than the value read on the horizontal axis. Thus we expect the rate of ionization and all of the other dependent quantities to vary accordingly.

In Fig. X-49, we show the predicted behavior of the source. The parameter that is varied is the mean path length of the multiple-bounce electrons. The substantial modulation at twice the heating frequency is obvious.

Appendix

From Fig. X-49 it can be seen that at p = 15 the ion current decreases with the increasing path length of the multiple-bounce electrons, while the opposite effect occurs at p = 7. Then there must be a set of conditions for which

$$\frac{d}{ds} j_{\text{ion saturation}} = \frac{d}{ds}\left[.3 \times Jn_i \left(\frac{2kT_e}{M_i}\right)^{1/2}\right] = 0. \tag{3}$$

With this set of conditions, the fluctuations created by a variation in path length will be minimized.

To find the conditions for which (3) is satisfied, we need to take the derivatives of the equations that provide the solutions for n_e, T_e, and I. First, from (3) we obtain

$$\frac{1}{n_i}\frac{dn_i}{ds} = -\frac{1}{2}\frac{1}{T_e}\frac{dT_e}{ds}. \tag{4}$$

From Crawford's relation[3]

$$\frac{dI}{ds} = \frac{d}{ds} eA_k n_e \left(\frac{kT_e}{2m_e}\right)^{1/2} J_o\left(\frac{eV_k}{kT_e}\right)$$

$$= -I \frac{J'_o\left(\frac{eV_k}{kT_e}\right)}{J_o\left(\frac{eV_k}{kT_e}\right)} = \frac{eV_k}{kT_e}\frac{1}{T_e}\frac{dT_e}{ds}. \tag{5}$$

From the particle conservation equation[4]

$$\frac{dI}{ds}\left\langle \frac{1-e^{-\ell\left(\frac{1}{\ell_i}+\frac{1}{\ell_*}\right)}}{1+\frac{\ell_i}{\ell_*}} \right\rangle_\ell + I\frac{d}{ds}\left\langle \frac{e^{-\ell\left(\frac{1}{\ell_i}+\frac{1}{\ell_*}\right)}}{1+\frac{\ell_i}{\ell_*}} \right\rangle_\ell = 0 \tag{6a}$$

which reduces to

$$\frac{dI}{ds} = -\frac{I\frac{d}{ds}\left\langle e^{-\ell\left(\frac{1}{\ell_i}+\frac{1}{\ell_*}\right)} \right\rangle_\ell}{\left\langle 1+e^{-\ell\left(\frac{1}{\ell_i}+\frac{1}{\ell_*}\right)} \right\rangle_\ell}. \tag{6b}$$

Differentiating the energy conservation equation[5] with respect to s and simplifying, we obtain

$$\frac{1}{s}+\frac{1}{I}\frac{dI}{ds}+\frac{I}{n_e}\frac{dn_e}{ds}=\frac{I}{T_e}\frac{dT_e}{ds}. \tag{7}$$

Combining Eqs. 4, 5, 6b, and 7 yields the condition for which Eq. 3 is valid:

$$\frac{\frac{1}{s}}{\frac{3}{2}\frac{J_o\left(\frac{eV_k}{kT_e}\right)}{J'_o\left(\frac{eV_k}{kT_e}\right)\left(\frac{eV_k}{kT_e}\right)}+1} = \frac{\frac{d}{ds}\left\langle e^{-\ell\left(\frac{1}{\ell_i}+\frac{1}{\ell_*}\right)} \right\rangle_\ell}{\left\langle 1-e^{-\ell\left(\frac{1}{\ell_i}+\frac{1}{\ell_*}\right)} \right\rangle_\ell}. \tag{8}$$

Figure X-50 shows contours of constant ion saturation current as a function of the arc voltage and pressure. Also shown is the solution of Eq. 8 for minimizing the fluctuations. This graph shows that the preferred region of operation is given by the intersection between the minimum fluctuation curve and the desired current density.

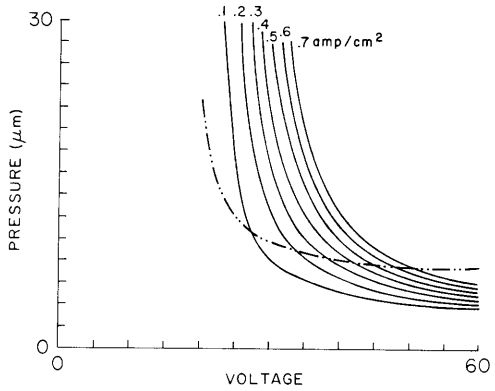

Fig. X-50. Pressure vs voltage for constant ion current density. Broken line shows conditions for minimum ac fluctuations (Eq. 8).

References

1. L. Bromberg and L. D. Smullin, "Thermionic Cathode, Low-Pressure Discharge," RLE Progress Report No. 117, Research Laboratory of Electronics, M. I. T., January 1976, pp. 249-256.
2. W. R. Baker et al., in Proceedings of the Fifth Symposium on Engineering Problems of Fusion Research, Princeton University, 1973.
3. L. Bromberg and L. D. Smullin, op. cit., see Eq. 6.
4. Ibid., see Eq. 5.
5. Ibid., see Eq. 9.

7. LOW-PRESSURE, THERMIONIC CATHODE DIODE

U. S. Energy Research and Development Administration (Contract E(11-1)-3070)

Leslie Bromberg, Louis D. Smullin

The problem of negative-resistance I-V curves in low-pressure, thermionic cathode diodes has often been noted but, except for Langmuir's treatment,[1] the theory has not been developed. Self[2] worked on the plasma-sheath equation, but his results are only useful in the case of symmetrical columns. His interest was in the spatial distribution and he did not solve a self-consistent problem. In this report our main purpose is to predict the behavior of a low-pressure diode in two regimes, the "space-charge-dominated" and the "plasma" regimes.

Space-Charge-Dominated Regime

We shall restrict ourselves to plane-parallel geometry. In other geometries the numerical analysis is more complicated but the results should be similar.

The space charge considered in this regime arises from fast primary electrons and

secondary ions. Secondary electrons do not contribute significantly to the space charge because of the absence of an anode sheath. The secondary electron space charge is of the order of the square root of the mass ratio smaller than the ionic space charge. This defines the regime clearly.

Poisson's equation reduces to

$$\frac{d^2V}{dx^2} = -\frac{1}{\epsilon_o}\left(-\frac{J_o}{\left(\frac{2eV_o}{m_e}\right)^{1/2}} + \int_x^a \frac{J_o n_o \sigma_i(V(x'))\,dx'}{\left[\frac{2e}{M_i}(V(x') - V(x))\right]^{1/2}}\right), \tag{1}$$

where V is the potential, J_o the electron current density, a the anode-cathode distance, n_o the neutral pressure, σ_i the ionization cross section, and V_o the anode-cathode voltage.

After normalization this equation reduces to

$$\frac{d^2\phi}{dz^2} + K\left(\frac{1}{\sqrt{\phi}} - \left(\frac{M_i}{m_e}\right)^{1/2}\int_z^1 \frac{\alpha(\phi(z')V_o)\,dz'}{[\phi(z') - \phi(z)]^{1/2}}\right), \tag{2}$$

where $\phi = V/V_o$, $z = x/a$, $K = J_o a^2/[\epsilon_o\sqrt{(2e/m_e)}\ V_o^{3/2}]$, and $\alpha = n_o\sigma_i(V)$. We multiply by $d\phi/dx$ and integrate to reduce Eq. 2 to

$$\left(\frac{d\phi}{dz}\right)^2 = 4K\left(\phi^{1/2} + (M_i/m_e)^{1/2}\int_z^1 \alpha(z')\left[\sqrt{\phi(z')} - \sqrt{\phi(z') - \phi(z)}\right]dz'\right). \tag{3}$$

Equation 3 is a nonlinear integro-differential eigenvalue problem because $K = K(V_o)$. We can, however, reduce it to a boundary-value problem.

Consider a solution $\phi(z)$ that satisfies the differential equation but not the boundary condition. That is, $\phi(1) = \phi_1 \neq 1$, $K = k_1$, $V_o = P_1$. Then $\psi(z) \triangleq \phi(z)/\phi_1$ is a solution of the problem with $K^1 = \dfrac{K_1}{\phi_1^{3/2}}$ and $V_o^1 = P_1\phi_1$. This can be checked by plugging back into the differential equation (see the appendix).

Similarity rules can be derived for this equation. As long as $n_o a$ is held fixed, $\phi(z)$, V_o, and K do not vary as a or n_o changes. Note, however, that $J_o(\sim K/a^2)$ will change. We conclude, therefore, that all that is needed is a set of curves for one anode-cathode spacing from which solutions for all parameters n_o and a can be derived, by using this similarity rule.

Another approximate similarity rule can be derived. There are two effects if the gas is changed; both the cross section and the ion mass change. When the second effect

is the more important (for example, when the masses are very different), an $n_o \sqrt{M_i}$ similarity rule exists.

The numerical calculations are described in the appendix. Some numerical results are shown in Figs. X-51 and X-52. These curves are drawn for argon. Normalized current density is shown in Fig. X-51. It can be seen that as the pressure increases, the voltage decreases for infinite slope. This theory is valid up to the point where an anode sheath develops and the secondary electron space charge becomes appreciable. The curves could have been extended somewhat further but, because of the large slope, the numerical scheme diverges.

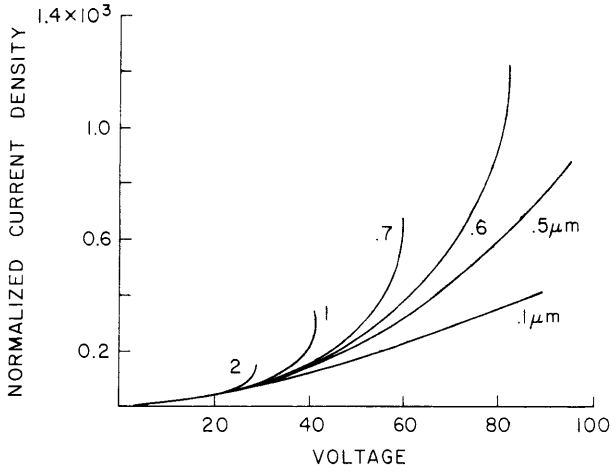

Fig. X-51.

Normalized current density in units of $\epsilon_o \sqrt{2e/m_e} \frac{1}{a^2}$ vs voltage with variable pressure. Plane diode, argon filling gas.

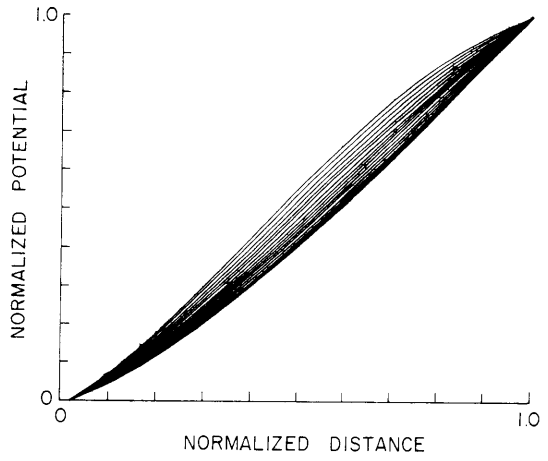

Fig. X-52.

Normalized potential distribution vs normalized distance. Lowest curve is without the presence of the ions. ($V_o < V_{ionization}$). The highest curve corresponds to the I-V curve becoming vertical. Argon pressure, p = 2 μm.

In Fig. X-52 the normalized potential distribution is shown for different voltages. The discharge voltage is being varied up to the point where the I-V curve becomes vertical. Even at this point the secondary electron space charge is negligible.

It is interesting to note that the reason for the break is just space charge and not the presence of a plasma.

Plasma Regime

After the I-V curves become vertical and the ion space charge has increased enough, an anode drop begins to appear. Figure X-53 illustrates what must happen as the current

increases (and the conditions are right). As the anode drop appears, secondary electrons are trapped in a potential well and their space charge becomes important. Since the electric field concentrates near the cathode and anode regions, the problem can be solved in another limit, by using boundary-layer theory. Note that as the electric field recedes toward the electrodes, the Debye length must decrease (the validity of this theory lies in the assumption $\lambda_D/a \ll 1$).

In this limit, the potential distribution at the boundary layer near the anode has been solved by Carusso,[3] and at the boundary layer near the cathode by Crawford.[4] The outer solution (i.e., the solution away from the boundaries) has been solved by Carusso[3] and by Self.[2] Their results for uniform plasma generation are applicable to our study, but care must be taken to redefine the ionizing collision frequency, in order to take into account the fact that only primaries ionize; the plasma electrons do not. Then we can match boundary conditions to obtain the ion and electron fluxes away from the plasma and the primary current density.

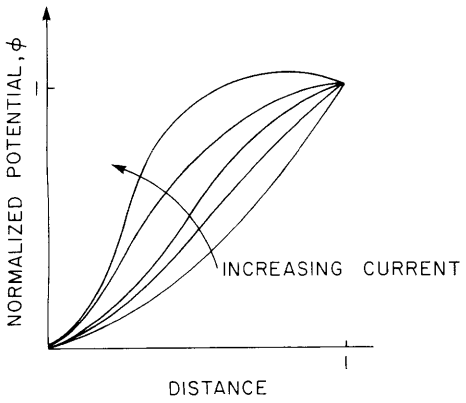

Fig. X-53.

Normalized potential vs distance for different currents. Lowest curve is in the space-charge-dominated regime; uppermost curve is in the plasma regime.

To solve the problem self-consistently (that is, to solve for the variables in terms of geometry, neutral density, and voltage), more equations are needed. The equations that we used are global conservation laws in the plasma. Finally, we are interested in macroscopic quantities, such as I-V curves, density, and temperature.

We assume that the plasma electrons do not contribute to the ionization process. This is a plausible assumption, since the high-energy component of the distribution function is lost through the anode sheath, and we are assuming long mean-free paths. The particle conservation equation is

$$\frac{dn_i}{dn} = \underbrace{\frac{J_o}{e}\,\frac{\left(1 - \exp(-n_o \sigma_T(v)a)\right)}{\sigma_T/\sigma_i}}_{\text{Production by primaries}} - \underbrace{\left(.345\, n_i \left(\frac{2kT_e}{M_i}\right)^{1/2}\right) 2}_{\text{Loss to anode and cathode}} = 0. \tag{4}$$

where σ_i is the total inelastic cross section.

An equation describing the cathode emission was derived by Crawford and Cannara.[4]

It can be expressed as

$$J_o = 2\pi^{1/2} a \phi^{1/2} e n_e \left(\frac{kT_e}{2\pi m_e}\right)^{1/2} \tag{5}$$

where $\phi_o = V_o/T_e$, and $a = n_{primary}/n_{secondaries}$ is given in Eq. 3 as a function of ϕ_o. We note that $n_i = n_e + n_p$, and Eq. 5 reduces to

$$2\pi^{1/2}\left[\frac{a\phi_o^{1/2}}{1+a}\right]\left[\frac{1 - \exp(-n_o\sigma_T a)}{\sigma_T/\sigma_i}\right] = .69\left(\frac{4\pi m_e}{M_i}\right)^{1/2}. \tag{6}$$

This is an equation for the temperature. It is valid, of course, only when the temperatures obtained are low enough; otherwise, the assumption of negligible ionization because of the secondaries breaks down.

The equation of conservation of energy should read

$$\begin{bmatrix}\text{energy lost by primary}\\ \text{slowing down}\end{bmatrix} = \begin{bmatrix}\text{energy carried away by ions and secondary electrons,}\\ \text{energy lost by secondary ionizing and exciting}\end{bmatrix}$$

Then, using Coulomb friction as the left-hand term, we obtain

$$\frac{J_o}{e}\frac{dw}{dx}a = \delta kT_e\left[\frac{J_o\left(1 - \exp(-n_o\sigma_T a)\right)}{\sigma_T/\sigma_i}\right] \tag{7}$$

where it is assumed that there is negligible excitation and ionization by secondary electrons, and δ is a constant ≈ 1.5. The average energy carried out by the exiting ion or electron as it crosses the plasma sheath is δkT_e.

Equation 7 can be rewritten

$$n_e = \frac{4\pi u_p^2 \delta kT_e \epsilon_o^2 m_e}{3\ln(\Lambda)e^4}\left[\frac{1 - \exp(-n_o\sigma_T a)}{a\sigma_T/\sigma_i}\right] \approx \frac{4\pi u_p^2 \delta kT_e \epsilon_o^2 m_e}{3\ln\Lambda e^4} n_o\sigma_i, \tag{8}$$

where u_p is the speed of the primaries. Equation 8 completes the set. It can be seen from Eqs. 5, 6, and 8 that $n_o a$ is a similarity rule for T_e, $n_e a$, and $J_o a$. A similarity rule for T_e, $n_e\sqrt{M_i}$, and $J\sqrt{M_i}$ in the long mean-free-path limit is $n_o\sqrt{M_i}$, which is subject to the same constraints as in the spece-charge-dominated region.

Two approximations limit the validity of the theory. As in the space-charge-limited regime, at very low ionization rates the current is given by the Child-Langmuir equation and not by Crawford's relation. What really breaks down is the $\lambda_D/a \ll 1$ assumption. It can be shown that a lower limit for the validity of the theory is

$$\sigma_i(V) > 4.2 \times 10^{-3}/n_o a.$$

The results are shown in Fig. X-54. The region of low current is invalid.

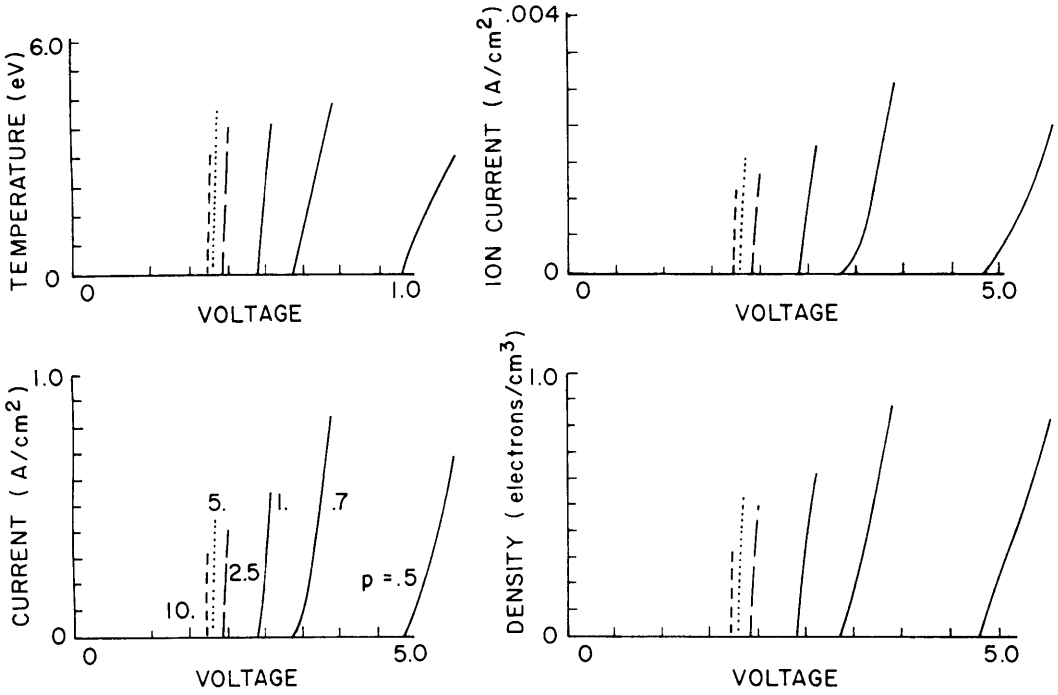

Fig. X-54. Microscopic parameters vs voltage in argon with variable pressure. Plasma regime curves drawn for 1-cm anode-cathode distance.

It should be noted, in agreement with results from the space-charge regime, that a plasma does not appear until the pressure is above a minimum. Also, for a given pressure, the voltage at which a plasma appears is approximately the voltage at which the slope of the I-V curve becomes infinite.

Experimental Results

For comparison with the theoretical predictions, we used data from a cylindrical discharge. The experiment was conducted by Barry N. Breen, an undergraduate member of RLE. Basically, the cathode is a BaO-coated cylinder of 5/16" diameter. The anode is a concentric cylinder of 1" diameter, and the gas is argon, 1" long.

The experimental data are shown in Fig. X-55. Figure X-55a shows the space-charge-dominated regime, while Fig. X-55b shows more of the plasma regime.

The pressures where the I-V curves break for a given voltage agree with the

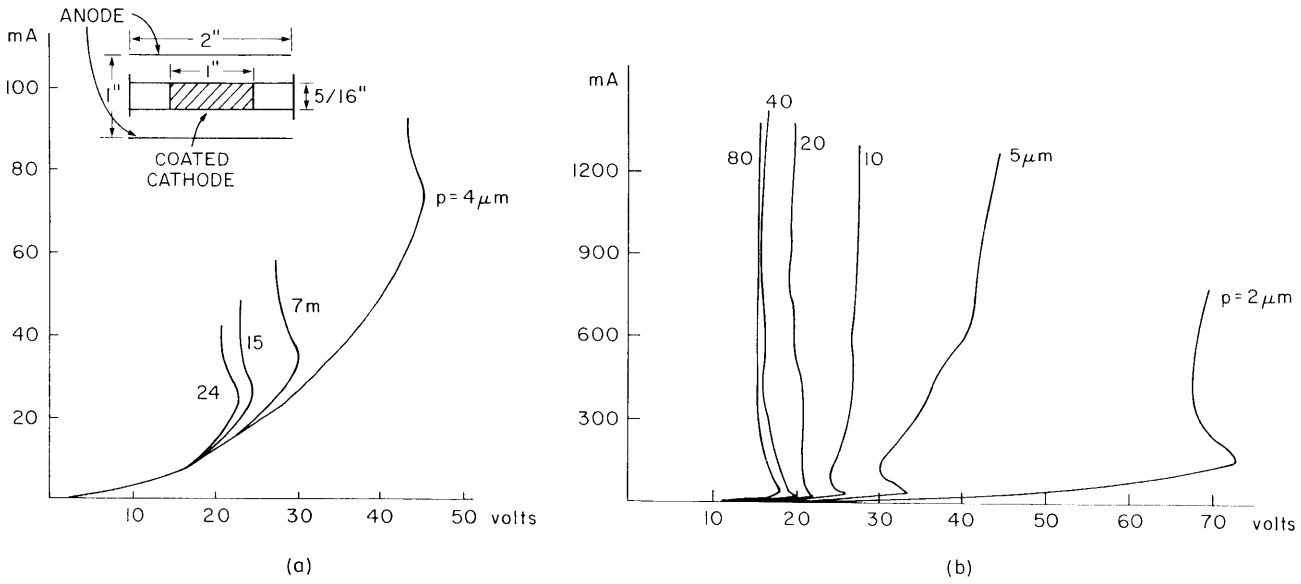

Fig. X-55. I-V curve for a cylindrical discharge in argon.
(a) Diameter of cathode, 5/16"; diameter of anode, 1"; length of discharge, 1".
(b) Same as (a) for higher currents.

calculated pressures within a factor of 3. For the plasma-dominated regime, however, the difference is larger. The reason is that in Eq. 6 the area of the cathode is equal to the area of the anode. In the experiment, the areas are different by a factor of 4, and therefore the right-hand side of Eq. 6 has to be multiplied by 2.1 $\left(= \frac{\text{A cathode + A anode}}{2}\right)$.

The results of Fig. X-54 are still valid if the pressure is multiplied by this factor. (Note that in Eq. 6 in the long mean-free-path limit the pressure appears linearly and can absorb this factor!) Taking this into consideration, we find that the agreement with the experiment is similar to that in the space-charge-dominated regime.

The reasons for the disagreement could be: (a) influence of geometry (cylindrical vs plasma), (b) bias in the measuring pressure gauge (although some care was taken to calibrate the gauges), and (c) end losses, which were neglected in this calculation.

Appendix

Consider the equation

$$\left(\frac{d\phi}{dz}\right)^2 = 4k\left(\phi^{1/2} + \left(\frac{M_i}{M_e}\right)^{1/2} \int_z^1 a(V_o\phi(z'))\left[\sqrt{\phi(z')} - \sqrt{\phi(z') - \phi(z)}\right] dz'\right)$$

with $\phi(0) = \frac{d\phi}{dz}(0) = 0$, $\phi(1) = \phi_1$.

Now make the substitution $\psi(z) = \frac{\phi(z)}{\phi_1}$. Then

$$\left(\frac{d\psi}{dz}\right)^2 = \frac{4k}{\phi_1^{3/2}}\left(\psi^{1/2}\left(\frac{M_i}{M_e}\right)^{1/2} \int_z^1 a(V_o\phi_1\psi(z'))\left[\sqrt{\psi(z')} - \sqrt{\psi(z') - \psi(z)}\right] dz\right).$$

If we define $k' = k/\phi_1^{3/2}$ and $V_o' = V_o\phi_1$, then this equation reduces to

$$\left(\frac{d\psi}{dz}\right)^2 = 4k'\left(\psi^{1/2} + \left(\frac{M_i}{M_e}\right)^{1/2} \int_z^1 a(V_o'\psi(z'))\left[\sqrt{\psi(z')} - \sqrt{\psi(z') - \psi(z)}\right] dz'\right),$$

with $\psi(0) = \frac{d\psi}{dz}(0) = 0$, $\psi(1) = 1$. Hence ψ satisfies the boundary conditions and the differential equation. This trick has been used to reduce the problem from an eigenvalue problem to an initial-value problem. The numerical method for solving this equation is as follows.

A shape of the potential is assumed. It could be the potential distribution for close but different conditions, or the low-pressure result obtained in the "no ionization" case. Values of k and v_o are chosen. Then Picard's iterative method[5] is used to obtain a

new potential distribution. This iteration involves plugging the approximate potential distribution into the right-hand side and integrating the equation numerically to obtain a new approximation. The iteration is repeated until the solution converges. The potential that is obtained satisfies the differential equation and the boundary conditions at $z = 0$, but not at $z = 1$. The transformation mentioned before is then used to find a solution that satisfies both the differential equation and the boundary conditions. This produces one point in the k vs V_o curve. The process can be repeated to generate an entire curve.

References

1. I. Langmuir, Phys. Rev. 33, 95 (1929).
2. S. A. Self, Phys. Fluids 10, 7 (1967).
3. A. Carusso and A. Cavaliere, Nuovo Cimento 26, 1389 (1962).
4. F. W. Crawford and A. B. Cannara, S. U.-M. L. Report No. 1261, Microwave Laboratory, Stanford University, Stanford, California, November 1964.
5. F. B. Hildebrand, Advanced Calculus for Applications (Prentice-Hall, Inc., Englewood Cliffs, N. J., 1962).

Research – Experimental

8. PARAMETER SPACE AVAILABLE TO VERSATOR I

U. S. Energy Research and Development Administration (Contract E(11-1)-3070)

Burton Richards, David S. Stone

Adjustable Parameters: Loop Voltage, Magnetic Field, and Limits of Stable Operation

The Versator I electrical systems were described in detail in RLE Progress Report No. 117 (pp. 242-249). One adjustable parameter that determines the behavior of the discharge is the initial loop-voltage pulse, applied around the plasma loop by an air-core transformer. This initial voltage may be varied to produce vacuum (unloaded) toroidal electric fields of up to .49 V/cm. As shown in Fig. X-56, the initial toroidal electric field must lie above a minimum value that causes an ionization rate (the gas is preionized to .1% fractional ionization with an RF toroidal electric field) sufficient to avoid runaway electron production. The initial plasma current is also proportional to

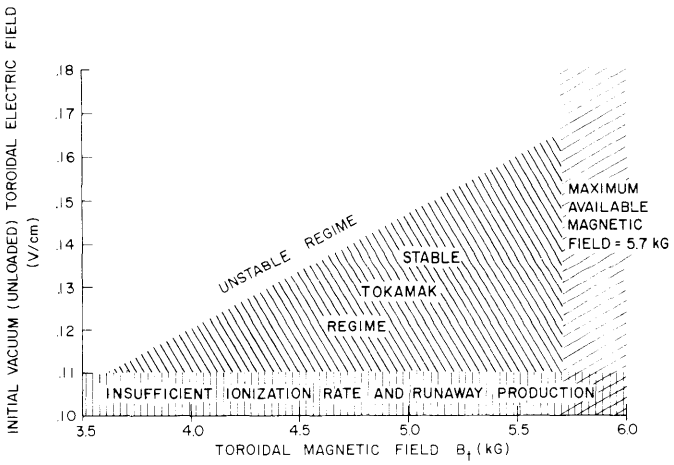

Fig. X-56. Regions of operation in parameter space accessible to Versator I. Variables are the initial vacuum (unloaded) toroidal electric field (E_t) and the toroidal magnetic field (B_t).

the initial loop voltage and the latter must not exceed a value that drives the current above the upper limit set by the Kruskal-Shafranov criterion[1] for MHD stability of the plasma loop,

$$I_p^{max} = \frac{5a^2 B_t}{qR}, \tag{1}$$

with I_p in amperes, a and R minor and major plasma radii in centimeters, q the MHD safety factor, and B_t in gauss. The plasma current I_p is proportional to the loop voltage V_{loop}, and therefore V_{loop}^{max} is proportional to the toroidal magnetic field B_t. These constraints define the region of stable Tokamak operation in parameter space that is accessible to Versator I. The electric field must lie between .11 and .16 V/cm while a toroidal field of less than 3.6 kG does not satisfy the requirement for stable Tokamak performance. The upper limit on the toroidal magnetic field is set for Versator I at 5.7 kG.

Variation of Parameters within Limits

The initial loop voltage and magnetic field may be varied within the limits that we have described (.11 V/cm < E_t < .16 V/cm and 3.6 kG < B_t < 5.7 kG). Under these conditions, the amplitude of the second portion of the loop-voltage pulse that is capable of delivering a vacuum toroidal electric field of up to 46 mV/cm for ~10 ms and whose purpose is to heat the plasma ohmically, may be varied up to a maximum value that is determined by Eq. 1. The amplitude of this second portion of the loop-voltage pulse may be adjusted to maximize the duration of the discharge and enhance the peak electron temperature. Discharge durations up to 10 ms and electron temperatures up to 180 eV (determined by the Spitzer conductivity[2]) have been achieved. Various parameters related to or determined by the initial loop voltage and the toroidal magnetic field are as follows.

beta poloidal electron	.1-.8
$V_{drift}/V_{thermal}$	.07-.24
T_e (electrons)	up to 180 eV
T_i (ions)	roughly 40 eV
τ_E (energy confinement time)	.08-.25 ms
I_p	2-6 kA

Measurement of T_i by Doppler Broadening of He II Line 4685.68 Å

For a typical hot stable discharge (T_e ~ 160-180 eV) the ions are cold with temperatures of approximately 30-40 eV. The ion temperature T_i has been measured by seeding the neutral fill gas H_2 with a small amount (0.5%) of He and measuring the Doppler broadening of the He II line at 4685.68 Å. We have assumed that this measurement provides a lower limit on the hydrogen ion temperature and that the presence of

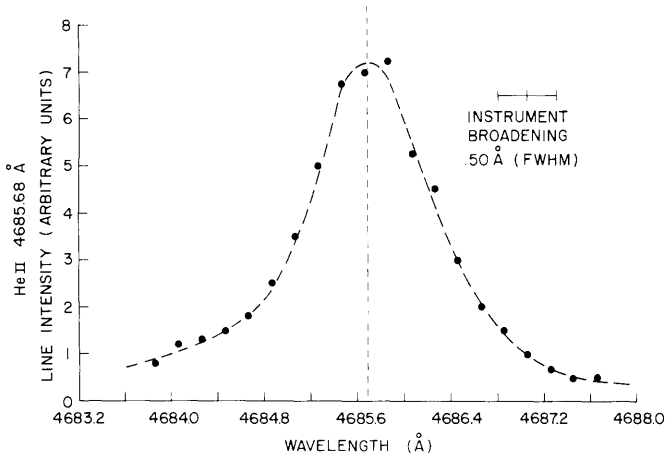

Fig. X-57. Doppler broadening of He II line 4685.68 Å in a Versator I hydrogen discharge. The fill gas H_2 is seeded with 0.5% He.

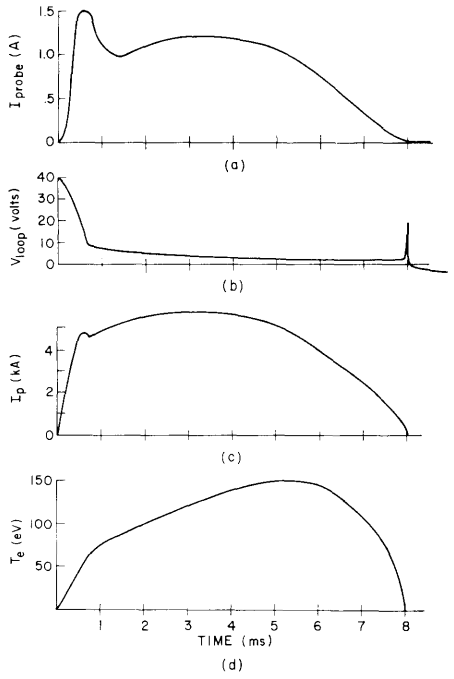

Fig. X-58. Time evolution of Versator I plasma parameters. (a) Saturation ion current ($\propto nT_e^{1/2}$) to a double Langmuir floating probe located ~7 cm from the center of the plasma as a function of time. Plasma minor radius ~3 cm. (b) Loop voltage as a function of time. (c) Plasma current as a function of time. (d) Electron temperature T_e as a function of time. The electron temperature is determined from the Spitzer conductivity of the plasma.

helium does not alter the character of the discharge. The results are shown in Fig. X-57. The Doppler effect broadens this spectral line ~1.2 Å, the full width at half maximum (FWHM), thereby indicating an ion temperature of ~31 eV. These data were obtained with the use of a 0.5 m Jarrel-Ash visible spectrometer [instrument broadening .50 Å (FWHM)] and an RCA Type 1P28 photomultiplier tube.

Time Evolution of Versator I Plasma Parameters

The time evolution of the Versator I plasma parameters particle density n, loop voltage V_{loop}, plasma current I_p, and electron temperature T_e determined from the Spitzer conductivity is shown in Fig. X-58.

a. Versator I Scaling Laws

The empirical scaling laws governing the Versator I plasma are summarized below and illustrated in Figs. X-59, X-60, and X-61.

$$I_p \propto B_t \tag{2}$$

$$T_e \propto I_p \tag{3}$$

$$n \quad \text{roughly constant at } 2\text{-}3 \times 10^{13} \text{ cm}^{-3} \tag{4}$$

$$a \quad \text{decreases with } I_p. \tag{5}$$

Relation 2 is expected from previous arguments leading up to Eq. 1. The temperature T_e is proportional to I_p, according to Eq. 3.

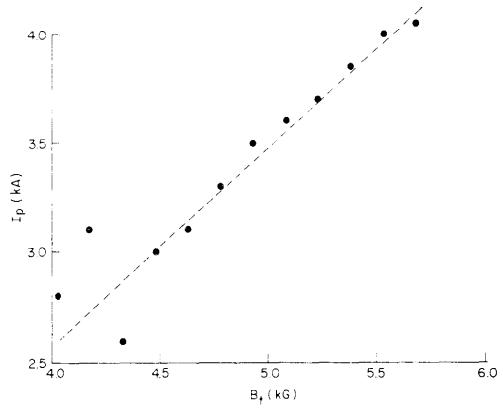

Fig. X-59. Plasma current as a function of toroidal magnetic field.

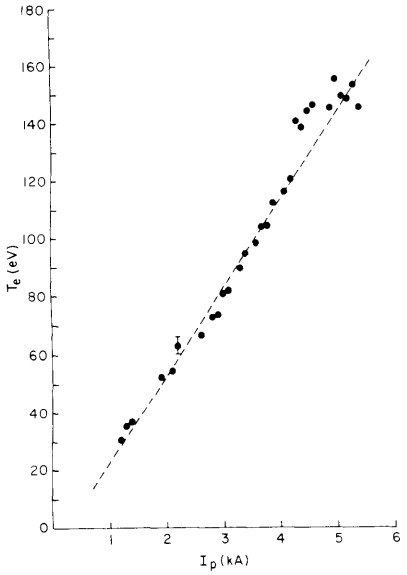

Fig. X-60.

Electron temperature derived from the Spitzer conductivity as a function of plasma current.

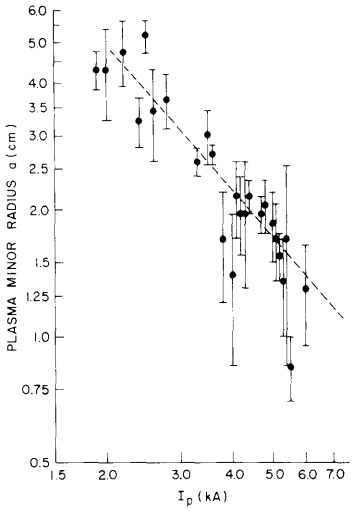

Fig. X-61.

Plasma minor radius as a function of plasma current.

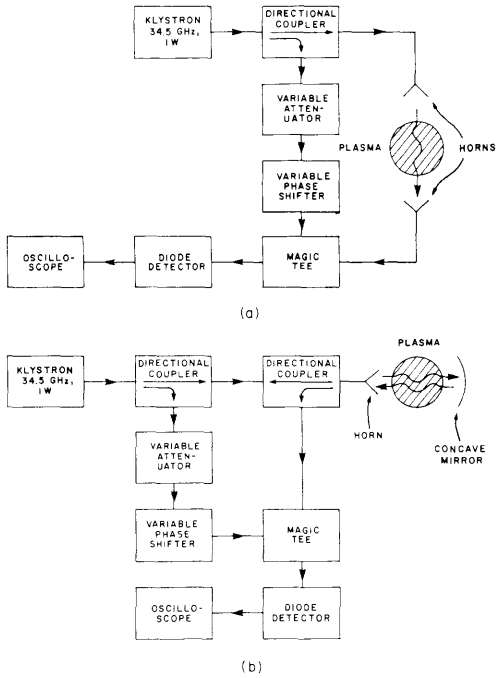

Fig. X-62. Comparison of (a) conventional single-pass microwave interferometer and (b) double-pass microwave interferometer.

b. Constant Density

The peak density (determined by the Langmuir probe and microwave interferometer) in the Versator I device is roughly constant (Eq. 4) and equal to $2\text{-}3 \times 10^{13}$ cm^{-3} for all accessible values of toroidal magnetic field, plasma current, loop voltage, and fill pressure. We believe this to be a consequence of the high impurity levels in the Versator I plasma.

The density is measured with an 8-mm (34.5 GHz, 1 watt) double-pass microwave interferometer. In Fig. X-62 the double-pass configuration is compared with the conventional single-pass configuration.[3] A concave metal surface (the wall of the vacuum chamber) reflects the microwave beam back on itself creating twice the phase shift of the single-pass technique. The returned signal is combined in a magic T in the interferometer arm with a portion of the original signal and the line-integrated plasma density is then determined by counting the resulting interference fringes.

Shrinking of Plasma Minor Radius with Increasing Current

We have observed that the plasma minor radius a shrinks with increasing current, an effect mentioned briefly in RLE Progress Report No. 117. The minor radius of the torus is 14 cm and the plasma minor radius would be expected to be independent of the plasma current and, since Versator I has no limiter, to be equal to ~10-12 cm. The shrinking of the plasma column can be explained by assuming that cold impurity species cool the outer edge of the plasma and force the current to flow in a narrow central channel.[4] At higher currents and temperatures this effect becomes more pronounced and causes further constriction of the plasma column.

The plasma minor radius is measured with an 8-mm microwave interferometer (f_o = 34.5 GHz) which is cut off as the plasma density exceeds the critical density ($n_{critical}$ = 1.5×10^{13} cm^{-3}) within the first millisecond of the discharge (see Figs. X-58 and X-62.) As the plasma density drops below the critical density near the end of the discharge, the number of fringes N counted on the interferometer determines the plasma minor radius:

$$a = \frac{cN}{2f_o}, \tag{6}$$

where c is the speed of light in vacuum and a parabolic density profile has been assumed. This method of determining a has the advantage that it is independent of the plasma density.

References

1. V. D. Shafranov, "Plasma Equilibrium in a Magnetic Field," in Reviews of Plasma Physics, Vol. II (Consultants Bureau, New York, 1966).
2. L. Spitzer, Physics of Fully Ionized Gases (John Wiley and Sons, Inc., New York, 1962).
3. M. Heald and C. Wharton, Plasma Diagnostics with Microwaves (John Wiley and Sons, Inc., New York, 1965).
4. H. P. Furth, J. Nucl. Fusion 15, 487 (1975).

9. CYCLOTRON RADIATION FROM VERSATOR I – PRELIMINARY RESULTS

U.S. Energy Research and Development Administration (Contract E(11-1)-3070)

David S. Stone

Preliminary measurements of cyclotron radiation emission from the Versator I plasma have been completed. The detection apparatus is a low-gain 8 mm horn (14.6 dB) which couples Ka-band radiation (26-40 GHz) from the plasma into one arm of a balanced crystal mixer (Fig. X-63). The signal is mixed with a local oscillator (10 mW at 35 GHz) and any difference-frequency signal at 30 MHz is detected by the balanced crystals and differentially amplified by an intermediate-frequency (IF) amplifier (gain 100 dB, bandwidth 10 MHz). The IF amplifier output is then read out on a storage oscilloscope and is proportional to the cyclotron power radiated into the horn by the plasma at 35 GHz.

The data presented in Fig. X-64 were taken with a 5.5 kG toroidal magnetic field and a corresponding cyclotron frequency $f_{ce} = 15.4/\gamma$ GHz, where γ is the ratio of total electron energy to electron rest mass energy. Therefore the radiation detected at 35 GHz has a frequency that lies between twice the fundamental ($2f_{ce} = 30.8/\gamma$ GHz) and three times the fundamental ($3f_{ce} = 46.2/\gamma$ GHz) for nonrelativistic electrons ($\gamma = 1$). The inhomogeneity of the magnetic field causes ~10% broadening of the fundamental frequency and its harmonics. The flux of hard x rays, plasma current, and 35-GHz plasma radiation power are shown for a typical shot with and without large runaway electron populations.

Correlation of Cyclotron Radiation with Presence of Runaways

The data collected thus far suggest that the cyclotron radiation at 35 GHz is strongly correlated with the presence of runaway electrons. In shots with and without large runaway electron populations, bursts of cyclotron radiation are detected before and during large hard x-ray bursts. This may be explained by assuming that the cyclotron radiation is emitted by a small fraction of the total electron population, the runaways.

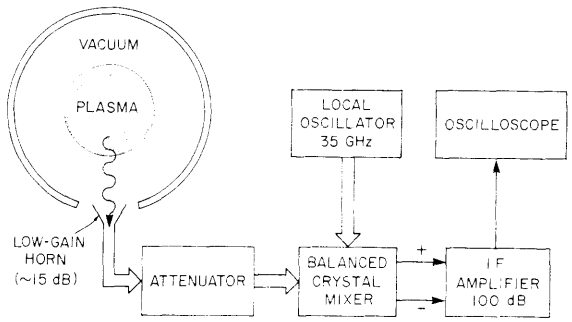

Fig. X-63. Diagram of apparatus used for detecting cyclotron radiation at 35 GHz.

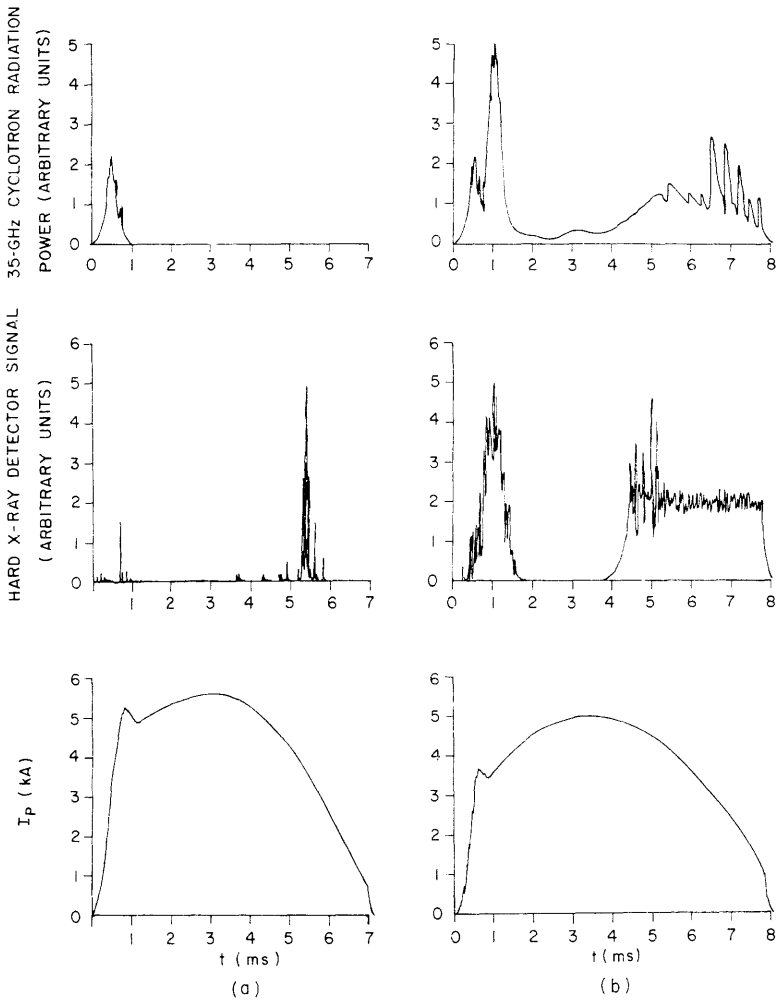

Fig. X-64. (a) Hot stable discharge.
(b) Runaway electron discharge.

The runaway particles are mildly relativistic and their energies, ~500 keV ($\gamma \approx 2$), have been determined by measuring the e-fold absorption length of the hard x rays in lead. Most of their velocity lies parallel to the toroidal field, but a small velocity component perpendicular to the magnetic field, $T_\perp \sim 50$ keV, is sufficient to enhance greatly the cyclotron power radiated by these electrons.[1] The power radiated by electrons in a nonrelativistic Maxwellian plasma[2, 3] follows the relation

$$P_{cyclotron} \sim nT_\perp B^2 (2T/m_o c^2)^m, \tag{7}$$

where n is the electron density, T is the temperature in energy units, B is the toroidal field, $m_o c^2$ is the electron rest mass, and m is the number of the radiation harmonic. (Equation 7 is not strictly correct for the runaway electrons since they are mildly relativistic and non-Maxwellian but, in the interest of simplicity, we shall assume that Eq. 7 is valid for order-of-magnitude estimates.) We may then estimate the ratio of cyclotron radiation emitted by runaways at the third harmonic ($4f_{ce}$ for these runaways, ~32 GHz) to that emitted by thermal electrons at the second harmonic (~31 GHz):

$$\frac{P_{runaways}}{P_{thermal}} \cong \frac{\left(nT_\perp \left(2T/m_o c^2\right)^4\right)_{runaways}}{\left(nT_\perp \left(2T/m_o c^2\right)^2\right)_{thermal}}. \tag{8}$$

From the preliminary data we have found that

$$\frac{P_{runaways}}{P_{thermal}} > 20. \tag{9}$$

The value given in relation (9) is an absolute minimum dictated by the signal-to-noise ratio for the detector. Using $(2T/m_o c^2)_{runaways} = 1$, and $T_{thermal} = 180$ eV, we find that

$$\frac{n_{runaways}}{n_{thermal}} > 2 \times 10^{-8}. \tag{10}$$

The frequency spectrum of this cyclotron radiation has not yet been measured. We plan to replace our fixed-frequency local oscillator with a sweep oscillator. We shall then be able to measure cyclotron radiation spectra as a function of time during the discharge.

References

1. D. Komm, Ph.D. Thesis, Department of Nuclear Engineering, M.I.T., 1976.

2. G. Bekefi, Radiation Processes in Plasmas (John Wiley and Sons, Inc., New York, 1966).

3. D. J. Rose and M. Clarke, Plasmas and Controlled Fusion (The M. I. T. Press, Cambridge, Mass., and John Wiley and Sons, Inc., New York, 1961).

10. PRELIMINARY STUDIES OF SOFT X-RAY EMISSION FROM VERSATOR I

U.S. Energy Research and Development Administration (Contract E(11-1)-3070)

Burton Richards, Geoffrey Garner, Robert Sand

A proportional counter has been installed on Versator to measure the spectrum of soft x rays (100-500 eV) emitted during the plasma pulse. The counter has a 1-mil beryllium window and is filled with 97% neon and 3% carbon dioxide at 1 atm pressure.[1,2] Figure X-65 shows typical data obtained on the counter. We have seven spectra, taken at 1-ms intervals for approximately 150 shots, which give the energy of photons vs number of photons of that energy. The data show, qualitatively, the plasma column

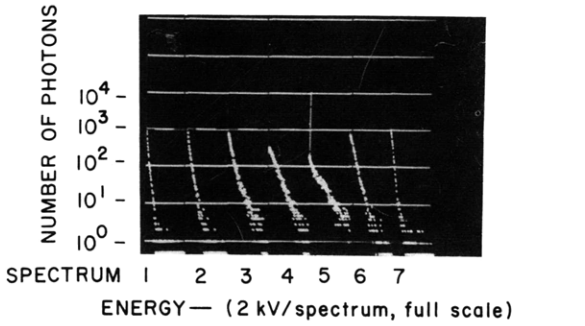

(a)

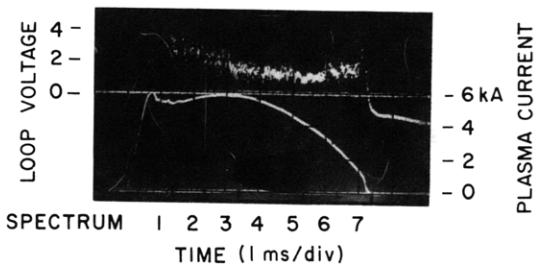

(b)

Fig. X-65. (a) Soft x-ray spectra, taken 1 ms apart (log scale).
(b) Typical current and voltage traces showing timing of soft x-ray spectra.

heating up with time, as can be seen by the progressively flatter spectra, until about the fifth millisecond of the plasma pulse. Then there is a rapid cooling as the plasma current dies. Difficulties discovered during the calibration of the detector and inconsistencies with the Spitzer temperature and spectroscopic data prevent a quantitative analysis at this time.

References

1. R. J. Sand, S.B. Thesis, Department of Physics, M. I. T., June 1976.
2. G. M. Garner, S.B. Thesis, Department of Physics, M. I. T., June 1976.

11. VACUUM ULTRAVIOLET STUDY OF THE DISRUPTIVE INSTABILITY IN THE VERSATOR I TOKAMAK

U.S. Energy Research and Development Administration (Contract E(11-1)-3070)

James L. Terry, Burton Richards, Barukh Ya'akobi, H. Warren Moos, George Bekefi

[J. L. Terry and H. W. Moos are at Johns Hopkins University. B. Ya'akobi is at the University of Rochester.]

The evolution of the oxygen impurity in the Tokamak Versator I has been investigated in stable and unstable discharges. The unstable discharge was characterized by a disruptive instability occurring approximately 1 ms into the pulse. In the study we utilized the vacuum ultraviolet resonance line radiation from oxygen ions and measured absolute levels of that radiation. We used an absolutely calibrated, 225 mm focal length normal-incidence monochrometer, sighting across a diameter of the plasma current cross section. A comparison of intensity time histories of lines from the ions O II through O VI in the stable and unstable modes showed that the ion evolution was significantly affected by the occurrence of the disruptive instability. In order to explain the differences in the two discharges, and to find the ion densities as a function of time and position, a one-dimensional computer code modeling the oxygen impurity evolution was developed. With this code we reconstructed electron temperature and density profiles in the column along the line of sight of the monochrometer and solved the rate equations in each small volume making up this column. By varying the particle influx and the ion confinement time (free parameters in the rate equations), we matched the code-predicted line intensities with those measured. The agreement is shown in Fig. X-66 for the unstable discharge. The effects of the instability have been modeled by a sudden drop in confinement time concurrent with a sharp increase in the number of oxygen atoms entering each unit volume along the column. Since the code could only model a fixed-radius plasma, we concluded that the physical interpretation of these particle influx

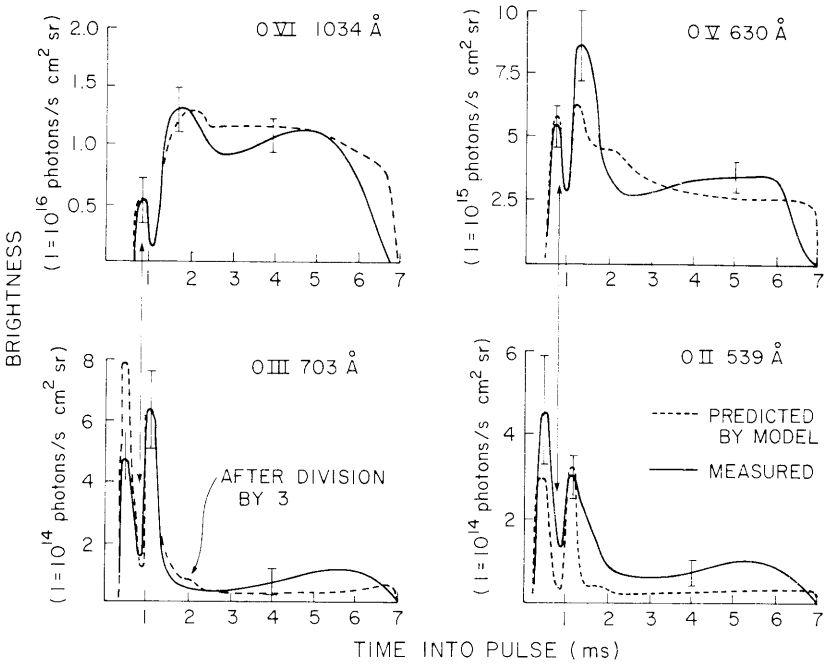

Fig. X-66. Comparison of model-predicted line-intensity time histories with those measured for the unstable discharge. Arrows mark the occurrence of the disruptive instability found from the plasma current-loop voltage signals. Note that for the O V and O VI lines there is a marked decrease in line intensity, whereas the O II and O III lines show a significant increase. These results cannot be explained entirely by a drop in temperature, since the characteristic recombination times are much longer than the times in which the second peaks in the O II and O III line-intensity time histories occur.

and confinement time functions is a sudden expansion of the plasma cross section into regions of "cold" oxygen atoms. The atoms in the region into which the plasma expands are quickly ionized to O II and O III, which accounts for the increase in their line radiation (see Fig. X-66). The number of O V or O VI atoms across a fixed line of sight is decreased, however, so that the line radiation from these ionization states is effectively decreased. Hence this explanation accounts for measured time histories and is consistent with the code results. Expansion of the current cross section in Versator is quite possible, since it has no limiter and the plasma does not fill the torus.

12. CRYOGENIC VACUUM ISOLATION OF PLASMA DIAGNOSTICS

U.S. Energy Research and Development Administration (Contract E(11-1)-3070)

James L. Terry, Burton Richards, H. Warren Moos, George Bekefi
[J. L. Terry and H. W. Moos are at Johns Hopkins University.]

A difficulty encountered during Versator ultraviolet spectrometry measurements was the contamination of the Tokamak plasma by the impurity influx from the spectrometer itself. The spectrometer vacuum chamber is pumped on by the main torus pumps through a pipe, 10 cm long and 4 cm in diameter (see Fig. X-67). The housing for the spectrometer equipment cannot be baked out or discharge-cleaned (typical cleaning procedures for Tokamaks) because this device contains electronics and optics that are intolerant of bakeout temperatures. But by cooling down the pipe connecting the spectrometer with the torus to liquid nitrogen temperature (77°K), the impurity influx from this diagnostic equipment can be reduced to acceptable levels for at least 10 hours.

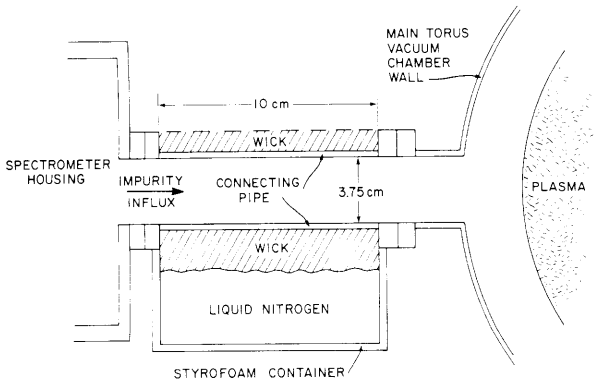

Fig. X-67.

Arrangement of torus, spectrometer, and connecting pipe, showing LN_2 cooling.

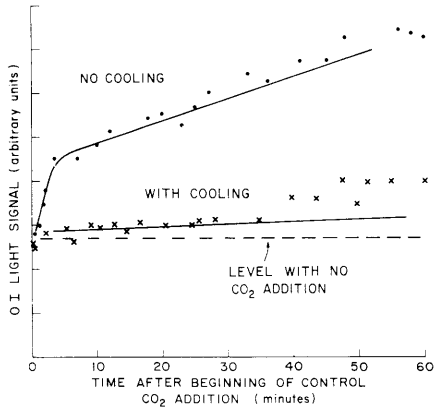

Fig. X-68

Level of oxygen impurity, showing the effect of cryogenic cooling.

A controlled test of this procedure was performed by adding a controlled influx (1.3×10^{-4} Torr-l/s) of CO_2 into the spectrometer chamber and looking at the OI (7774 Å) light with a visible spectrometer. Figure X-68 shows the OI signal during two runs, one with and one without liquid nitrogen cooling. A dramatic reduction in the impurity influx is seen during the cooled run.

We conclude that this technique provides good protection of high-purity plasma environments from contamination by peripheral plasma diagnostics.

13. EXPERIMENTAL DATA FROM AN ION SOURCE

U.S. Energy Research and Development Administration (Contract E(11-1)-3070)

Peter T. Kenyon, Louis D. Smullin

We have been able to extract up to 4 amperes of ion current from our ion source with an extraction efficiency γ (input power/extracted ion current) of 600 W/A. Optimum source performance occurs for neutral pressure of approximately 2 μm, H_2.

The extractor system is composed of two electrodes: a plasma electrode and an accelerator electrode. The extractor is illustrated in Fig. X-69. The plasma electrode transparency is approximately 50% and the open area is 20 cm^2. Since beam extraction is important and focusing is not, no particular attention was given at this time to the details of the slot geometry. The first set of measurements of ion extraction was made with a 3-mm interelectrode distance. The extraction voltage was derived from a pulse modulator capable of furnishing 1-7.5 kV pulses. The pulsewidth was 2.5 μs and it could be located arbitrarily within the 400 μs arc pulse. We then increased the pulsewidth threefold and no apparent depletion was seen. Our measurements of extracted ion current were made with the solenoidal magnetic field B_s and input power P_K as parameters. Graphs of extracted current I^+ vs extraction voltage V_E are shown in Fig. X-70 for various input conditions. Figure X-71 shows extracted current vs input power for B_s = 600 G and extraction voltage V_E = 5000 volts.

Secondary-emission electrons are not trapped by our accelerator; therefore, they contribute an error to the measured current. If we correct for secondary emission by using the data of A. I. Kislyakov et al.,[1] then the measured currents are reduced approximately 50%. In order to eliminate this source of error, future tests will be made with a Faraday cup collector.

As previously reported in RLE Progress Report No. 117 (pp. 256-260), we suspected a particle drift in our ion source because of the influence of the diverging solenoidal field. We were able to confirm this with a dual-probe system. These probes are illustrated in Fig. X-72. The difference in current between aft and forward probes indicates the drift. These probe currents are shown in Fig. X-73. At this time it is not clear whether the drift can be modeled as a symmetric distribution shifted along the velocity axis, or as an asymmetric distribution. Either model can give drift speeds defined by

$$\bar{v} = \frac{\int d^3\underline{v}\ \underline{v} f(\underline{v})}{\int d^3\underline{v}\ f(\underline{v})}.$$

Clearly, the drift energy of either species of ions or electrons cannot exceed the input cathode voltage V_K. If the species drift by ambipolar diffusion, then

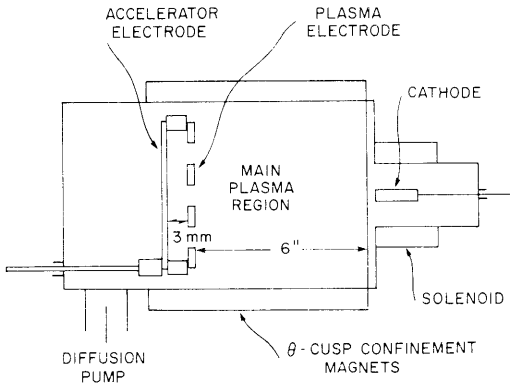

Fig. X-69. Ion source with ion extractor.

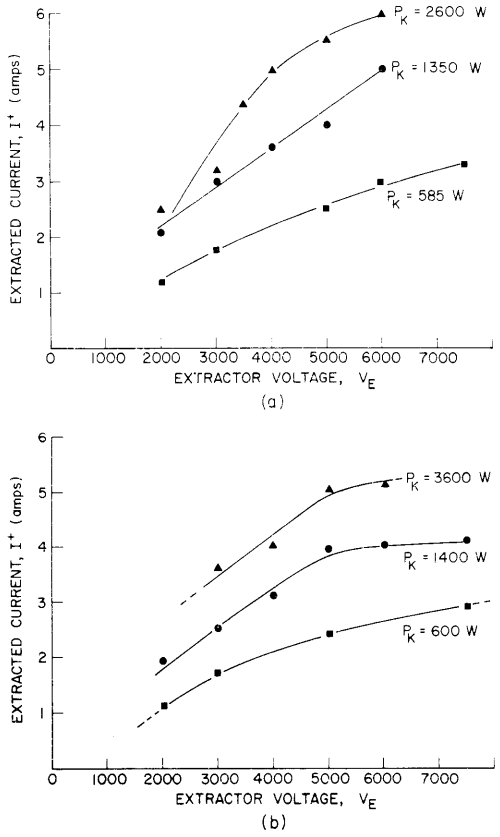

Fig. X-70. Extracted current vs extractor voltage p_o = 2 μm. (a) B_s = 400 G. (b) B_s = 600 G.

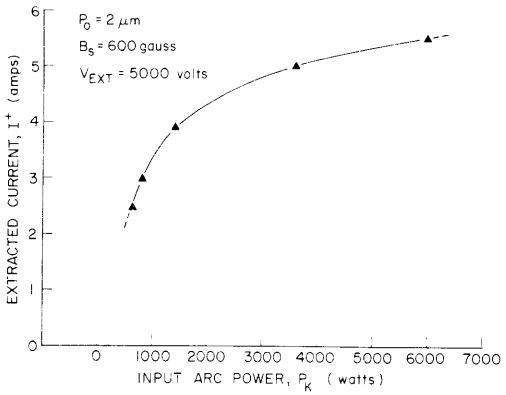

Fig. X-71. Extracted ion current vs input arc power.

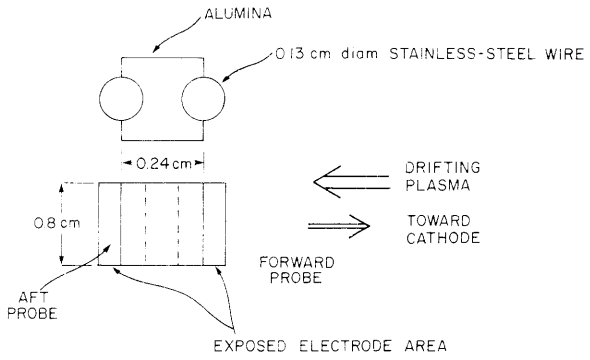

Fig. X-72. Dual-probe system.

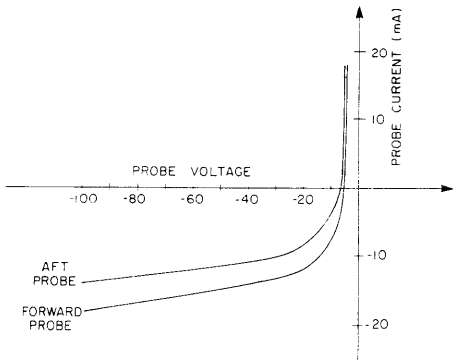

Fig. X-73. Currents of dual probes for P_K = 300 W and B_s = 400 G.

$$\mathscr{U}_i = \frac{m_i}{m_e}\,\mathscr{U}_e,$$

where $\mathscr{U}$ is the drift energy of either species. Using these facts allows us to place an upper bound on $\bar{v}$:

$$\bar{v} < \left(\frac{2qV_K}{m_i}\right)^{1/2}.$$

For example, if $V_K = 400$ V (an experimental operating condition), then

$$\bar{v} < 2.8 \times 10^5 \text{ meters/second.}$$

A more complete analysis of the drift data will be given in a future report.

References

1. A. I. Kislyakov et al., Sov. Phys. - Tech. Phys. 20, 986-987 (1975).

14. ION ACOUSTIC PROPAGATION IN A TWO-TEMPERATURE PLASMA

U.S. Energy Research and Development Administration (Contract E(11-1)-3070)

Peter T. Kenyon, Louis D. Smullin

Introduction

Using Langmuir probe current curves, we have observed a two-temperature plasma. This plasma can be modeled as a two-Maxwellian distribution. It was expected that the ion sound speed C_s would be influenced by the presence of the other electron species; that is, the sound speed should be a function of both electron temperatures. This functional dependence is given by

$$C_s = C_s\left(T_1^e, T_2^e\right),$$

where $T_1^e < T_2^e$. Our Langmuir curves show that $5 \lesssim T_1^e \lesssim 6$ eV and $40 \lesssim T_2^e \lesssim 60$ eV. In a separate measurement of the time delay, Δt_o, between cathode current I_k and the plasma current I_p (see Fig. X-74) at a distance d_o from the cathode, we were able to calculate an estimate of C_s:

$$C_s = \frac{d_o}{\Delta t_o} = \left(\frac{k_B T_o}{M_i}\right)^{1/2}.$$

This gives a temperature of approximately 5-10 eV, which, contrary to our initial

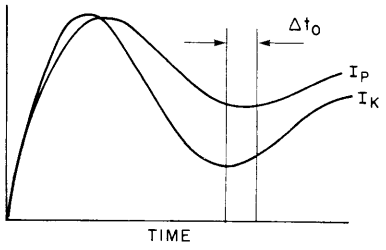

Fig. X-74.
Cathode current I_K and probe current I_P vs time for $d_o = 10$ cm and $\Delta t_o = 4$ μs.

expectations, shows that the higher temperature component is less influential than the lower in the propagation of linear ion acoustic waves.

Analysis

We assume that a one-dimensional analysis is sufficient to explain the previously stated phenomenon. The fluid equations necessary to derive the dispersion relation for a three-species plasma are

(i) continuity equations given by

$$\frac{\partial n_i}{\partial t} + \frac{\partial}{\partial x} n_i v_i = 0$$

$$\frac{\partial n_1}{\partial t} + \frac{\partial}{\partial x} n_1 v_1 = 0$$

$$\frac{\partial n_2}{\partial t} + \frac{\partial}{\partial x} n_2 v_2 = 0$$

(ii) momentum equations given by

$$m_i n_i \left[\frac{\partial v_i}{\partial t} + v_i \frac{\partial}{\partial x} v_i\right] = -\frac{\partial}{\partial x} p_i + q_i n_i E$$

$$m_e n_1 \left[\frac{\partial v_1}{\partial t} + v_1 \frac{\partial}{\partial x} v_1\right] = -\frac{\partial}{\partial x} p_1 + q_e n_1 E$$

$$m_e n_2 \left[\frac{\partial v_2}{\partial t} + v_2 \frac{\partial}{\partial x} v_2\right] = -\frac{\partial}{\partial x} p_2 + q_e n_2 E$$

(iii) Poisson's equation given by

$$\epsilon_o \frac{\partial E}{\partial x} = q_i n_i + q_e n_1 + q_e n_2.$$

To do a linear analysis we introduce the following expansions:

$$n_j = n_{oj} + \tilde{n}_j$$

$$E = E_o + \tilde{E}$$

$$v_j = v_{oj} + \tilde{v}_j$$

$$p_j = p_{oj} + \tilde{p}_j.$$

We assume that v_{oj} and $E_o = 0$, and $\tilde{T}_j = 0$ with $\partial n_{oj}/\partial x = \partial T_{oj}/\partial x = 0$. Since ion acoustic waves are inherently low-frequency disturbances, we assume (as is customary[1]) that the electron inertial effects are negligible and can be disregarded. This implies that the electron density obeys a Boltzmann's distribution given by

$$n_{1,2} = n_{o_{1,2}} \exp \frac{q_e \tilde{\phi}}{k_B T_{e_{1,2}}} = n_{o_{1,2}} \left[1 + \frac{q_e \tilde{\phi}}{k_B T_{e_{1,2}}} + \cdots \right]$$

where $\tilde{E} = -(\partial/\partial x)\tilde{\phi}$ (since $E_o = 0$) $= -jk\phi$, and it is assumed that all perturbation quantities go as $\exp[j(kx-\omega t)]$. The equation of state for the ions is

$$\frac{\partial}{\partial x} p_i = \nu_i k_B T_{o_i} \frac{\partial}{\partial x} n_i.$$

Since the ions undergo one-dimensional compression in the assumed plane wave $\exp[j(kx-\omega t)]$, we want eventually to set $\nu_i = 3$. [$\nu_i = (N_i+2)/N_i$; $N \triangleq$ number of degrees of freedom of ions.]

The linearized (and transformed) continuity equations are

$$-j\omega\tilde{n}_i = -jkn_{oi}\tilde{v}_i \tag{1a}$$

$$-j\omega\tilde{n}_1 = -jkn_{o1}\tilde{v}_1 \tag{1b}$$

$$-j\omega\tilde{n}_2 = -jkn_{o2}\tilde{v}_2. \tag{1c}$$

Note that (1b) and (1c) are not needed in the rest of this analysis. The momentum equations yield the following set of linearized transformed equations.

$$-j\omega m_i n_{oi}\tilde{v}_i = -q_i n_{oi} jk\tilde{\phi} - \nu_i k_B T_i jk\tilde{n}_i \tag{2a}$$

$$\tilde{n}_i = n_{o1} \frac{q_e \tilde{\phi}}{k_B T_{o1}} \tag{2b}$$

$$\tilde{n}_2 = n_{o2} \frac{q_e \tilde{\phi}}{k_B T_{o2}}. \tag{2c}$$

Using Eq. 1a, we get $\tilde{v}_i = \frac{\omega}{kn_{oi}} \times \tilde{n}_i$ and using Eq. 2a we derive

$$\tilde{n}_i = \frac{q_i n_{oi} k^2}{\omega^2 m_i - \nu_i k_B T_i k^2} . \tag{3}$$

Use of Eqs. 3, 2b, and 2c in the linearized Poisson's equations yields

$$\epsilon_o k^2 \tilde{\phi} = \frac{q_i^2 n_{oi} k^2}{\omega^2 m_i - \nu_i k_B T_i k^2} + \frac{q_e^2 n_{o1} \tilde{\phi}}{k_B T_{o1}} + \frac{q_e^2 n_{o2} \tilde{\phi}}{k_B T_{o2}} ,$$

which, letting $q_i = e$, we can rewrite as

$$\left(\frac{\omega}{k}\right)^2 = \frac{k_B T_i \nu_i}{m_i} + \frac{\omega_{pi}^2}{k^2 + \dfrac{\omega_{p1}^2}{\dfrac{k_B T_{o1}}{m_e}} + \dfrac{\omega_{p2}^2}{\dfrac{k_B T_{o2}}{m_e}}} . \tag{4}$$

Assuming that $k^2 \lambda_D^2 \ll 1$ for both species of electrons allows us to approximate Eq. 4 by

$$\left(\frac{\omega}{k}\right)^2 = \frac{\nu_i k_B T_{oi}}{m_i} + \frac{k_B}{m_i} \left(\frac{(n_{o1} + n_{o2}) T_{o1} T_{o2}}{n_{o1} T_{o2} + n_{o2} T_{o1}} \right)$$

where $n_{oi} = n_{o1} + n_{o2}$ is the quasi-neutrality condition. Assuming $T_{oi} \ll T_{o1}$, we have

$$\left(\frac{\omega}{k}\right)^2 = \frac{k_B}{m_i} \frac{(n_{o1} + n_{o2}) T_{o1} T_{o2}}{n_{o1} T_{o2} + n_{o2} T_{o1}} .$$

Application to Our Experiment

In our experiment, the Langmuir curve indicated that $T_{o2} \approx 10\ T_{o1}$ and we estimate that $(n_{o2}/n_{o1}) \approx 0.1$. Therefore

$$C_s^2 \approx \frac{k_B}{m_i} \left[\frac{n_{o1} \left(1 + \dfrac{n_{o2}}{n_{o1}} \right)}{10\, n_{o1} \left(1 + \dfrac{n_{o2}}{10\, n_{o1}} \right)} \right] (10\ T_{o1})$$

$$\simeq \frac{k_B T_{o1}}{m_i} .$$

This is verified by the measurement of the current time delays. Therefore the linear

acoustic wave is "independent" of the hotter electron species.

Conclusion

By equating the ratio $d_o/\Delta t_o$ with the sound speed, we assume that T_o is independent of space. In our theoretical analysis we also assume homogeneity in the zeroth-order temperature. Experimentally, however, we find spatially varying temperature for both cold and hot electron species. This is a source of error that must be included in the theoretical analysis. Also, the presence of the magnetic field has not been taken into account. We suspect that the assumption of three degrees of freedom for the electron is invalid, since this introduces a source of anisotropy in the theory.

References

1. N. A. Krall and A. W. Trivelpiece, Principles of Plasma Physics (McGraw-Hill Book Company, New York, 1973).

15. INSTABILITIES IN MINIMUM-B MIRROR SYSTEMS

U.S. Energy Research and Development Administration (Contract E(11-1)-3070)

Robert Klinkowstein, Louis D. Smullin

Introduction

The successful control of flute, drift, and negative mass instabilities in mirror machines has resulted from the effective use of minimum-B stabilizing fields and conduction through cold plasma to conducting walls, known as "line-tying." The other instabilities now being observed in minimum-B stabilized mirrors are microinstabilities resulting from velocity-space, loss-cone interactions. These instabilities drive particles into the loss cone and hence are lost. Velocity-space instabilities have been predicted theoretically and observed experimentally to some extent. There are many uncertainties, however, about the proper choice of theoretical models and boundary conditions in the study of these instabilities.

The drift-cyclotron instability, or drift-cone mode, is being observed at present in stabilized mirror experiments. This instability is driven by the coupling of ion cyclotron waves to drift waves associated with electron density gradients. It is an absolute instability that propagates across the field lines in the direction of the diamagnetic ion drift and is recognizable through a resonance condition that requires $\omega = \ell\Omega_i$, $\ell = 1, 2, 3 \ldots$, where Ω_i is the ion cyclotron frequency. The conditions for onset of this instability establish a critical radial density gradient that may be related to a critical plasma radius for many experiments.[1-4]

Other microinstabilities arising from the existence of a loss-cone limited

distribution do not appear to be a problem in present experiments. The drift-cone mode remains as the primary instability observed in the 2X11B mirror experiment at Lawrence Livermore Laboratory. Therefore, there is strong motivation for studying and controlling this instability.

This is the initial report of an experimental study to examine microinstabilities associated with loss-cone distributions of magnetic mirror experiments. The initial construction phase of the project was completed early in May 1976 and the data presented in this report are preliminary. The plasma sources are constructed of tungsten spiral cathodes mounted coaxially with stainless-steel anodes in a magnetron configuration.

Experiment

The investigation is based on a minimum-B mirror system using an array of ceramic permanent magnets to make a high-order, θ-periodic, cusp field superposed on a conventional mirror field. The plasma is formed by applying power to two plasma sources located at the mirror peaks (Fig. X-75). The magnetic field is produced by 10 coils each having 30 cm bore, 53 cm OD, and 7 cm length. By separately driving the center coils with a reverse current, it is possible to adjust the axial mirror ratio over a $2 < R < \infty$ range. Mirror peaks of ~2000 G are achievable. The θ-cusp field is produced by 12 ceramic magnets placed alternately around the interior of the vacuum chamber to produce a field of 1500 G at the magnet faces that decays radically inward

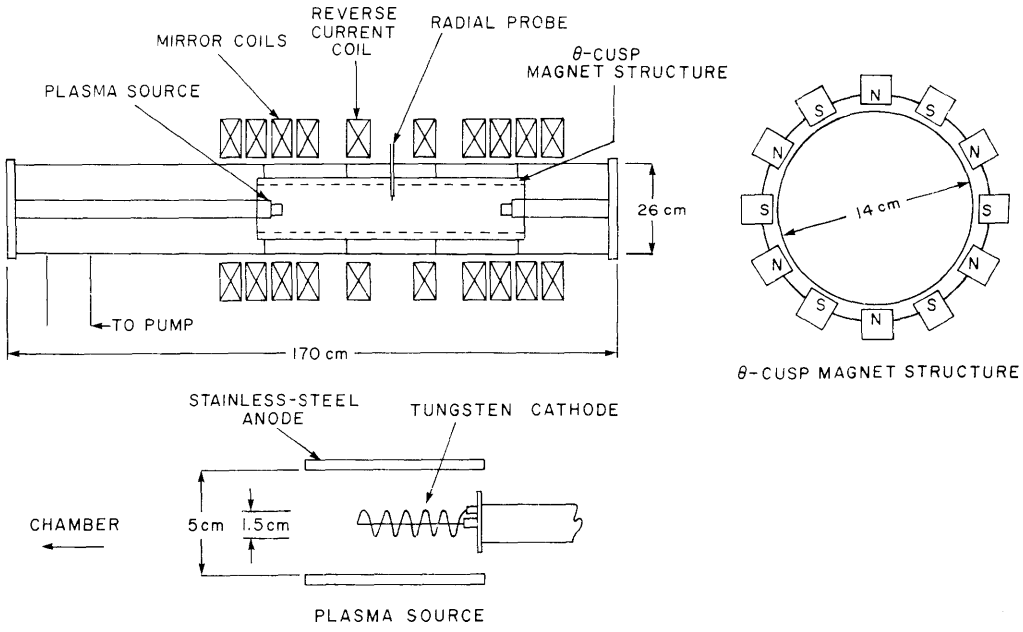

Fig. X-75. Schematic illustration of experiment.

[$B_{cusp} \approx .08r^5$ (r in cm)]. The experimental system will be capable of operating in pulsed or dc modes. At present, it is operating in a dc mode.

The buildup of plasma in the proposed system was expected to proceed as follows. Streaming plasma from the magnetron sources expands into the central region of the chamber where interchange instabilities occur, since $\partial B^2/\partial r < 0$ near the axis of the machine. The plasma expands radially and experiences $\partial B^2/\partial r > 0$ as it encounters the rapidly increasing θ-cusp field and thus becomes stable against interchange instabilities. The density builds up to a profile that is constant across the plasma radius and has a sharp gradient near the edge.

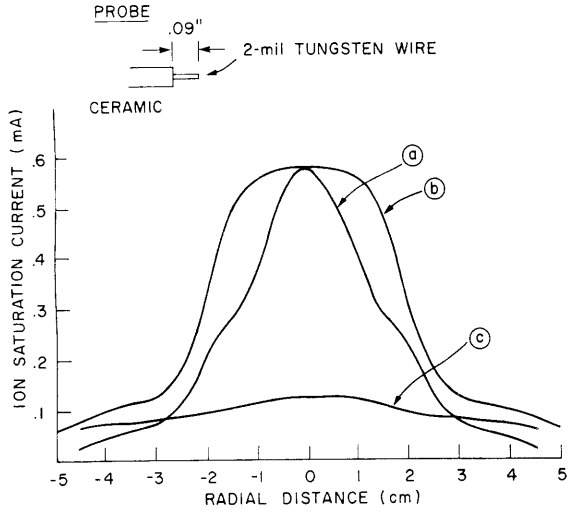

Fig. X-76.
Ion saturation current pressure = 2×10^{-4} H_2. Axial mirror ratios: (a) 2.5, (b) 4, (c) 6. $B_{max} = 700$ G.

Initial data for dc operation of the machine are shown in Fig. X-76. The data shown were for a pressure of ~2×10^{-4} Torr H_2. The plasma sources are capable of operation for pressures $\gtrsim 10^{-5}$ Torr. For the data shown each source was operated with a power input of 40 W. Interchange instabilities were detected with a probe ($f \approx 12$ kHz) for axial mirror ratios $R \leq 3$. For larger mirror ratios interchange instabilities were absent and the density profile developed a region of constant density. Langmuir probes were used to obtain density measurements, as indicated in Fig. X-76. Assumption of an electron temperature ≈ 10 eV indicates that these dc data points represent densities $10^{11} < n < 10^{12}$.

References

1. T. K. Fowler, Nucl. Fusion 9, 3-18 (1969).
2. R. F. Post and M. N. Rosenbluth, Phys. Fluids 8, 547 (1965).
3. A. B. Mikhailovsky, Nucl. Fusion 5, 125 (1965).
4. Y. Shima and T. K. Fowler, Phys. Fluids 8, 2245 (1965).